

RICE UNIVERSITY
**Thermodynamic Modeling and Molecular
Simulation of Amphiphilic Systems**

by

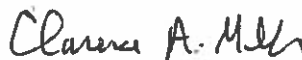
Le Wang

A THESIS SUBMITTED
IN PARTIAL FULFILLMENT OF THE
REQUIREMENTS FOR THE DEGREE
Doctor of Philosophy

APPROVED, THESIS COMMITTEE:



Walter G. Chapman, Chair
William W Akers Professor, Chemical
and Biomolecular Engineering; Associate
Dean for Energy, George R. Brown School
of Engineering



Clarence A. Miller
Louis Calder Professor Emeritus,
Research Professor, Chemical and
Biomolecular Engineering



George J. Hirasaki
A. J. Hartsook Professor Emeritus,
Research Professor, Chemical and
Biomolecular Engineering



Beatrice Riviere
Noah G. Harding Chair, Professor,
Department Chair, Computational and
Applied Mathematics

Houston, Texas

February, 2016

ABSTRACT

Thermodynamic Modeling and Molecular Simulation of Amphiphilic Systems

by

Le Wang

Interfacial phenomena are of vital importance to industrial and commercial applications from enhanced oil recovery to personal care products. To optimize interfacial processes, amphiphiles are usually involved, and, unlike simple molecules, amphiphiles possess both hydrophilic(water-loving) and hydrophobic(oil-loving) properties. Compared to the knowledge gained regarding the properties of simple fluids in the bulk region, our knowledge of modeling and prediction of the phase behavior and interfacial properties of amphiphiles is relatively less abundant. The goal of this thesis is to enhance our understanding of the phase behavior and interfacial phenomena of the systems containing amphiphiles using molecular simulation and statistical mechanics based theories. In particular, we have studied fundamental aspects related to enhanced oil recovery, i.e. interfacial tension, micelle formation, middle-phase microemulsion, foam stability and wettability alteration of reservoir rock surfaces.

In this thesis, the interfacial Statistical Associating Fluid Theory that relies on fundamental measure theory, mean field treatment of van der Waals interaction, and Wertheim's thermodynamic perturbation theory for association and chain connectivity along with molecular dynamics simulation have been used to study the molecular structure and interfacial properties of surfactant containing systems. Key contributions of this thesis include:

1. An approach inside iSAFT framework based on the Method of Moments that predicts the formation of middle-phase microemulsions of surfactant/oil/water systems has been presented.
2. The iSAFT approach has been extended to model surfactant micelle formation. Complete interfacial tension isotherm can be predicted. The effects of surfactant architecture have been studied.
3. The role of lauryl betaine as a foam booster was investigated. Insight was gained on the interaction between lauryl betaine and alpha olefin sulfonate.
4. The adsorption of deprotonated naphthenic acid on Calcite surface was studied, which is important in understanding the wettability alteration of carbonate reservoirs.

Acknowledgements

This thesis cannot be made possible without the supports from many:

First, I would like to thank my thesis advisor Dr. Walter G. Chapman for his support in research and help in my daily life. I benefited greatly from our discussions. His enthusiasm for research and wisdom in life have always led me to the right direction. I would also like to thank Dr. George J. Hirasaki, Dr. Clarence A. Miller and Dr. Beatrice Riviere for serving on my thesis committee and for the valuable discussions and comments on my research. Thanks to Dr. Kenneth R. Cox, Dr. Lisa Biswal, Dr. Deepti Ballal and Dr. Pradeep Venkataraman for the discussions and inspirations at the early stage of my research. I thank Dr. Yingcheng Li, Dr. Jun Jin and Ms. Xiujuan He from China Sinopec for the industry related discussions and experience.

I feel fortunate to have a group of talented people to work with. Thanks to Mr. Amin Haghmoradi, Dr. Dilip Asthagiri, and Dr. Wael Ahmad, whom I have worked with to solve a number of challenging problems in thermodynamics. Thanks to Dr. Aarthi Muthuswamy, Mr. Luqing Qi, Mr. Yongchao Zeng and Mr. Siyang Xiao for providing experimental insights and for collaborating in enhanced oil recovery topics. I also thank my group mates, Ms. Artee Bansal, Mr. Arjun Parambathu, Dr. Ali Hammadi, Dr. Bennett Marshall, Dr. Deepti Ballal, Dr. Essmaïil Djamali, Dr. Hassan Alasiri, Ms. Jinlu Liu, Dr. Kai Langenbach, Dr. Kai Gong, Mr. Mohamed Hosani, Dr. Pradeep Venkataraman, Dr. Sai Panuganti, Mr. Shun Xi, Mr. Xiaoqun Mu, Mr. Yuchong Zhang, and Dr. Zhengzheng Feng, for the conversations and for bringing joy to the office.

I thank Rice University Consortium for Processes in Porous Media, the Welch A.

Foundation and Abu Dhabi National Oil Company for their financial support.

Above all, I'd like to thank my family, including my parents, Xiujuan Gao and Yilin Wang, and my wife, Mengmeng Li, for their support and unconditional love. This thesis is dedicated to them. I am who I am today because of them.

Contents

Abstract	ii
List of Illustrations	x
List of Tables	xvii
1 Introduction	1
1.1 Motivation	1
1.2 Surfactant	2
1.3 Microemulsion	4
1.4 Surface/Interfaical Tension	6
1.5 Enhanced Oil Recovery	8
1.6 Challenges	10
1.7 Scope of the thesis	11
2 Theoretical Background	14
2.1 Potential Models	14
2.2 interfacial Statistical Associating Fluid Theory	16
2.3 Electrostatic iSAFT	22
2.3.1 Electrostatic Functional	22
2.3.2 Electrostatic Correlation	25
2.3.3 Preliminary Results	27
2.4 Summary	28
3 Method of Moments from iSAFT and the Formation of Microemulsions	32

3.1	Introduction	32
3.2	Stress Profile from iSAFT DFT	34
3.3	Results and discussion	36
3.3.1	Stress Profile of an Octane/Water Interface	36
3.3.2	Method of Moments	43
3.3.3	Effect of Temperature	45
3.3.4	Effect of Head/Tail Size	46
3.3.5	Single-Tail Surfactant vs Double-Tail Surfactant	46
3.4	Conclusion	52
4	Effect of Surfactant Architecture on Micelle Formation and Interfacial Tension	54
4.1	Introduction	54
4.2	Parameter Estimation	58
4.3	Results and Discussion	60
4.3.1	Water/surfactant binary mixtures	60
4.3.2	Water/octane/surfactant ternary mixtures	69
4.4	Conclusion	74
5	Simulation Studies on the Role of Lauryl Betaine in Mod- ulating the Stability of AOS Surfactant-Stabilized Foams	76
5.1	Introduction	76
5.2	Molecular dynamics simulations	78
5.3	Results and discussion	80
5.3.1	Area per molecule	81
5.3.2	Surface distribution of LB in the monolayer	83
5.3.3	Role of LB in the structure of surfactant monolayer	85
5.3.4	Binding energy of LB and surface dilatational modulus	89

5.4	Conclusion	92
6	Molecular Dynamics Simulation Study on the Adsorption of Naphthenic Acids on Calcite ($10\bar{1}4$) Surface	93
6.1	Introduction	93
6.2	Model and Methods	95
6.3	Results and Discussion	98
6.3.1	Water Structure at the Calcite/Water Interface	98
6.3.2	Adsorption of Deprotonated Naphthenic Acids on Calcite . . .	102
6.3.3	Effect of Temperature on Adsorption at Low Acid Concentration	105
6.3.4	Adsorption Driving Force	105
6.3.5	Free Energy of Adsorption of Carbonate Ion	107
6.4	Conclusion	108
7	Concluding Remarks	110
7.1	Summary	110
7.2	Future work	112
7.2.1	More Realistic Model for Surfactant	112
7.2.2	Micelles as Drug Delivery Carriers	112
7.2.3	Wettability Alteration	114
7.2.4	Solving iSAFT in Higher Dimension	115
	Bibliography	116
A	Numerical Integrals in 1-D Spherical Coordinate	146
A.1	Introduction	146
A.2	1-D Numerical Integrals	146
A.2.1	Ideal Gas Contribution	146
A.2.2	Hard Sphere Contribution	147

A.2.3	Long Range Attraction	152
A.2.4	Association Contribution	153
A.2.5	Chain Formation Contribution	154

B Simulation Box Snapshots and Pair Correlation Func-

tions **155**

B.1	Snapshots of the simulation box	155
B.2	Pair Correlation Functions	157

Illustrations

1.1	Schematic of Winsor Type Microemulsions	4
2.1	Potential Model for Association	16
2.2	Schematics of water, octane and amphiphilic chain constructure within the Telo da Gama and Gubbins model.	17
2.3	Density distributions(normalized by bulk density) for cations(red) and anions(blue) and mean electrostatic potential in a simple 1:1 electrolyte near a positively charged surface. $\sigma_+ = \sigma_- = \sigma = 0.425$ nm, $Q\sigma^2/e = 0.3$, $C = 0.1$ mol/L, where σ is the diameter of the ion, Q is the surface charge, e is the elementary charge and C is the concentration. $\Psi^* = \Psi e/kT$, where e is the elementary charge, k is the Boltzmann constant and T is the absolute temperature. Lines are from iSAFT and dots are from Monte Carlo simulation[1].	28
2.4	Density distributions(normalized by bulk density) for cations(red) and anions(blue) and mean electrostatic potential in a simple 1:1 electrolyte near a positively charged surface. $\sigma_+ = \sigma_- = \sigma = 0.425$ nm, $Q\sigma^2/e = 0.7$, $C = 1$ mol/L. Lines are from iSAFT and dots are from Monte Carlo simulation[1].	29

2.5	Density distributions(normalized by bulk density) for divalent cations(red) and monovalent anions(blue) and mean electrostatic potential in a simple 2:1 electrolyte near a negatively charged surface. $\sigma_+ = \sigma_- = \sigma = 0.3$ nm, $Q\sigma^2/e = -0.1685$, $C = 1$ mol/L. Lines are from iSAFT and dots are from Monte Carlo simulation[2].	29
2.6	Density distributions(normalized by bulk density) for monovalent cations(blue) and divalent anions(red) and mean electrostatic potential in a simple 1:2 electrolyte near a negatively charged surface. $\sigma_+ = \sigma_- = \sigma = 0.3$ nm, $Q\sigma^2/e = -0.1685$, $C = 1$ mol/L.	30
2.7	Density distributions(normalized by bulk density) for cations(red) and anions(blue) and mean electrostatic potential in a simple 2:2 electrolyte near a negatively charged surface. $\sigma_+ = \sigma_- = \sigma = 0.425$ nm, $Q\sigma^2/e = -0.1704$, $C = 0.5$ mol/L. Lines are from iSAFT and dots are from Monte Carlo simulation[3].	30
2.8	Density distributions for polyelectrolytes and coions in a electrolyte near a positively charged surface. $\sigma = 0.714$ nm, $Q\sigma^2/e = 0.125$, $\rho\sigma^3 = 0.01, 0.06, 0.16, 0.22$. Lines are from iSAFT and dots are from monte-carlo simulation[4, 5].	31
3.1	Comparison between iSAFT and MD for an A/B/AB mixture. The upper panel shows the density profile from iSAFT (solid lines) and MD (circles). The lower panel shows the stress profile from iSAFT (solid line) and MD (circles). $\rho^{bulk}\sigma^3 = 0.823$ and $x_{AB}^{bulk} = 0.004$	37
3.2	Interfacial tension of an octane/water interface as a function of temperature. Dots are from experiments[6]. Line is from iSAFT.	38
3.3	Stress($P_N - P_T$) of octane/water interface from iSAFT at 1 atm and various temperature.	40

3.4	Stress profile(grey) and density profile of a water(red)/octane(blue) interface at 298 K and 1 atm.	40
3.5	Fraction of association sites not bonded X_a at various temperatures and 1 atm. The increase of X_a implies the weakening of hydrogen bonding between water molecules.	41
3.6	Stress profile of a water/octane interface at 298 K and 1 atm. The total stress profile is decoupled to three contributions: the contribution from octane-octane interaction, that from water-water interaction and that from water-octane interaction.	42
3.7	Effect of temperature on surface torque density at zero interfacial tension and 1 atm.	47
3.8	Effect of head size on surface torque density at various temperature, 1 atm and zero interfacial tension. The tail size is fixed to 6 segments.	48
3.9	Effect of tail size on surface torque density at various temperature, 1 atm and zero interfacial tension. The head size is fixed to 5 segments.	48
3.10	Surface torque densities of single tail H5T6 and double-tail T3H5T3 surfactants at zero interfacial tension and 1 atm.	50
3.11	Density profiles(c, d) and stress profiles(a, b) of single-tail surfactants(a, c) and double-tail surfactants(b, d) under zero tension at 298 K and 1 atm. In d, the density profiles of the two tails are overlapping.	51
4.1	Liquid density(a, c) and saturated vapor pressure(b, d) of water and octane respectively from theory(line) and experiments(circle). Solubility of octane in water(e) from theory(line) and experiments[7](circle).	60
4.2	Comparison of Grand Potential for the CMC determination.	62

4.3	The top panel shows the structure of micelle formed by H_5T_4 surfactants from DFT calculation. The bottom panel is the radial distribution functions $g(r)$ for micelle formed by 40 $C_{12}E_5$ surfactant molecules. Reprinted with permission from ref [8]. Copyright 2011 American Chemical Society.	63
4.4	Effect of surfactant architecture on critical micelle concentration. (a) The effect of head size on the critical micelle concentration. All surfactants have 4 tail segments. (b) The effect of tail size on the critical micelle concentration. All surfactants have 6 head segments.	65
4.5	Effect of surfactant structure on aggregation number. (a) The effect of tail size on the aggregation number. All surfactants have 6 head segments. (b) The effect of head size on the aggregation number. All surfactants have 4 tail segments.	67
4.6	Surface tension as a function of surfactant concentration from iSAFT.	70
4.7	Surface tension isotherm. The top panel reprinted with permission from ref [9]. Copyright 1999 American Chemical Society. The bottom panel is reprinted with permission from ref [10]. Copyright 2000 American Chemical Society.	71
4.8	Structure of swollen micelle formed by H_5T_4 /octane/water at $25^\circ C$ and $1bar$	72
4.9	Comparison of the CMC values of surfactant/water systems and surfactant/octane/water systems. (a) The effect of head size on the critical micelle concentration. All surfactants have 4 tail segments. Squares are CMCs with oil present and crosses are CMCs without oil. (b) The effect of tail size on the critical micelle concentration. All surfactants have 6 head segments. Squares are CMCs with oil present and crosses are CMCs without oil.	73

4.10	Structure of reverse micelle formed by H5T4/water/octane using the parameters listed in Table 4.3.	75
5.1	Schematic of the head-group of (a) lauryl betaine (LB) and (b) alpha olefin sulfonate 14 (AOS-14). LB is zwitterionic, while AOS-14 is anionic. Lauryl betaine has an alkyl chain length comprising 12 carbons, while AOS-14 has an olefinic chain comprising 14 carbon atoms.	79
5.2	Area per molecule averaged over 10 ns. The standard error of the mean is negligible compared to the size of the symbol.	82
5.3	Pair correlation functions for various surfactant systems. S-N correlation (blue curve) in 3:7 mixture of LB and AOS; N-N correlation for neat LB (green), and S-S correlation for neat AOS (red).The curves are offset for clarity.	83
5.4	Normalized density profile for nitrogen (green), sulfur (red), and carboxylate carbon (blue) in 3:7 mixture of LB and AOS in a direction perpendicular to the interface. $z = 0$ nm defines the center of the octane slab and $z = 8.8$ nm approximately corresponds to the center of the water slab. The density distribution of each component is normalized by $\int \rho(z)dz$, where the integration is across the oil/water interface.	84
5.5	Angle between C-C vector in the LB head-group (-N-C-CO ₂) and the monolayer normal. The standard error of the mean is negligible on the scale of the graph.	86
5.6	Average order parameters for surfactant hydrocarbon chains of LB (left panel) and AOS-14 (right panel).	88

5.7	Binding energy of a distinguished LB with the rest of surfactants in the monolayer. The statistical uncertainty is smaller than the size of the symbols.	89
5.8	Surface Dilatational Modulus obtained using Eq. 5.2. The surface tension in Eq. 5.2 was calculated using the pressure tensor for systems differing in area by 7% from the equilibrium value.	91
6.1	Schematic of $C_5-C_9-CO_2^-$ where C_5 represents cyclopentyl.	97
6.2	Illustration of the simulation box. The calcite crystal(in the middle) is sandwiched by two water phases(red dots) which is in coexistence with their vapor phases(blank space). The green lines in water phase represents deprotonated naphthenic acid molecules.	97
6.3	Number density distribution of calciums in calcite and oxygens in TIP4P/2005 water model.	99
6.4	Orientation of water molecules. x axis is the distance of oxygen atoms from the surface. y axis represents the cosine values of the angles between dipoles of water molecules and surface normal averaged over molecules and time.	100
6.5	Charge distribution of calcite/water interface	101
6.6	Potential of mean force(PMF) of naphthenic acids with different tail length at 300 K: a) no tail, b) $C_2 - C_5$ tail, c) $C_9 - C_5$ tail. The PMF is normalized by kT , where k is the Boltzmann constant and T is absolute temperature. The gray shades are the statistical error estimated by using Bayesian bootstrap method.	104
6.7	Potential of mean force of the $C_5 - C_9 - COO^-$ naphthenic acid at 310 K. The gray shades are the statistical error estimated by using Bayesian bootstrap method.	106

6.8	Entropic($-T\Delta S$) and enthalpic(ΔH) contributions to the free energy of adsorption($\Delta A = \Delta H - T\Delta S$) at 300 K.	107
6.9	Potnetial of mean force of the carbonate ion at 300 K. The gray shades are the statistical error estimated by using Bayesian bootstrap method.	108
A.1	Coordinate transformation from rectanlinear to spherical coordinate.	148
B.1	Snapshots of the systems listed in Table 1 at the end of production. Color scheme: LB in green, AOS in white, octane in gray, water in blue, and NA in yellow. Black represents vacuum. The aspect ratios of the simulation boxes printed here are kept the same as the original simulation cells while the real dimensions are not produced.	156
B.2	3-D Pair correlation functions between C in carboxylic group of LB and sodium(solid blue) and S in sulfonate group of AOS and sodium(dash green), respectively. The range of y axes are kept the same for comparison.	157

Tables

3.1	Summary of Parameters	38
4.1	Summary of Parameters	59
4.2	Effect of head size and tail size on the CMC from experiment	66
4.3	iSAFT parameters for surfactant that forms reverse micelle	74
5.1	Compositions of the various systems studied in this work. The number of molecules in each system is noted in the columns.	81
5.2	Local composition versus overall composition of LB in the monolayer. The local composition is given by $LB_{local} = (N_{LB} + 1)/(N_{LB} + N_{AOS-14} + 1)$, where N is the number of particles (either LB or AOS) within the first shell of the distinguished LB molecule. (These N values are standardly obtained from the pair correlation.)	85

Chapter 1

Introduction

1.1 Motivation

Surfactants have been widely used in industry and our daily life. In the oil industry, surfactants find great applications in enhanced oil recovery processes (EOR). EOR, also called tertiary recovery, refers to the techniques that increase the production of crude oil from oil reservoirs after waterflooding. Due to surfactants' amphiphilic nature, they can be used to alter the interfacial tension of the oil-water interface and alter the wettability of rock surfaces such that the oil trapped in the porous media can be more easily released. Additionally, with the help of certain surfactants (alpha olefin sulfonate, internal olefin sulfonate, etc), strong foam can be generated that provides mobility control of the injected fluid to increase the sweep efficiency and oil production.

In surfactant EOR processes, ultra-low interfacial tension is favored. When ultra-low interfacial tension is achieved, a homogeneous and transparent mixture of oil, water, and surfactant can be observed, and this mixture is referred to as a middle-phase microemulsion. So, experimentally, surfactant formulation is screened based on the appearance of the middle-phase microemulsion for ultra-low interfacial tension. However, this process can be time-consuming and expensive. Additionally, the mechanisms behind a number of phenomena related to oil recovery, such as lauryl betaine enhancing foam stability, wettability alteration of carbonate reservoirs, etc,

are still not well understood. Hence it is desirable to utilize molecular modeling tools to understand the properties of surfactants and their roles in interfacial phenomena.

1.2 Surfactant

Surface active agents or surfactants exhibit complex and interesting phase behavior at fluid/fluid(vapor) or fluid/solid interfaces and in bulk solution due to their amphiphilic nature. Each surfactant molecule generally has one or more hydrophilic moieties or heads and one or multiple hydrophobic moieties or tails. The surfactant tail is usually an alkyl chain that dislikes water and acts as the driving force for the aggregation of surfactants in aqueous solution through an entropically driven process. The surfactant head is hydrophilic and can form hydrogen bonds with water molecules (nonionic surfactants) or interact with water molecules through electrostatic interactions (ionic surfactants) that enhances the solubility of surfactants in water. Depending on the type of charge their head groups carry, surfactants are classified into four categories[11]: nonionic surfactants(e.g. polyethelene glycol alkly ether), anionic surfactants(e.g. alpha olefin sulfonate, carboxylic acid), cationic surfactants(e.g. quaternary ammonium organics) and zwitterionic surfactant(e.g. betaines, sultanes). The head charge of certain surfactants, such as alkyl amidine compounds[12], can be modified by the environment they are exposed to. They are referred to as switchable surfactants. The surfactant's electrostatic characteristics are very important and have to be considered in different applications. For example, in enhanced oil recovery process concerning carbonate reservoirs, special attention has to be made when applying anionic surfactants since the favorable interaction between positively charged carbonate rock surface and negatively charged anionic surfactant would result in the adsorption and a huge loss of surfactant[13], making the process less effective and

economical.

The unique chemical nature of surfactants leads to interesting and attractive phase behavior in either aqueous or oleic environment. They can participate at the interface between hydrophobic and hydrophilic media to reduce the interfacial tension and, as the concentration rises, they can self-assemble into micelles(usually spherical at low surfactant concentration)[14]. The onset concentration at which micelles start to form is the critical micelle concentration(CMC). After this concentration is reached, the surface concentration of surfactant molecules at the interface is approximately constant, hence, interfacial tension stays constant. As concentration further increases, spherical micelles may aggregate and elongate to form cylindrical/worm-like micelles(responsible for the change of viscosity)[15], hexagonal structure[16], bicontinuous structure[17] and liquid crystalline structure. They can also precipitate out of the solution at certain conditions making the solution cloudy to one's eye. The phase behavior of surfactant solution can affect its macroscopic properties. For example, the entanglement of worm-like micelles could increase the viscosity of the solution[18]. For ionic surfactants, the formation of micelles can change the conductivity of the solution, which can be used as a criterion to determine the CMC(conductivity method[19]). The formation of a bicontinuous structure will greatly enhance the mutual solubility between dislike oil and water and this bicontinuous phase is called a middle-phase microemulsion. It is an indication of the ultra-low interfacial tension between oil phase and water phase. Thus it finds great application in enhanced oil recovery processes. Due to these effects, surfactant can be utilized as detergents, emulsifiers, solution viscosity modifier, interfacial tension modifier, structural templates for nanoparticle synthesis, carriers for drug delivery processes, etc.

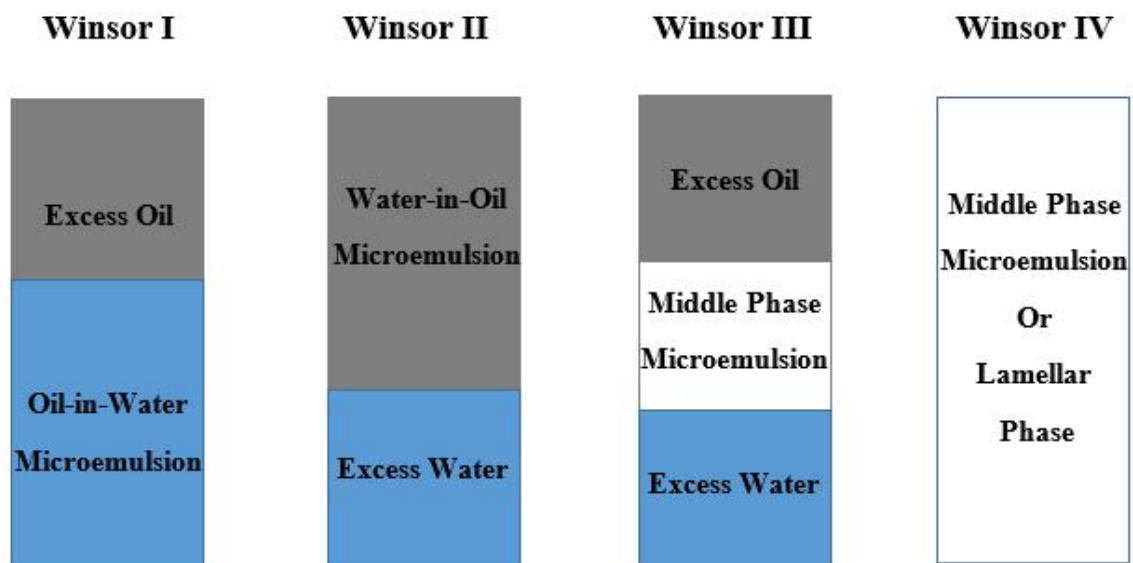


Figure 1.1 : Schematic of Winsor Type Microemulsions

1.3 Microemulsion

Microemulsion is defined as a ternary mixture of oil, water, and surfactants, which is homogeneous and thermodynamically stable[20]. According to Winsor[21] who proposed the Winsor R-ratio to predict the favorable type of microemulsions, there are four types of microemulsions, i.e. an oil-in-water microemulsion in coexistence with excess oil phase, a water-in-oil microemulsion in coexistence with excess water phase, a middle-phase microemulsion in coexistence with excess oil and water, and a single-phase microemulsion formed by adding sufficient amount of surfactant resulting in maximum solubilization of excess oil and water. The schematic is shown in Figure 1.1.

The Winsor R-ratio theory, as mentioned before, can be used to qualitatively understand the type of microemulsions formed under specific external conditions, i.e.

temperature, pressure, salinity, surfactant architecture, and solvent structure. The type of microemulsions is determined based on the bending of a pre-defined interfacial layer of surfactants at a planar oil/water interface. The tendency of the interface to bend toward water phase is compared against the tendency of the interface to bend toward the oil phase. This tendency is influenced by the interaction energy or cohesive energy between surfactant layer and oil or water phase. The Winsor R-ratio can be written as

$$R = \frac{A_{TO} + A_{HO} - A_{OO} - A_{TT}}{A_{TW} + A_{HW} - A_{WW} - A_{HH}} \quad (1.1)$$

where A refers to cohesive energy, and the index T , O , H , W represents surfactant tail, oil, surfactant head, and water, respectively. A_{XY} denotes the cohesive energy between X and Y . If $R < 1$, the interaction between surfactant and water is more favored than the interaction between surfactant and oil. Hence, the surfactant layer will be convex to water. Water becomes the continuous phase and an oil-in-water microemulsion is favored. Similarly, if $R > 1$, a water-in-oil microemulsion is favored. When the cohesive energy between the planar surfactant layer and water molecules is equivalent to the cohesive energy between the surfactant layer and oil molecules ($R = 1$), a middle-phase microemulsion is favorable. Although lots of insight can be gained from Winsor R-theory, the theory is relatively hard to implement since the cohesive energy between surfactant monolayer and bulk phase is not straightforward to calculate considering the fact that an interfacial layer must be defined beforehand.

In 2003, Fraaije et al.[22] proposed a more quantitative method referred to as the Method of Moments. A direct mapping between the Method of Moments and Winsor R ratio is available. This will be discussed in more details in Chapter 3. Other empirical correlations such as packing parameter[23] and hydrophilic-lipophilic

balance(HLB)[24] can also help explain the formation of microemulsions. However, the predictive power of empirical correlations is usually poor and will not be the focus of this thesis.

1.4 Surface/Interfaical Tension

Associated with surfactants and microemulsions, surface tension or interfacial tension is of special interest. It can be defined as the surface excess free energy or the work needed to create a surface with unit area and plays great roles in mass transfer, nucleation, wetting[25], and enhanced oil recovery process[26]. Based on convention, the definition of surface tension and interfacial tension is a little different. Surface tension usually refers to the surface excess energy between one phase and a vapor phase, while interfacial tension is the surface excess energy between other phases. But hereafter, those two terms will be used interchangeably.

Various approaches can be taken to investigate the magnitude of interfacial tension. Experimentally, interfacial tension can be measured by capillary rise method[27], pendent drop method[28], Wilhelmy plate method[29], etc. Theoretically, depending on the ensemble of interest, interfacial tension can be written as the change of corresponding free energy over the change of interfacial area. In (NpT) ensemble, interfacial tension γ is $\gamma = (\frac{dG}{dA})_{T,p,N}$ that can be derived from the change of Gibbs energy of the system written as

$$dG = \left(\frac{dG}{dT}\right)_{p,N,A}dT + \left(\frac{dG}{dp}\right)_{T,N,A}dp + \sum_i \left(\frac{dG}{dN_i}\right)_{T,p,N_{j \neq i},A}dN_i + \gamma dA \quad (1.2)$$

where G is Gibbs free energy, T is the temperature, N_i denotes the amount of species i , p is the pressure, and A is the interfacial area. In this classical thermodynamics treatment, not many insights into the interfacial region besides the magnitude of

interfacial tension can be obtained.

van der Waals realized that the densities of molecules change continuously between two bulk phases[30] and an expression of local free energy density composed of both homogeneous free energy introduced by a bulk Equation of State and local density approximation and inhomogeneous free energy(a density gradient term)[31] was introduced to describe this distribution. Later, the theory was organized and completed by Cahn et al.[32] and the density gradient theory (DGT) was proposed. DGT, based on the bulk Equation of States, has been widely used to calculate the value of interfacial tension[33, 34, 35] and showed good accuracy. Furthermore, the density distribution of molecules across the interfacial region can be obtained and interesting observations such as the aggregation of toluene at oil/water interface can be made. Aside from DGT that relies on bulk EoS and local density approximation, classical density functional theory (DFT) is known to be most versatile and successful approach to describe interfacial properties[30]. In DFT, the free energy density is described by the inhomogeneous free energy functionals designed specifically for the inhomogeneous region. The interfacial tensions calculated have been shown to be in good agreement with experimental data[36, 37]. Furthermore, the distribution of molecules such as amphiphilic molecules at liquid/liquid interfaces can be described which is currently not available from the DGT approach.

With the development of computational power, computer simulation techniques such as Monte Carlo simulation(MC), molecular dynamics simulation(MD), and dissipative particle dynamics(DPD) were developed and keep gaining attention from researchers for investigating the interfacial properties[38, 39, 40, 41]. To calculate interfacial tension between two liquids, two slabs of bulk liquid phases are placed in the simulation cell. By either solving Newton's Equation of Motion (in MD and

DPD) or statistical sampling (in MC), the equilibrium distribution of molecules can be generated. Then the surface tension can be calculated with the pressure tensor method[30] or test area method[42]. Thanks to the development of computer algorithms and software packages[43, 44, 45, 46, 47], and rigorous force fields[48, 49], the interfacial properties of more realistic systems[50, 51] can be investigated with great accuracy. However, at the current time, molecular simulations are still considerably slower than theoretical approaches such as DFT and DGT when calculating interfacial tension and the distribution of trace components cannot be dealt with very efficiently by simulation approaches due to the large number of molecules needed to simulate such systems. Additionally, the free energy of the system is not readily available making the calculation of some quantities such as chemical potentials less convenient compared with DFT and DGT.

1.5 Enhanced Oil Recovery

Oil recovery processes involve three stages: primary recovery, secondary recovery, and tertiary recovery(enhanced oil recovery)[52]. In the primary recovery stage, oil is produced by the high pressure inside the reservoir. As the production and depletion of oil proceed, the reservoir pressure declines causing the loss of driving force. A pump can be used to produce oil at low rates. To increase production rate, an external fluid such as gas or water can be injected into the reservoir to increase pressure. The injected fluid can also help displace the crude oil. The use of external fluids to maintain reservoir pressure is called secondary recovery which reaches its limit when a large amount of injected fluid is produced from the production well. Only about a third of original oil in place(OOIP) can be produced by primary recovery and secondary recovery[53], due to high interfacial tension between oil and water,

unfavorable wettability of rock surface and poor mobility control. To overcome these issues, chemicals and heat can be introduced. This stage is called tertiary recovery or enhanced oil recovery(EOR)[52].

Major EOR techniques may involve chemical EOR, miscible flooding, and thermal methods. In chemical EOR, chemicals such as surfactant, alkali and polymers are usually involved[54, 55, 56]. Surfactant can reduce the interfacial tension between reservoir fluids and alter the wettability of rock surfaces, that helps release the oil droplets originally trapped inside the rock pores. The EOR approach using surfactant is called surfactant flooding. Although it has been shown to be an effective approach, the expense of surfactant is usually very high making it less economical. Alkali can react with the organics in the crude oil and produce soap that is a natural surfactant. So by injecting alkali, surfactant can be produced in-situ and IFT can be reduced[57]. Furthermore, it has been shown that the addition of relatively economic alkali can reduce the adsorption of more expensive surfactant[58]. The efficiency of this approach depends on the acid number of the crude oil. Rather than decreasing interfacial tension, polymers with high viscosity can help provide mobility control of the injected fluid and increase the sweep efficiency. However, polymers cannot prevent oil trapping by capillary forces. Similar to surfactant, polymers are expensive and high salinity and temperature in the reservoirs may cause serious chemical and thermal degradation resulting in the loss of performance[59]. Alternatively, foam can be used. Foam has been shown to be a promising alternative to polymers for mobility control[60]. These three techniques can be used simultaneously and the resulting approach is called the alkaline-surfactant-polymer(ASP) flooding[61].

In addition to chemical EOR, miscible flooding can be applied. Solvents and gases such as supercritical CO₂ that are miscible with the crude oil can be injected which

has been shown to enhance the microscopic displacement efficiency[62]. However, due to the difference in density and viscosity, the miscible fluids can preferentially flow over(gravity override) or finger through the oil phase resulting in poor sweep efficiency. To resolve this issue, as mentioned, foam or polymers can be introduced for mobility control purpose.

1.6 Challenges

Challenges are remaining in EOR processes related to the interfacial phenomena and the use of amphiphilic molecules. In this thesis, we mainly focus on several.

One of the challenges is to efficiently screen surfactant formulation for better performance in surfactant flooding process. In surfactant flooding, surfactant formulation that generates ultra-low interfacial tension is required. Ultra-low interfacial tension usually appears with the formation of a middle-phase microemulsion. To reach optimal surfactant formulation, a great amount of effort is needed for conducting surfactant formulation scan experiments seeking the middle-phase microemulsion. These experiments can be time-consuming and costly. To make the process more efficient, theories can be developed and applied to predict the properties of surfactant systems and save experimental efforts. However, predictive approaches are still rare to find in the literature and left to be developed.

Another challenge is to understand the foam boosting effect of lauryl betaine in Foam EOR processes and the interaction between zwitterionic lauryl betaine and anionic surfactants. Foam has been regarded as a promising alternative to conventional high molecular weight polymers for mobility control purposes in EOR processes. For foam to be effective in mobility control, it has to be relatively strong and stable. Although it has been shown experimentally that lauryl betaine can greatly increase the

stability of foam generated by a mixture of gas, water and anionic surfactants, the mechanism behind it is not well understood. Efforts need to be made to understand the mechanism which will allow rational design of efficient and economic foaming agents.

The third challenge of interest is to develop new techniques for the wettability alteration of carbonate reservoirs. Although originally water-wet, carbonates can be preferentially oil-wet under reservoir conditions in contact with reservoir fluids. The oil-wet state of carbonates is not preferred in oil recovery process since it can prevent water from spontaneous imbibition and trap oil inside the rock pores due to capillarity. If the carbonate surfaces can be modified to water-wet, the injecting fluid(water) can invade into small pores in the rock matrix and displace oil more effectively, resulting in increased oil recovery efficiency. New technologies are needed for this purpose, and a molecular level understanding of the interactions between reservoir rock surfaces and organic acids can be helpful.

1.7 Scope of the thesis

This thesis is confined to study the interfacial phenomena related to surfactants and amphiphilic molecules aiming to provide insight and help overcome the challenges mentioned previously.

Chapter 2 gives an introduction to the interfacial statistical association fluid theory(iSAFT) density functional theory(DFT) approach. The formulations used to conduct iSAFT calculations in Chapter 3 and Chapter 4 are summarized. The extension of iSAFT describing electrostatic interactions is also covered.

In Chapter 3, an iSAFT approach based on force acting through the interface and the Method of Moments was developed to predict the effect of surfactant architecture

on the type of microemulsions formed. The stress that describes the local force in the interface obtained from iSAFT was verified against molecular dynamics simulation approach, and the dependence of the types of microemulsions on surfactant architecture agrees qualitatively with experimental observation. Additionally, the effect of surfactant structure on the phase inversion temperature can be captured. With properly determined surfactant parameters, this new approach will enable efficient screening of surfactant formulations for optimal surfactant flooding.

Chapter 4 discusses an extension of iSAFT to model the formation of spherical surfactant aggregates(micelles) in water and oil/water mixture. Compared with molecular simulation approach, DFT approach models the true thermodynamic equilibrium state between micelles and surfactant monomers and provides a unified theoretical framework for predicting the properties of surfactants in the bulk region and interfacial region. This new application of iSAFT DFT enables us to predict complete interfacial tension isotherms. Additionally, this approach can be used to study swollen micelles and inverse swollen micelles that may enable us to gain better understanding of the formation of a middle-phase microemulsion.

Chapter 5 provides insight into the mechanism of lauryl betaine as foam booster. Using molecular dynamics simulations, a system of LB (the foam booster) and alpha olefin sulfonate (AOS-14), an anionic surfactant that is used as a foam stabilizer, was studied. It was found that the foam booster functions by screening the interaction between the anionic surfactant. Favorable interaction between foam booster and anionic surfactants leads to a closer packing of the monolayer than possible with just the pure anionic surfactant. It was also found that the closer packing is also reflected in an elevated surface dilatational modulus, indicating that the closer packed monolayer will stabilize the foam. This work offers insights that can be potentially

useful in the rational design of surfactant blends for use in enhanced oil recovery.

In Chapter 6, the adsorption of naphthenic acids on calcite surface was studied by molecular dynamics simulation and the free energy of adsorption is calculated by umbrella sampling technique. It was found that, aside from electrostatic interaction, the hydrophobic attraction between acid molecules and calcite surface is also important in the adsorption process. The adsorption free energy can be enhanced by increasing the tail size of naphthenic acids. Further, the adsorption at room temperature was shown to be entropically driven and increases with the increase of temperature, which is consistent with experimental observation.

Chapter 7 summarizes the thesis and suggests future research directions.

Chapter 2

Theoretical Background

In the following, details of the potential models and iSAFT DFT are described.

2.1 Potential Models

The Statistical Associating Fluid Theory (SAFT)[63] has shown great success in modeling phase behavior of polyatomic associating fluids. In this approach, molecules are modeled as chains of segments. All the segments are spherical with hard sphere diameter σ that also interact through a Lennard-Jones potential and directional hydrogen bonding sites. As the generalization of the SAFT, interfacial Statistical Associating Fluid Theory (iSAFT) allows the prediction of interfacial properties[64, 65] and meso-scale structure of complex fluids. In the bulk, iSAFT reduces to the SAFT form.

The segment-segment hard sphere repulsion and long-range attraction are modeled with the pair potential

$$u_{\alpha\beta}(r) = \begin{cases} \infty & r < \sigma_{\alpha\beta}, \\ u_{\alpha\beta}^{LJ}(r_{\min}) - u_{\alpha\beta}^{LJ}(r_c) & \sigma_{\alpha\beta} \leq r < r_{\min}, \\ u_{\alpha\beta}^{LJ}(r) - u_{\alpha\beta}^{LJ}(r_c) & r_{\min} \leq r < r_c, \\ 0 & r \geq r_c \end{cases} \quad (2.1)$$

where $u_{\alpha\beta}^{LJ}$ represents the Lennard-Jones potential, r is the distance between segment α and β , $\sigma_{\alpha\beta}$ is the cross species hard sphere diameter determined by specific mixing

rules, r_{min} represents the Lennard-Jones potential minimum, and r_c denotes the cutoff radius which is set to $4\sigma_{\alpha\beta}$.

The Lennard-Jones potential $u_{\alpha\beta}^{LJ}$ is defined as

$$u_{\alpha\beta}^{LJ}(r) = 4\varepsilon_{\alpha\beta} \left[\left(\frac{\sigma_{\alpha\beta}}{r} \right)^{12} - \left(\frac{\sigma_{\alpha\beta}}{r} \right)^6 \right] \quad (2.2)$$

where $\varepsilon_{\alpha\beta}$ is the depth of attraction well between segment α and β that is determined by specific mixing rules. In this work, cross interaction parameters for Lennard-Jones interactions of two unlike segments α and β are given by

$$\varepsilon_{\alpha\beta} = \sqrt{\varepsilon_{\alpha}\varepsilon_{\beta}}(1 - k_{\alpha\beta}) \quad \sigma_{\alpha\beta} = \frac{\sigma_{\alpha} + \sigma_{\beta}}{2} \quad (2.3)$$

where ε_{α} and ε_{β} are Lennard-Jones interaction energies of segments α and β respectively; while σ_{α} and σ_{β} are diameters of segments α and β respectively. $k_{\alpha\beta}$ is the binary interaction parameter for the two segments.

Molecules such as water and surfactants may form hydrogen bonds. The association between molecules is described by a directional attractive potential between association sites as shown in Figure 2.1. An orientationally dependent square well potential is used to model the hydrogen bonding interaction energy given by

$$u_{AB}^{assoc}(r, \Omega_{\alpha}, \Omega_{\beta}) = \begin{cases} -\varepsilon_{assoc} & r < r_{c,assoc}; \theta_A < \theta_c; \theta_B < \theta_c, \\ 0 & otherwise \end{cases} \quad (2.4)$$

where ε_{assoc} denotes the association energy between association site A on segment α and association site B on segment β . $r_{c,assoc}$ is the cutoff distance within which association can occur. Ω_{α} and Ω_{β} are the orientations of segments α and β respectively. θ is the angle between the vector pointing from the center of a segment to the center of the association site on that segment and the vector pointing from the center of one segment (α or β) to the center of the other segment (β or α). Association can

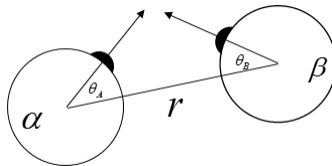


Figure 2.1 : Potential Model for Association

only occur when these two angles are smaller than the cutoff value θ_c (Figure 2.1). The cutoff distance and the angular cutoffs are chosen to allow only one bond per association site.

In this work, potential parameters for water and oil are fit to saturated liquid densities and vapor pressures. The surfactant is constructed in the same spirit as the Telo de Gama and Gubbins model[66] where the surfactants include segments with water-like parameters and segments with alkane-like parameters. Here, we explicitly include hydrogen bonding which was not present in Telo de Gama and Gubbins model. The schematics of model water, octane and surfactant molecules are shown in Figure 2.2. For example, water is modeled as a sphere with four association sites: two electron donor and two electron acceptor sites. Fitting of the model parameters is described in the Parameter Estimation Section.

2.2 interfacial Statistical Associating Fluid Theory

Based on the potential models, the iSAFT free energy functional of the system A can be constructed. In the framework of thermodynamic perturbation theory, A is given by the summation of various contributions, i.e. ideal gas contribution A^{id} , hard sphere contribution A^{hs} , long range attraction contribution A^{att} , association contribution A^{assoc} , and contribution due to the covalent bond between segments to

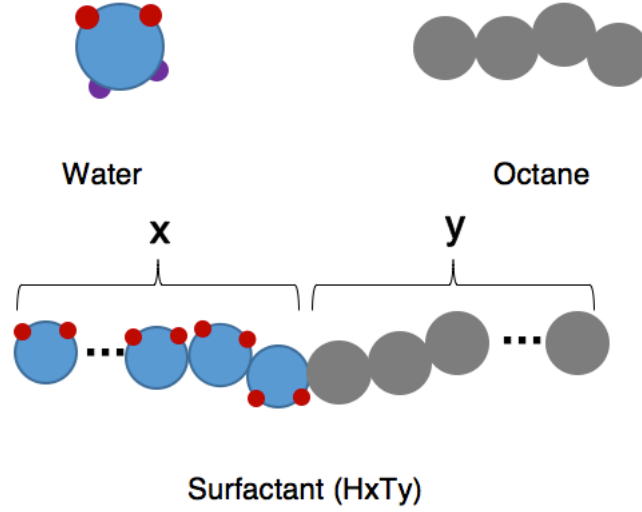


Figure 2.2 : Schematics of water, octane and amphiphilic chain constructure within the Telo da Gama and Gubbins model.

form chain-like molecules A^{chain} . In the following, we review expressions of Helmholtz free energy due to these different contributions. More details can be found in the original publications by Jain et al.[67] and Bymaster et al.[68] .

The ideal gas contribution for a mixture of spheres is exactly known from statistical mechanics[69],

$$A^{id} [\{\rho_\alpha\}] = k_B T \int d\vec{r} \sum_{\alpha=1}^N \rho_\alpha(\vec{r}) (\ln(\rho_\alpha(\vec{r})) - 1) \quad (2.5)$$

where ρ_α is the density of segment α , N is the number of different types of segments in the system so the summation is conducted over all segments, k_B is the Boltzmann constant, and T is the absolute temperature. The de Broglie wavelength is neglected since it does not affect fluid structure.

The hard sphere contribution to the Helmholtz free energy is considered by em-

ploying Rosenfeld's fundamental measure theory (FMT)[70],

$$A^{hs}[\{\rho_\alpha\}] = k_B T \int d\vec{r} \Phi[\{n_\alpha(\vec{r})\}] \quad (2.6)$$

where $\Phi[\{n_\alpha\}]$ is given by

$$\begin{aligned} \Phi[\{n_\alpha(\vec{r})\}] = & -n_0 \ln(1 - n_3) + \frac{n_1 n_2}{1 - n_3} + \frac{n_2^3}{24\pi(1 - n_3)^2} \\ & - \frac{\vec{n}_{V1} \cdot \vec{n}_{V2}}{1 - n_3} - \frac{n_2(\vec{n}_{V1} \cdot \vec{n}_{V2})}{8\pi(1 - n_3)^2} \end{aligned} \quad (2.7)$$

n_i ($i = 0, 1, 2, 3, V1, V2$) are FMT weighted densities given by

$$n_i(\vec{r}) = \sum_{\alpha=1}^N n_{i,\alpha}(\vec{r}) = \sum_{\alpha=1}^N \int \rho_\alpha^{seg}(\vec{r}_1) \omega_\alpha^{(i)}(\vec{r} - \vec{r}_1) d\vec{r}_1, \quad i = 0, 1, 2, 3, V1, V2 \quad (2.8)$$

where $\omega_\alpha^{(2)}(r) = \delta(R_\alpha - r)$, $\omega_\alpha^{(3)}(r) = \Theta(R_\alpha - r)$, $\vec{\omega}_\alpha^{(V2)}(\vec{r}) = \frac{\vec{r}}{r} \delta(R_\alpha - r)$, $\omega_\alpha^{(0)}(r) = \frac{\omega_\alpha^{(2)}(r)}{4\pi R_\alpha^2}$, $\omega_\alpha^{(1)}(r) = \frac{\omega_\alpha^{(2)}(r)}{4\pi R_\alpha}$, and $\vec{\omega}_\alpha^{(V1)}(\vec{r}) = \frac{\omega_\alpha^{(V2)}(\vec{r})}{4\pi R_\alpha}$. $\delta(R_\alpha - r)$ is the Dirac delta function and $\Theta(R_\alpha - r)$ is the Heaviside step function, where R_α is the radius of segment α .

The Helmholtz free energy resulting from long-range attraction is considered by neglecting the detailed correlation between segments (mean-field approximation)[71],

$$A^{att}[\{\rho_\alpha\}] = \frac{1}{2} k_B T \sum_{\alpha=1}^N \sum_{\beta=1}^N \int_{|\vec{r}_2 - \vec{r}_1| > \sigma_{\alpha\beta}} d\vec{r}_1 d\vec{r}_2 u_{\alpha\beta}(|\vec{r}_2 - \vec{r}_1|) \rho_\alpha(\vec{r}_1) \rho_\beta(\vec{r}_2) \quad (2.9)$$

where $u_{\alpha\beta}$ is given in Eq.(2.1).

The Helmholtz free energy due to association was derived from Wertheim's theory[72, 73, 74, 75]. It can be written as[68, 76, 77],

$$A^{assoc}[\{\rho_\alpha\}] = k_B T \int d\vec{r}_1 \sum_{\alpha=1}^N \rho_\alpha(\vec{r}_1) \sum_{A \in \Gamma(\alpha)} \left(\ln X_A^\alpha(\vec{r}_1) - \frac{X_A^\alpha(\vec{r}_1)}{2} + \frac{1}{2} \right) \quad (2.10)$$

where X_A^α is the fraction of association sites A on segments α which are not bonded.

This fraction is given by $X_A^\alpha(\vec{r}_1) = \frac{1}{1 + \sum_{\alpha'=1}^N \int d\vec{r}_2 \rho_{\alpha'}(\vec{r}_2) \sum_{B \in \Gamma(\alpha')} X_B^{\alpha'}(\vec{r}_2) \Delta^{\alpha\alpha'}(\vec{r}_1, \vec{r}_2)}$, where α'

represents the segments which can associate or form hydrogen bond with segments α , $\Gamma^{(\alpha')}$ denotes all association sites on segment α' , and $\Delta^{\alpha\alpha'}(\vec{r}_1, \vec{r}_2)$ is given by

$$\Delta^{\alpha\alpha'}(\vec{r}_1, \vec{r}_2) = \kappa[\exp(\beta\varepsilon_{assoc}) - 1]y^{\alpha\alpha'}(\vec{r}_1, \vec{r}_2) \quad (2.11)$$

where κ is a bonding geometric constant, β is the inverse temperature $\frac{1}{k_B T}$, ε_{assoc} is the association energy, and $y^{\alpha\alpha'}(\vec{r}_1, \vec{r}_2)$ is the inhomogeneous cavity correlation function of the reference hard sphere fluid. Assuming that the potential of mean force is pairwise additive and using a weighted density approximation, this function can be approximated as[36, 78],

$$y^{\alpha\alpha'}(\vec{r}_1, \vec{r}_2) = \sqrt{y_{contact}^{\alpha\alpha'}[\{\bar{\rho}_\alpha(\vec{r}_1)\}]y_{contact}^{\alpha\alpha'}[\{\bar{\rho}_\alpha(\vec{r}_2)\}]} \quad (2.12)$$

where $y_{contact}^{\alpha\alpha'}[\{\bar{\rho}_\alpha(\vec{r})\}]$ is the bulk cavity correlation function at contact evaluated at weighted densities $\{\bar{\rho}_\alpha\}$. In this work, $y_{contact}^{\alpha\alpha'}[\{\bar{\rho}_\alpha(\vec{r})\}]$ is given by[78],

$$y_{contact}^{\alpha\alpha'}[\{\bar{\rho}_\alpha(\vec{r}_1)\}] = \frac{1}{1 - \bar{\varsigma}_3} + \frac{3\sigma_\alpha\sigma_{\alpha'}}{\sigma_\alpha + \sigma_{\alpha'}} \frac{\bar{\varsigma}_2}{(1 - \bar{\varsigma}_3)^2} + 2\left(\frac{\sigma_\alpha\sigma_{\alpha'}}{\sigma_\alpha + \sigma_{\alpha'}}\right)^2 \frac{(\bar{\varsigma}_2)^2}{(1 - \bar{\varsigma}_3)^3} \quad (2.13)$$

where $\bar{\varsigma}_i$ is given by

$$\bar{\varsigma}_i = \frac{\pi}{6} \sum_{\alpha=1}^N \bar{\rho}_\alpha(\vec{r}_1) \sigma_\alpha^i, \quad i = 0, 1, 2, 3 \quad (2.14)$$

The weighted densities in the above equations are

$$\bar{\rho}_\alpha(\vec{r}_1) = \frac{3}{4\pi\sigma_\alpha^3} \int_{|\vec{r}' - \vec{r}_1| < \sigma_\alpha} d\vec{r}' \rho_\alpha(\vec{r}') \quad (2.15)$$

By taking the limit $\varepsilon_{assoc} \rightarrow \infty$, we reach complete association and chain formation. The free energy due to chain formation A^{chain} can be directly derived from A^{assoc} (see the original publication[67] for more details).

As of now, the total Helmholtz free energy is obtained

$$A = A^{id} + A^{hs} + A^{att} + A^{assoc} + A^{chain} \quad (2.16)$$

The grand potential of a grand canonical ensemble, where volume V , temperature T , and chemical potential μ of each species are fixed, can be written as

$$\Omega[\{\rho_\alpha\}] = A[\{\rho_\alpha\}] - \sum_{\alpha=1}^N \int d\vec{r}' \rho_\alpha(\vec{r}') (\mu_\alpha - V_\alpha^{ext}(\vec{r}')) \quad (2.17)$$

where μ_α is the chemical potential of segments α , and V_α^{ext} is the external potential acting on segments α .

By minimizing the grand potential with respect to densities, the equilibrium density profiles $\rho_\alpha^{\text{equilibrium}}(\vec{r})$ can be obtained.

$$\left. \frac{\delta \Omega[\{\rho_\alpha\}]}{\delta \rho_\alpha(\vec{r})} \right|_{\rho_\alpha^{\text{equilibrium}}} = 0, \quad \forall \alpha \in \{1, 2, \dots, N\} \quad (2.18)$$

Combining Eq.(2.17) and Eq.(2.18) gives

$$\left. \frac{\delta \beta A[\{\rho_\alpha\}]}{\delta \rho_\alpha(\vec{r})} \right|_{\rho_\alpha^{\text{equilibrium}}} = \beta(\mu_\alpha - V_\alpha^{ext}(\vec{r})), \quad \forall \alpha \in \{1, 2, \dots, N\} \quad (2.19)$$

Solving Eq.(2.19) requires functional derivatives of the Helmholtz free energy functionals. They are given by

$$\frac{\delta \beta A^{id}}{\delta \rho_\alpha(\vec{r})} = \ln \rho_\alpha(\vec{r}) \quad (2.20)$$

$$\frac{\delta \beta A^{hs}}{\delta \rho_\alpha(\vec{r})} = \int d\vec{r}_1 \frac{\delta \Phi[n_\beta(\vec{r}_1)]}{\delta \rho_\alpha(\vec{r})} \quad (2.21)$$

$$\frac{\delta \beta A^{att}}{\delta \rho_\alpha(\vec{r})} = \sum_{\beta=1}^N \int_{|\vec{r}-\vec{r}_1|>\sigma_{\alpha\beta}} d\vec{r}_1 \beta u_{\alpha\beta}^{att}(|\vec{r}-\vec{r}_1|) \rho_\alpha(\vec{r}_1) \quad (2.22)$$

$$\frac{\delta \beta A^{assoc}}{\delta \rho_\alpha(\vec{r})} = \sum_{A \in \Gamma^{(\alpha)}} \ln X_A^\alpha(\vec{r}) - \frac{1}{2} \sum_{\gamma=1}^N \sum_{\gamma'}^{\{\gamma'\}} \int \rho_\gamma(\vec{r}_1) \sum_{A \in \Gamma^{(\gamma)}} (1 - X_A^\gamma(\vec{r}_1)) \frac{\delta \ln y_{contact}^{\gamma\gamma'}[\{\bar{\rho}_\alpha(\vec{r}_1)\}]}{\delta \rho_\alpha(\vec{r})} d\vec{r}_1 \quad (2.23)$$

$$\frac{\delta \beta A^{chain}}{\delta \rho_\alpha(\vec{r})} = \sum_{B \in \Gamma^{(\alpha)}} \ln X_B^\alpha(\vec{r}) - \frac{1}{2} \sum_{\gamma=1}^N \sum_{\gamma'}^{\{\gamma'\}} \int \rho_\gamma(\vec{r}_1) \frac{\delta \ln y_{contact}^{\gamma\gamma'}[\{\bar{\rho}_\alpha(\vec{r}_1)\}]}{\delta \rho_\alpha(\vec{r})} d\vec{r}_1 \quad (2.24)$$

where $\Gamma^{(\alpha)}$ denotes the set of association sites on segment α and $\{\gamma'\}$ represents the set of segment that can bond(associate) with segment γ in chain term(association term).

As mentioned above, we have chain formation when association energy is infinity. By $\varepsilon_{assoc} \rightarrow \infty$ and $X_A \rightarrow 0$, Eq. (2.23) reduces to Eq. (2.24). Note that sites A and sites B are conceptually different. Sites A in Eq. (2.23) denotes association sites that form hydrogen bonds, while sites B in Eq. (2.24) represents the sites involved in covalent bonds.

After obtaining the functional derivatives, Equation 2.19 can be solved iteratively. By further numerical manipulation, Equation 2.19 can be written in the following form[67]:

$$\rho_\alpha(\vec{r}) = \exp(\beta\mu_M) \exp[D_\alpha(\vec{r}) - \beta V_\alpha^{ext}(\vec{r})] I_{1,\alpha}(\vec{r}) I_{2,\alpha}(\vec{r}), \forall \alpha \in \{1, 2, \dots, N\} \quad (2.25)$$

where μ_M is the chemical potential of chain M ($\mu_M = \sum_{i=1}^{i=m} \mu_i$), m is the length of the chain molecule, $D_\alpha(\vec{r}_\alpha)$ is a function taking into account the excess free energy functional derivatives and will be given below, and $I_1(I_2)$ takes into account the chain connectivity.

$$D_\alpha(\vec{r}) = \frac{1}{2} \sum_{\gamma=1}^N \sum_{\gamma'}^{\{\gamma'\}} \int \rho_\gamma(\vec{r}_1) \frac{\delta \ln y_{contact}^{\gamma\gamma'}[\{\bar{\rho}_\alpha(\vec{r}_1)\}]}{\delta \rho_\alpha(\vec{r})} d\vec{r}_1 - \frac{\delta \beta A^{hs}}{\delta \rho_\alpha(\vec{r})} - \frac{\delta \beta A^{att}}{\delta \rho_\alpha(\vec{r})} - \frac{\delta \beta A^{assoc}}{\delta \rho_\alpha(\vec{r})} \quad (2.26)$$

$$I_{1,\alpha}(\vec{r}) = \begin{cases} 1, \alpha = 1 \\ \int I_{1,\alpha-1}(\vec{r}^j) \exp[D_{\alpha-1}(\vec{r}^j) - \beta V_{\alpha-1}^{ext}(\vec{r}^j)] \Delta^{(\alpha-1,\alpha)}(\vec{r}, \vec{r}^j) d\vec{r}^j, \alpha > 2 \end{cases} \quad (2.27)$$

$$I_{2,\alpha}(\vec{r}) = \begin{cases} 1, \alpha = m \\ \int I_{2,\alpha+1}(\vec{r}^j) \exp[D_{\alpha+1}(\vec{r}^j) - \beta V_{\alpha+1}^{ext}(\vec{r}^j)] \Delta^{(\alpha,\alpha+1)}(\vec{r}, \vec{r}^j) d\vec{r}^j, \alpha < m \end{cases} \quad (2.28)$$

where m represents the length of one chain molecule, and Δ is given in Equation 2.11.

To solve for the equilibrium density profile and interfacial properties, a simple Picard iteration is utilized but other techniques such as Newton-Raphson method

can also be applied.

Once the equilibrium density profile was obtained, the interfacial properties such as interfacial tension or more interesting stress profile which will be used in Chapter 3 can be calculated. It has been shown by Frink et al.[79] that the stress($P_N - P_T$, where P_N is the normal pressure and P_T is the tangential pressure) is essentially the local excess grand potential. From iSAFT, this quantity can be calculated by the following expression for a planar interface:

$$\begin{aligned} \beta s(\vec{r}) = & \sum_{\alpha=1}^N \rho_{\alpha}(\vec{r}) [D_{\alpha}(\vec{r}) + \frac{n(\Gamma^{\alpha})}{2} - 1] + \Phi(\{n_{\alpha}(\vec{r})\}) + \\ & \frac{1}{2} \sum_{\alpha=1}^N \sum_{\beta=1}^N \int_{|\vec{r}-\vec{r}_1| > \sigma_{\alpha\beta}} d\vec{r}_1 \beta u_{\alpha\beta}^{att}(|\vec{r}-\vec{r}_1|) \rho_{\alpha}(\vec{r}_1) \rho_{\beta}(\vec{r}) + \\ & \sum_{\alpha=1}^N \rho_{\alpha}(\vec{r}) \sum_{A \in \Gamma(\alpha)} (\ln X_A^{\alpha}(\vec{r}) - \frac{X_A^{\alpha}(\vec{r})}{2} + \frac{1}{2}) + \beta P \end{aligned} \quad (2.29)$$

where P is the bulk pressure, s denotes the stress, and the meaning of the rest of variables is the same as previously introduced.

2.3 Electrostatic iSAFT

2.3.1 Electrostatic Functional

To describe electrostatic interactions by density functional theory, the electrostatic Helmholtz free energy functional needs to be developed and included. The Helmholtz free energy contribution can be included in the original iSAFT theory as a perturbation from the reference hard sphere fluid. Based on Coulomb's law, the Helmholtz free energy can be written as

$$\beta A^{ex,C}[\{\rho_i\}] = \frac{1}{2} \sum_{i=1}^n \sum_{j=1}^n \int d\vec{r}_1 d\vec{r}_2 \beta \frac{Z_i Z_j e^2 \rho_i(\vec{r}_1) \rho_j(\vec{r}_2)}{4\pi \epsilon_0 \epsilon_r |\vec{r}_2 - \vec{r}_1|} \quad (2.30)$$

where $\beta A^{ex,C}$ represents the excess free energy due to direct electrostatic interaction between the ions, Z_i is the valence, e is the elementary charge, and $\varepsilon_0\varepsilon_r$ gives the permittivity of the solvent. So this expression is based on a primitive model assumption. Although the form of this electrostatic free energy functional is simple and easy to understand, it is hard to converge due to the long-range nature of electrostatic interactions. What's more, it can be observed that a mean field approximation is applied since no radial distribution function describing the electrolyte structure can be seen in the above equation.

Instead of solving the equation above, the electrostatic contribution can be calculated from the local mean electrostatic potential.

$$\beta A^{ex,C}[\{\rho\}] = \frac{1}{2}\beta e \sum_{j=1}^n \int d\vec{r}_2 Z_j \rho_j(\vec{r}_2) \psi(\vec{r}_2) \quad (2.31)$$

where ψ represents the local mean electrostatic potential and can be recognized as the summation of electrostatic potentials of individual point charges.

$$\psi(\vec{r}) = \int d\vec{r}_1 \sum_{i=1}^n \frac{Z_i e \rho_i(\vec{r}_1)}{4\pi\varepsilon |\vec{r} - \vec{r}_1|} \quad (2.32)$$

where ε is the dielectric constant $\varepsilon_0\varepsilon_r$, and ρ_i is the density of ion with index i .

This local mean electrostatic potential satisfies the Poisson's equation. In 1-D, Poisson's equation can be read as[80]

$$\frac{d}{dz} \left(\varepsilon \frac{d}{dz} \psi(z) \right) = -4\pi\rho_c(z) \quad (2.33)$$

where ρ_c is the charge density $(\sum_{i=1}^n Z_i \rho_i)$.

The equation can be solved by imposing proper boundary conditions. To calculate charge distribution close to a charged surface, one boundary condition could be $\frac{d}{dz}\psi(z)$ is 0 when z is sufficiently large. This boundary condition assumes that the

mean electrostatic potential caused by the charged surface can be negligible when the distance from the surface is large enough and the property of the fluid reaches its bulk property. The other boundary condition could be $\psi(z)$ is 0 when z is sufficiently large.

The integrated form of the Poisson's equation is given as following[81]

$$\psi^*(z) \equiv \beta e \psi(z) = 4\pi l_B \sum_{i=1}^n \int_z^\infty dz' (z - z') Z_i \rho_i(z') \quad (2.34)$$

where l_B is the Bjerrum length given by $l_B = \frac{e^2}{4\pi\epsilon_0\epsilon_r k_B T}$. k_B is Boltzmann constant, and T is the absolute temperature. An equivalent form can be derived based on this equation and it is given by

$$\psi^*(z) = \psi^*(0) + 4\pi l_B \left[\int_z^\infty dz' z \sum_i Z_i \rho_i(z') + \int_0^z dz' z' \sum_i Z_i \rho_i(z') \right] \quad (2.35)$$

where $\psi^*(0)$ is the electrostatic potential at the charged surface.

The local chemical potential due to direct Coulomb interaction can be recovered,

$$\frac{\delta \beta A^{ex,C}}{\delta \rho_i(z)} = Z_i \psi^*(z) \quad (2.36)$$

Plugging in this equation in the original Euler-Lagrange equation described before leads to the following equation, based on which the equilibrated density profile can be calculated,

$$D_\alpha(\vec{r}) = \frac{1}{2} \sum_{\gamma=1}^N \int \rho_\gamma(\vec{r}_1) \frac{\delta \ln y_{contact}^{\gamma\gamma}[\{\bar{\rho}_\alpha(\vec{r}_1)\}]}{\delta \rho_\alpha(\vec{r})} d\vec{r}_1 - \frac{\delta \beta A^{hs}}{\delta \rho_\alpha(\vec{r})} - \frac{\delta \beta A^{att}}{\delta \rho_\alpha(\vec{r})} - \frac{\delta \beta A^{assoc}}{\delta \rho_\alpha(\vec{r})} - \frac{\delta \beta A^{ex,C}}{\delta \rho_\alpha(\vec{r})} \quad (2.37)$$

$$\rho_\alpha(z) = \exp(\beta\mu_M) \exp[D_\alpha(z) - Z_\alpha \psi^*(z) - \beta V_\alpha^{ext}(z)] I_{1,\alpha}(z) I_{2,\alpha}(z) \quad (2.38)$$

2.3.2 Electrostatic Correlation

The electrostatic interaction described in the previous section neglects the short range correlation between ions. Although it was found to be adequate at least for monovalent ions[82], the theory may fail when divalent ions are present. This electrostatic correlation effect can be included by approximating electrostatic free energy functional by a quadratic functional Taylor expansion with respect to that of a bulk fluid of densities ρ_i^b .

$$A^{ex,elec}[\{\rho_i\}] = A^{ex,elec}[\{\rho_i^b\}] + \int d\vec{r} \sum_{i=1}^n \frac{\delta F^{ex,elec}}{\delta \rho_i(\vec{r})} [\rho_i(\vec{r}) - \rho_i^b] + \frac{1}{2} \int \int d\vec{r} d\vec{r}' \sum_{j=1}^n \sum_{i=1}^n \frac{\delta^2 F^{ex,elec}}{\delta \rho_i(\vec{r}) \delta \rho_j(\vec{r}')} [\rho_i(\vec{r}) - \rho_i^b] [\rho_j(\vec{r}') - \rho_j^b] + \dots \quad (2.39)$$

Recognizing that the direct correlation functions are defined as

$$\Delta C_i^{(1)el} = -\frac{\beta \delta A^{ex,elec}[\{\rho_i\}]}{\delta \rho_i(\vec{r})} \quad (2.40)$$

$$\Delta C_{ij}^{(2)el} = -\frac{\beta \delta^2 A^{ex,elec}[\{\rho_i\}]}{\delta \rho_i(\vec{r}) \delta \rho_j(\vec{r}')} \quad (2.41)$$

Neglecting the higher order terms, Equation 2.39 can be written as

$$A^{ex,elec}[\{\rho_i\}] = A^{ex,elec}[\{\rho_i^b\}] - \int d\vec{r} \sum_{i=1}^n \Delta C_i^{(1)el} [\rho_i(\vec{r}) - \rho_i^b] + \frac{1}{2} \int \int d\vec{r} d\vec{r}' \sum_{j=1}^n \sum_{i=1}^n \Delta C_{ij}^{(2)el} [\rho_i(\vec{r}) - \rho_i^b] [\rho_j(\vec{r}') - \rho_j^b] \quad (2.42)$$

Taking functional derivative of the above equation and utilizing Equation 2.36 lead to

$$\frac{\delta \beta A^{ex,elec}[\{\rho_i\}]}{\delta \rho_j(\vec{r})} = Z_i \psi^*(\vec{r}) - \sum_{i=1}^n \int d\vec{r}_2 \Delta C_{ij}^{(2)el} (|\vec{r}_2 - \vec{r}|) [\rho_i(\vec{r}_2) - \rho_i^b] \quad (2.43)$$

The excess direct correlation function $\Delta C_{ij}^{(2)el}(r)$ is defined as

$$\Delta C_{ij}^{(2)el}(r) = C_{ij}(r) + \frac{\beta Z_i Z_j e^2}{4\pi \epsilon_0 \epsilon_r r} - C_{ij}^{hs}(r) \quad (2.44)$$

This direct correlation function can be derived from OZ equation by proper closure. It can be seen that the direct correlation functions due to Coulombic interaction and hard sphere interaction are subtracted, which avoids the double counting of various contributions. The mean spherical approximation(MSA) closure assuming equal hard sphere diameter (restricted primitive model) gives

$$\Delta C_{ij}^{(2)el}(r) = \begin{cases} -Z_i Z_j l_B [\frac{2B}{\sigma} - (\frac{B}{\sigma})^2 r - \frac{1}{r}], r \leq \sigma \\ 0, r > \sigma \end{cases} \quad (2.45)$$

where

$$B = \frac{\Gamma \sigma}{1 + \Gamma \sigma} \quad (2.46)$$

and Γ is related to the Debye screening length by

$$\kappa = 2\Gamma(1 + \Gamma \sigma) \quad (2.47)$$

The Debye screening length is given by

$$\kappa^2 = 4\pi l_B \sum_{i=1}^N \rho_i^b Z_i^2 \quad (2.48)$$

Now the Euler-Lagrange equation can be solved numerically.

For semi primitive model, the MSA solution has a more complicated form [83, 84].

For $d_i < d_j$ and $0 \leq r \leq \frac{d_j - d_i}{2}$

$$\Delta C_{ij}(r) = 2l_B [\frac{Z_i Z_j}{2r} + Z_i N_j - X_i (N_i + \Gamma X_i) + \frac{d_i}{3} (N_i + \Gamma X_i)^2] \quad (2.49)$$

and for $\frac{|d_j - d_i|}{2} \leq r \leq \frac{d_j + d_i}{2}$, ΔC is given as

$$\Delta C_{ij}(r) = \frac{l_B}{r} [Z_i Z_j + (d_i - d_j) f_1 - r f_2 + r^2 f_3 + r^2 f_4] \quad (2.50)$$

where

$$f_1 = \frac{X_i + X_j}{4} [(N_i + \Gamma X_i) - (N_j + \Gamma X_j)] - \frac{d_i - d_j}{16} [(N_i + \Gamma X_i + N_j + \Gamma X_j)^2 - 4N_i N_j] \quad (2.51)$$

$$f_2 = (X_i - X_j)(N_i - N_j) + (d_i + d_j)N_i N_j + (X_i^2 + X_j^2)\Gamma - \frac{1}{3}[d_i(N_i + \Gamma X_i)^2 + d_j(N_j + \Gamma X_j)^2] \quad (2.52)$$

$$f_3 = \frac{X_i}{d_i}(N_i + \Gamma X_i) + \frac{X_j}{d_j}(N_j + \Gamma X_j) + N_i N_j - \frac{1}{2}[(N_i + \Gamma X_i)^2 + (N_j + \Gamma X_j)^2] \quad (2.53)$$

$$f_4 = \frac{(N_i + \Gamma X_i)^2}{6d_i^2} + \frac{(N_j + \Gamma X_j)^2}{6d_j^2} \quad (2.54)$$

where d is the hard sphere diameter, Z represents the valence, and N , X , and Γ are calculated numerically based on

$$X_i = \frac{Z_i}{1 + \Gamma d_i} - \frac{c d_i^2}{1 + \Gamma d_i} \frac{\sum_j^n (\rho_j d_j Z_j)/(1 + \Gamma d_j)}{1 + c \sum_j^n (\rho_j d_j^3)/(1 + \Gamma d_j)} \quad (2.55)$$

$$X_i = Z_i + N_i d_i \quad (2.56)$$

$$\Gamma^2 = \pi l_B \sum_i^n \rho_i X_i^2 \quad (2.57)$$

$$c = \frac{\pi}{2[1 - \frac{\pi}{6} \sum_i^n \rho_i d_i^3]} \quad (2.58)$$

2.3.3 Preliminary Results

Here, we show some preliminary results using iSAFT that incorporates electrostatic contribution introduced above. Since a primitive model of electrolyte is employed, we have to assign the dielectric constant. We use the relative permittivity of water ($\epsilon_r = 78.5$) at 298 K. The first testing case is the density distributions and electrostatic potential profiles of simple electrolytes close to charged surfaces. The results are compared against available simulation results from Monte Carlo simulation in the literature and presented in Figure 2.3 - 2.7. It can be seen that good agreement between the theoretical prediction and simulation can be achieved.

Then we show the results for systems of negatively charge polyelectrolyte and positive coions close to a charged surface with surface charge density $Q\sigma^2/e = 0.125$ at different bulk electrolyte concentration ($\rho\sigma^3 = 0.01, 0.06, 0.16, 0.22$). Each negatively

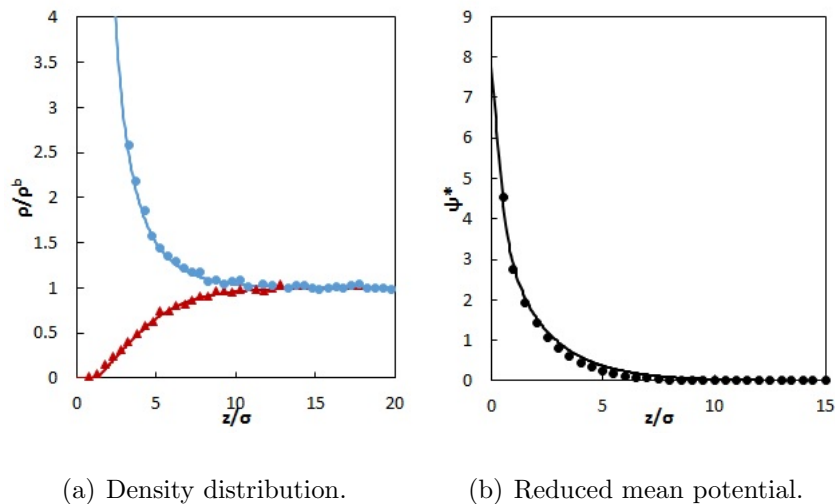
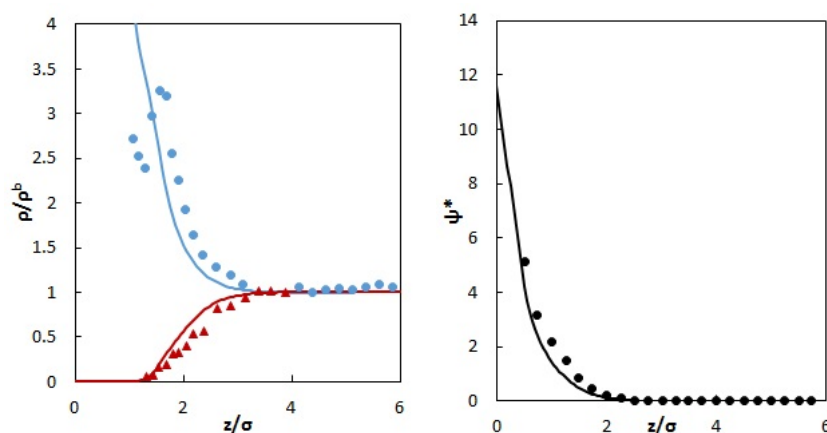


Figure 2.3 : Density distributions(normalized by bulk density) for cations(red) and anions(blue) and mean electrostatic potential in a simple 1:1 electrolyte near a positively charged surface. $\sigma_+ = \sigma_- = \sigma = 0.425$ nm, $Q\sigma^2/e = 0.3$, $C = 0.1$ mol/L, where σ is the diameter of the ion, Q is the surface charge, e is the elementary charge and C is the concentration. $\Psi^* = \Psi e/kT$, where e is the elementary charge, k is the Boltzmann constant and T is the absolute temperature. Lines are from iSAFT and dots are from Monte Carlo simulation[1].

charged polyelectrolyte chain consists of 10 tangentially bonded spherical segments ($m = 10$) with the size of 0.714 nm in diameter. So the overall valence of the polyelectrolyte is -10 . The coions are positively charged with the same size. The density profiles calculated from iSAFT are shown in Figure 2.8 along with some results from Monte Carlo simulation. Again good agreement can be found and the results are comparable to the work by Li et al.[5].

2.4 Summary

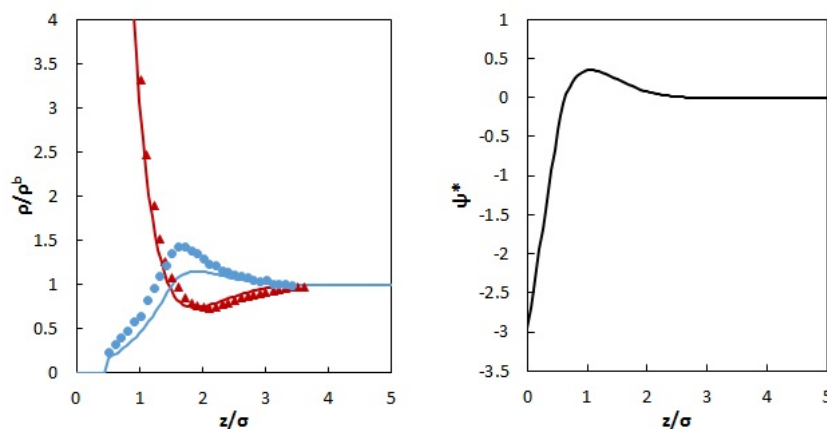
In this chapter, the background of iSAFT classical density functional theory are present. Further, iSAFT was extended to include the electrostatic contributions. Good agreement between the results from iSAFT and those from Monte Carlo simu-



(a) Density distribution.

(b) Reduced mean potential.

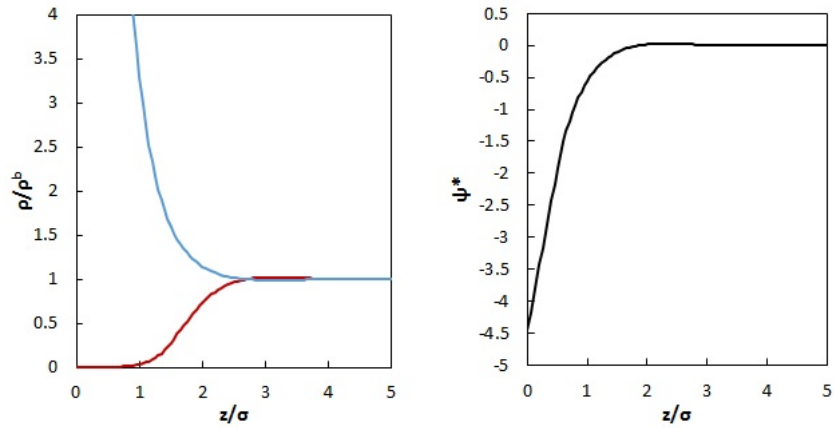
Figure 2.4 : Density distributions(normalized by bulk density) for cations(red) and anions(blue) and mean electrostatic potential in a simple 1:1 electrolyte near a positively charged surface. $\sigma_+ = \sigma_- = \sigma = 0.425$ nm, $Q\sigma^2/e = 0.7$, $C = 1$ mol/L. Lines are from iSAFT and dots are from Monte Carlo simulation[1].



(a) Density distribution.

(b) Reduced mean potential.

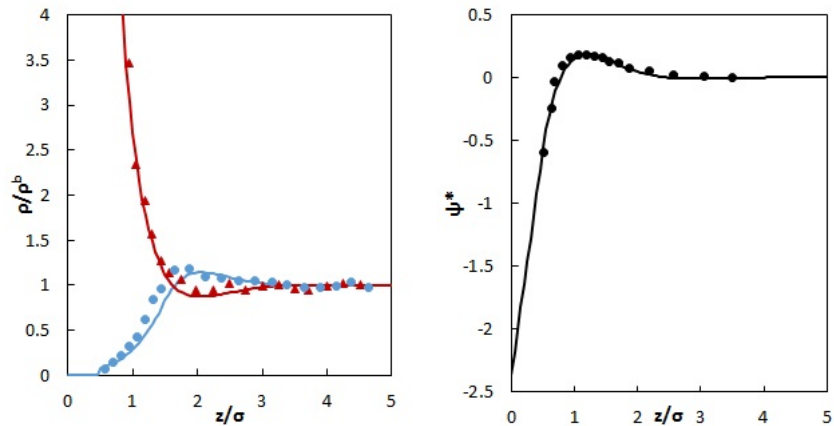
Figure 2.5 : Density distributions(normalized by bulk density) for divalent cations(red) and monovalent anions(blue) and mean electrostatic potential in a simple 2:1 electrolyte near a negatively charged surface. $\sigma_+ = \sigma_- = \sigma = 0.3$ nm, $Q\sigma^2/e = -0.1685$, $C = 1$ mol/L. Lines are from iSAFT and dots are from Monte Carlo simulation[2].



(a) Density distribution.

(b) Reduced mean potential.

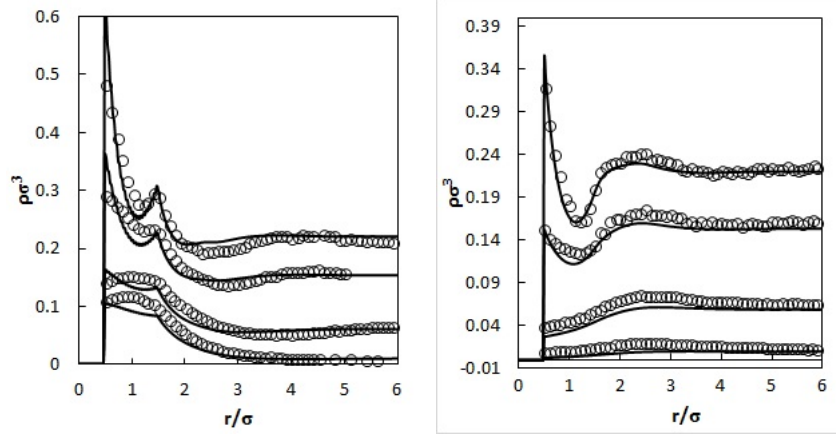
Figure 2.6 : Density distributions(normalized by bulk density) for monovalent cations(blue) and divalent anions(red) and mean electrostatic potential in a simple 1:2 electrolyte near a negatively charged surface. $\sigma_+ = \sigma_- = \sigma = 0.3$ nm, $Q\sigma^2/e = -0.1685$, $C = 1$ mol/L.



(a) Density distribution.

(b) Reduced mean potential.

Figure 2.7 : Density distributions(normalized by bulk density) for cations(red) and anions(blue) and mean electrostatic potential in a simple 2:2 electrolyte near a negatively charged surface. $\sigma_+ = \sigma_- = \sigma = 0.425$ nm, $Q\sigma^2/e = -0.1704$, $C = 0.5$ mol/L. Lines are from iSAFT and dots are from Monte Carlo simulation[3].



(a) Polyelectrolyte.

(b) Coion.

Figure 2.8 : Density distributions for polyelectrolytes and coions in a electrolyte near a positively charged surface. $\sigma = 0.714$ nm, $Q\sigma^2/e = 0.125$, $\rho\sigma^3 = 0.01, 0.06, 0.16, 0.22$. Lines are from iSAFT and dots are from monte-carlo simulation[4, 5].

lations is achieved.

Chapter 3

Method of Moments from iSAFT and the Formation of Microemulsions

Surfactants have wide range of industrial and commercial applications, i.e. shampoo, detergent, surfactant flooding in enhanced oil recovery(EOR). This chapter is related to their application in EOR processes, where ultra-low interfacial tension is required and optimal surfactant formulation is needed. The iSAFT density functional theory is applied to study the mechanical property (stress or lateral pressure) of an octane/water interface. This mechanical property can be related to Winsor R-ratio through the Method of Moments developed by Fraaije et al. [22]. By implementing the Method of Moments in iSAFT, the effects of surfactant formulation variables (temperature, surfactant tail or head size, surfactant architecture) on the formation of microemulsions can be obtained. The trend from iSAFT is in good agreement with what was observed in the experiments.

This work has been presented in the 2014 AICHE Annual Meeting[85].

3.1 Introduction

Surfactant flooding with the creation of middle-phase microemulsions has been widely used to enhance the production of crude oil[52, 54]. Only an average of 35%-45% original oil in place (OOIP) can be extracted after primary and secondary recoveries[86], with large amount of crude oil left behind in the oil reservoirs. This is largely due to the large value of interfacial tension in the reservoir and capillary trapping. Surfac-

tants, being amphiphilic, can lower the interfacial tension, so that the oil trapped originally by capillary effect can be more easily released and displaced by the injected fluids, which enhances the oil production. In surfactant flooding processes, ultra-low interfacial tension ($< 10^{-3}$ mN/m) is required. Ultra-low interfacial tension often occurs with the formation of middle-phase microemulsions[87]. To locate the optimal surfactant formulation for ultra-low interfacial tension, formulation scan techniques[88], i.e. salinity scan(ionic surfactants) and temperature scan, are followed experimentally at the conditions of interest. These scan experiments can be time-consuming and expensive with such a large formulation variable space (chemical nature of surfactant molecules, salinity, temperature, pressure, crude oil composition or alkane carbon number(ACN))[89]. To narrow down the set of variables and speed up the acquisition of optimal surfactant formulations and ultralow interfacial tension, theoretical approaches can be helpful. Following Winsor's pioneering work in the 1950s, many theoretical developments have been made to determine optimum conditions, namely surfactant affinity difference(SAD), hydrophilic-lipophilic deviation(HLD)[90], Helfrich theory[91], etc. Recently, a method based on the mechanical property of the interface(stress profile) and the theories of Helfrich[91], Murphy[92] and others[93] was developed[22] which will be discussed shortly.

The stress profile (or negative lateral pressure) across the interface dominates many interfacial phenomena and physical processes. For example, it was shown by Cantor that Anesthesia is related to the compositional response of the lateral pressure profile in bilayer membranes[94]. The change of the composition would cause the redistribution of the lateral pressure in the membrane that alters the conformation and functionality of cell proteins[95]. The lateral pressure also governs the self-assembly of particles at interfaces. Aveyard et al. showed the aggregation of

monodisperse spherical polystyrene particles at water/octane interface is due to the change of lateral pressure modulated by surfactants[96]. Long et al. studied the lateral pressure by Monte Carlo simulation and provided a unifying explanation for the phenomena observed in confined environments which only occur under very high pressure in bulk solution[97]. Related to microemulsions, the bending of surfactant layer (consequence of stress) was shown to be important and incorporated with entropy effects for the first time by Miller et al.[98] to establish a thermodynamic model for microemulsions. Fraaije et al.[22] proposed a method conceptually equivalent to Winsor-R theory based on manipulation of the stress profile to determine the formation of Winsor type microemulsions for different surfactant formulations. This method is referred to as Method of Moments. The idea is not new. Similar approach was considered by Bowcott et al.[93] and Murphy[92] dating back to 1960s. However, only thermodynamic foundation to calculate stress profile was established[99] at that time. Recently, the Method of Moments was implemented based on the stress profile calculated from Dissipative Particle Dynamics(DPD) simulation and good agreement with experiments was found. In this chapter, we will implement the method in the framework of the iSAFT density functional theory to provide insight into the effect of surfactant architecture on the formation of microemulsions.

3.2 Stress Profile from iSAFT DFT

According to Frink et al.[79], the stress profile is equal to the local excess grand potential that can be calculated directly from iSAFT density functional theory for a planar interface (See Equation 2.29). The background of iSAFT density functional theory has been provided in Chapter 2 and will not be duplicated here. The stress profile ($stress(z) = P_N - P_T(z)$) and interfacial tension are related through the me-

chanical definition of interfacial tension for a planar interface $\gamma = \int stress(z)dz = \int (P_N - P_T(z))dz$, where P_N is the normal pressure (constant throughout the interface) and P_T is the tangential pressure, the value of which depends on z . This stress profile($P_N - P_T(z)$) can provide insights into the mechanical property of the interface, which has been shown to be important in determining the bending state of the interface[92] and other phenomena[100]. To validate the iSAFT model, the density profile and stress profile obtained from iSAFT are compared against those from molecular dynamics simulation(MD).

Here, we examine a model A/B/AB ternary mixture, where molecule(bead) A and molecule(bead) B dislike each other and AB is a surfactant-like molecule consisting of A and B bonded tangentially. Beads interact with each other through Lennard-Jones potential, and two potential parameters need to be specified, namely σ and ϵ/k_b . The diameter σ of all beads is set equally to 0.3 nm and interaction energy ϵ/k_b between A or B beads is set to 300 K while that between A and B beads is set to 30 K.

Molecular dynamics simulation was performed in NVT ensemble using GROMACS 4.6.5 software package. The simulation box of size $5.5 \times 5.5 \times 11.0$ nm is filled with a slab of A(4800 A beads) and a slab of B(4800 B beads), creating two A/B interfaces due to the applied periodic boundary condition in all directions. 200 AB molecules are present in the system and they spontaneously participate at the two interfaces. The modified Berendsen thermostat[101] was used to maintain the temperature of the system to 300 K. The system was initially energy-minimized and after a short NVT simulation (100 ps) the system was equilibrated in NVT ensemble for 1 ns for data analysis. The stress profile was calculated using central force decomposition method developed by Vanegas et al.[102] and their modified GROMACS software package - GROMACS-LS is used.

The iSAFT classical density functional theory calculation of the same A/B/AB mixture was also performed using the same set of parameters under the same condition. The bulk reduced density $\rho^{bulk}\sigma^3$ is set to 0.823 to match that obtained in MD simulation. And the mole fraction of AB in bulk x_{AB}^{bulk} is also specified to 0.004 according to the MD simulation. The results are shown in Figure 3.1. It can be seen that the results from iSAFT agree very well with those from MD simulation. Both MD and DFT gives positive stress, meaning the interface is under tension.

3.3 Results and discussion

3.3.1 Stress Profile of an Octane/Water Interface

In iSAFT, octane is modeled as four spherical beads bonded tangentially and the water is modeled as one sphere with four association sites (two electron donors and two accepters). The iSAFT parameters of octane molecule and water molecule are determined by fitting to vapor pressures and saturated liquid densities. And the cross interaction parameter ($k_{ij} = 0.22$) between octane and water is fit to the solubility of water in octane. The value of k_{ij} will be adopted to describe the cross interactions between surfactant tail and head, tail and water, and head and tail. The values of parameters are provided in Table 3.1.

The interfacial tension of an octane/water interface is calculated and compared against experiment (Figure 3.2) and good agreement is achieved.

The stress profile and density profile of an octane/water interface at 298 K and 1 atm are given in Figure 3.4. From the figure, we can see that the largest contribution to the stress is on the water side of the interface. Unlike the octane side that has a negative stress with small magnitude, the stress on the water side is huge and dom-

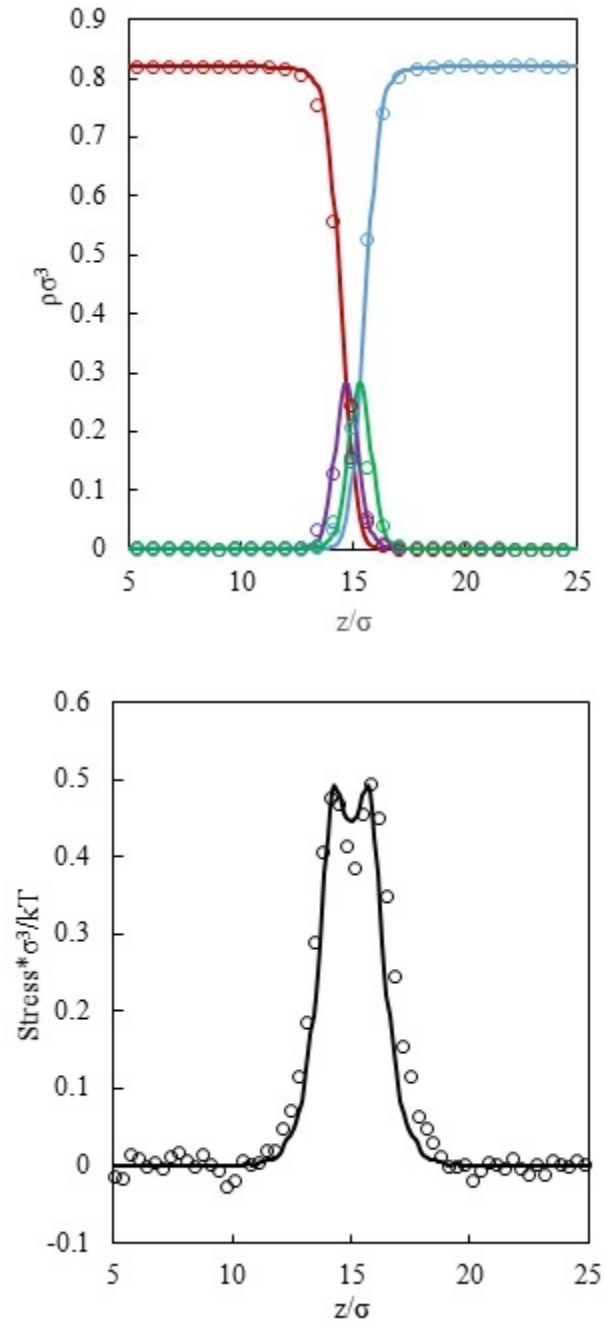


Figure 3.1 : Comparison between iSAFT and MD for an A/B/AB mixture. The upper panel shows the density profile from iSAFT (solid lines) and MD (circles). The lower panel shows the stress profile from iSAFT (solid line) and MD (circles). $\rho^{bulk}\sigma^3 = 0.823$ and $x_{AB}^{bulk} = 0.004$.

Table 3.1 : Summary of Parameters

	m	$\sigma(\text{\AA})$	ε/k_B (K)	ε_{assoc}/k_B	K/σ^3
water	1	3.0	328.6	1747.3	0.004432
octane	4	3.6	294.05		
Head segments	x	3.0	328.6	1747.3	0.004432
Tail segments	y	3.0	294.05		

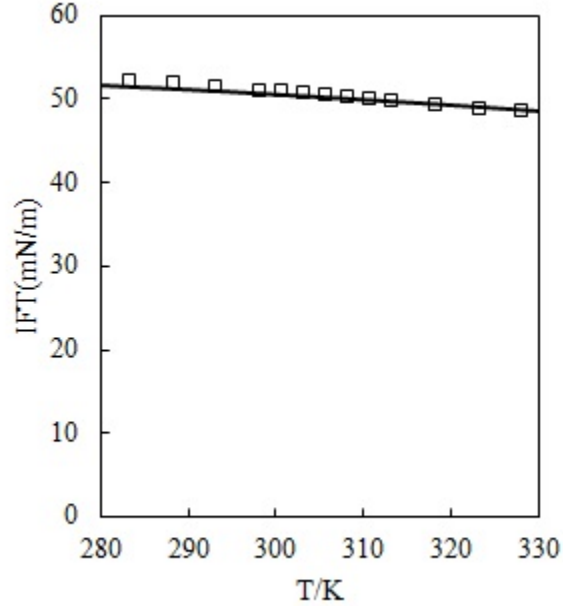


Figure 3.2 : Interfacial tension of an octane/water interface as a function of temperature. Dots are from experiments[6]. Line is from iSAFT.

inates the value of interfacial tension($\gamma = \int stress(z)dz$). This might be one of the reasons why surfactant head group properties dominate the interfacial tension[103]. By definition, a region with positive stress is under tension, and a region with negative stress is under compression tending to expand. So it would be intuitive to think that this flat octane/water interface with this stress profile would be favorable to be concave toward the water phase so that the stress is released. Figure 3.3 gives the stress profiles of the same octane/water interface at different temperatures(298 K, 330 K, 360 K) and 1 atm in real unit. We can see that the magnitude of the stress is huge(around 100 MPa) compared with the bulk pressure (1 atm). This high value of pressure in the inhomogeneous region has been shown by Long et al.[97] from Monte Carlo simulation for fluids under confinement and it can be used to explain the phenomena observed in the inhomogeneous region that will only occur in the bulk phase at extremely high pressure [104, 105, 106, 107, 108, 109, 110]. As temperature is increased, the interfacial tension decreases. The magnitude of the positive stress decreases with the negative stress roughly unchanged. The release of the tension on the water side is perhaps due to the weakening of hydrogen bonding interaction, which is indicated by the increase of the fraction of association sites not bonded X_a from the theory in Figure 3.5.

The stress profile of a water/octane interface can be decoupled to three contributions: the contribution from octane-octane interaction, that from water-water interaction and that from cross interaction between octane and water. Each contribution is shown in Figure 3.6. Several interesting points can be observed. First, the tension on the water side of the interface is mainly due to the interactions between water molecules and lower water density relative to its bulk value while the compression on the octane side of the interface is mainly introduced by the interaction between

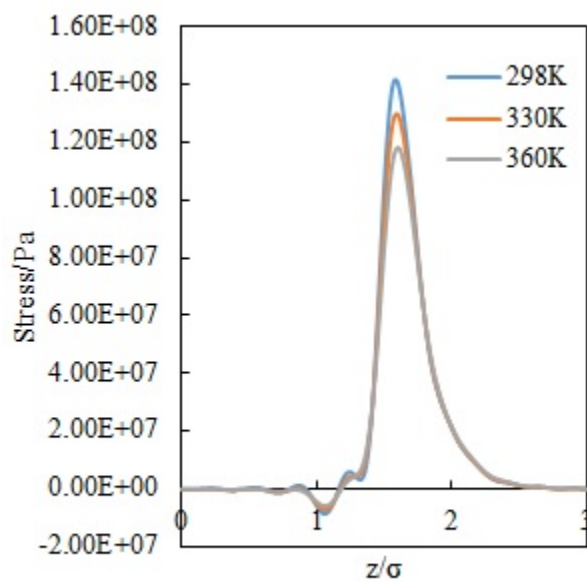


Figure 3.3 : Stress($P_N - P_T$) of octane/water interface from iSAFT at 1 atm and various temperature.

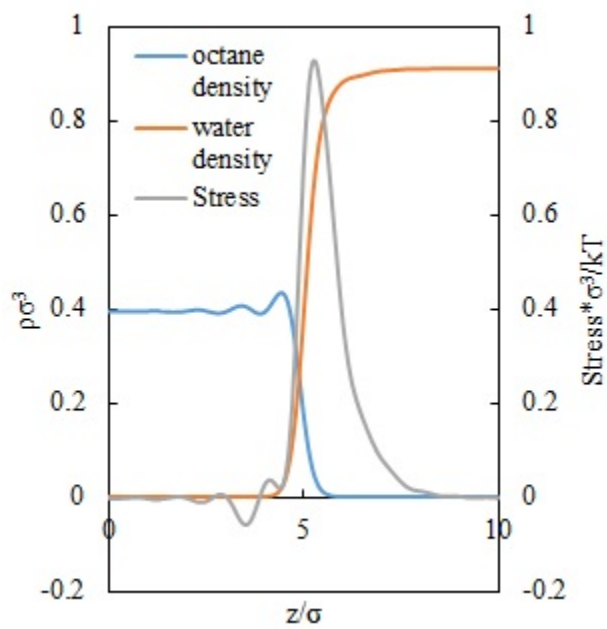


Figure 3.4 : Stress profile(grey) and density profile of a water(red)/octane(blue) interface at 298 K and 1 atm.

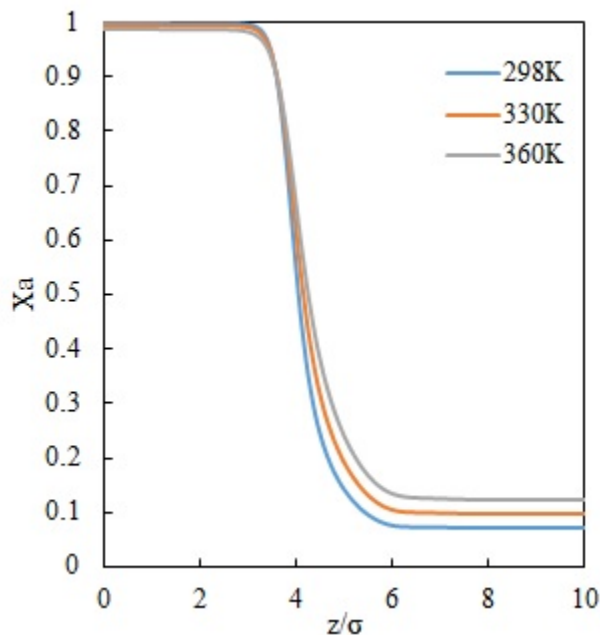


Figure 3.5 : Fraction of association sites not bonded X_a at various temperatures and 1 atm. The increase of X_a implies the weakening of hydrogen bonding between water molecules.

octane molecules and the higher density (i.e. peaks at the interface) relative to its bulk value. Second, the interaction between octane and water molecules has opposite effects on the two sides of the interface: on the octane side the interaction introduces tension that helps to enhance the density of octane while on the water side it introduces repulsion that tends to decrease the density of water. These two effects can be intuitively understood. Due to relatively high water density, water phase behaves like an attractive wall and it attracts the octane molecules to the interfacial region, resulting in an effective tension that tends to bring octane molecules to a denser state. On the other hand, the presence of octane phase disturbs the hydrogen bonding interactions between water molecules and essentially results in an effective repulsion in that region.

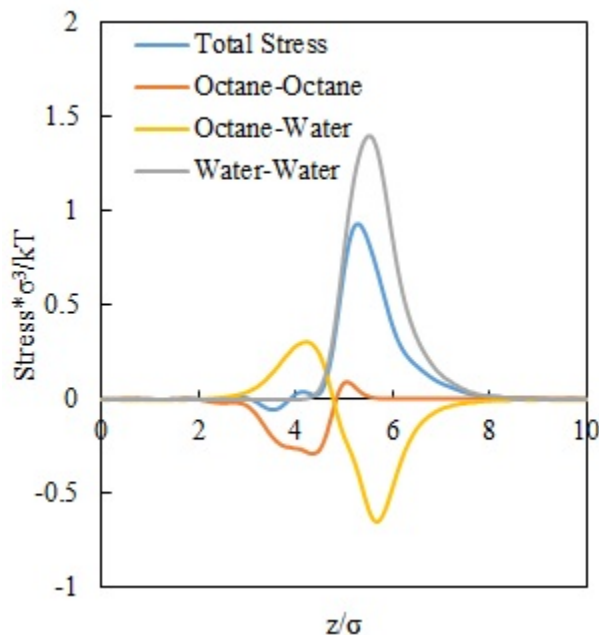


Figure 3.6 : Stress profile of a water/octane interface at 298 K and 1 atm. The total stress profile is decoupled to three contributions: the contribution from octane-octane interaction, that from water-water interaction and that from water-octane interaction.

Aside from temperature, the mechanical property of an oil/water interface can be altered dramatically by the addition of surface active agent (surfactant). A small amount of surfactant is capable of reducing interfacial tension between oil and water by orders of magnitudes. Hereafter, the mechanical property of octane/water interfaces with surfactant molecules and the formation of microemulsions will be studied. Before discussing the results, we need a surfactant model. Here as mentioned in Chapter 2, we extended the Telo da Gama and Gubbins model and explicitly includes the hydrogen bonding interactions between surfactant head and water. Each surfactant head segment carries two independent association sites that can only form hydrogen bonds with water molecules. The values of parameters have already been given in Table 3.1.

3.3.2 Method of Moments

Winsor[111] first clarified the types of microemulsions (Winsor I, Winsor II and Winsor III) in his Winsor R theory. The theory can help qualitatively understand the effects of amphiphiles formulation (surfactant nature, temperature, salinity, and etc) on the types of microemulsions produced. However, the Winsor R theory is not straightforward to implement due to the ambiguous definition of the interfacial layer: this renders calculating cohesive energies between different species difficult. Conceptually, the Winsor R-ratio (R) describes the bending tendency of the flat interfacial layer. If $R > 1$, the interfacial layer tends to bend toward water phase and a water-in-oil microemulsion (Winsor II) is produced. This bending tendency of the interface depends on the mechanical properties of the flat interface or forces exerted on that interface, which can be unveiled from the aforementioned stress profile. Based on this interpretation, a more quantitative Winsor R type of theories (Method of Moments) was developed by Fraaije et al.[22]. This idea is not new. Similar approaches were proposed by Murphy[92] and Bowcott et al. [93]. However, an effective way of calculating stress profile was not available which prevented the theory from further application. Here, we will apply iSAFT to obtain the stress profile and study the formation of microemulsions.

The key equations used in this work for a planar interface are given in Equation 3.1,

$$\begin{aligned}
 M_k &= \int s(z)z^k dz \\
 \gamma &= M_0 \\
 \tau &= -M_1, (\text{when } M_0 = 0)
 \end{aligned}
 \tag{3.1}$$

where M_k is the k th moment of stress profile($s(z)$), γ denotes the interfacial tension,

and τ denotes the surface torque density. What should be noted is that calculating surface torque density requires the interfacial tension to be 0 (which is essentially the case when a microemulsion forms) so that the determination of the position of neutral surface[92] is no longer needed. Hereafter, all the results are obtained at zero tension if not mentioned explicitly. For a planar interface, according to Helfrich[112, 113], the surface torque density is equal to kc_0 , where k represents bending modulus and c_0 is the spontaneous curvature. According to Fraaije et al., the surface torque density is sufficient to determine the optimal condition for the middle-phase microemulsion[22]. The relationship between surface torque density (τ) and Winsor R-ratio is given in Equation 3.2.

$$\begin{aligned}\tau = 0 &\equiv R = 1 \\ \tau < 0 &\equiv R > 1 \\ \tau > 0 &\equiv R < 1\end{aligned}\tag{3.2}$$

For this relationship to hold, the oil phase should be located on the left of the calculation domain and water phase on the right. This condition was not mentioned in the original publication.

It was shown that this method is capable of successfully capturing the dependence of the phase behavior of ternary ionic surfactant/oil/water mixture on salinity. The optimal salinity obtained from the Method of Moments implemented in Dissipative Particle Dynamics is in good agreement with experimental data[22]. Here, we implement this method to show the capability of iSAFT in capturing the physics of surfactant containing solutions and predict the effect of nonionic surfactant formulation on the formation of microemulsions.

3.3.3 Effect of Temperature

Temperature has a strong effect on the phase behavior of ternary nonionic surfactant/oil/water system. At low temperature, surfactant heads are hydrated due to the strong hydrogen bonding interactions between surfactant heads and water molecules. Hence, surfactant molecules tend to maximize their contact with aqueous environment and an oil-in-water microemulsion is favorable ($R < 1$). When temperature is increased, the interaction between water molecules and surfactants are weakened so that the apolar interaction between surfactant and oil dominates. Then, the surfactants tend to optimize their contact with oil molecules and a water-in-oil microemulsion is favored ($R > 1$). At the right temperature in between, the interaction between surfactant and oil is equivalent to that between surfactant and water, and a middle-phase microemulsion is favorable ($R = 1$). In this case, the interactions between the surfactant layer and oil and that between the surfactant layer and water are thought to be balanced. This balanced temperature is usually referred to as phase inversion temperature[114].

To see whether this physics can be captured from iSAFT, the surface torque densities of a series of model nonionic surfactants were calculated based on the Method of Moments. The results are presented in Figure 3.7. From the figure, we can see that the surface torque density decreases as the temperature increases. (As shown in Equation 3.2, $\tau > 0$ is equivalent to $R < 1$, meaning an oil-in-water microemulsion forms, and $\tau < 0$ means a water-in-oil microemulsion forms. $\tau = 0$ suggests a middle-phase microemulsion is produced.) For the case of H5T6 surfactant (red line), an oil-in-water microemulsion forms at 298 K but, at 360 K, a water-in-oil microemulsion is favored, with phase inversion temperature in between. The results also suggest that the phase inversion temperature increases as the hydrophilicity rises (either by increasing head

size or decreasing tail size). These trends from iSAFT agree qualitatively with the experimental observation[115].

3.3.4 Effect of Head/Tail Size

The phase behavior of surfactant/oil/water systems also depends on the structure of surfactant molecules. Based on hydrophilic-lipophilic balance(HLB) analysis[116], surfactants being more hydrophilic have higher solubility in aqueous phase and an oil-in-water microemulsion forms more easily, while more hydrophobic surfactants (although still amphiphilic) tend to be solubilized in the oil phase, resulting in a water-in-oil microemulsion. This experimentally observed trend can also be predicted from our model.

Here, we show the effects of surfactant head and tail sizes on the microemulsion formed at three different temperatures (298 K, 330 K, 360 K) and 1 atm from iSAFT. The effect of head size is illustrated in Figure 3.8 and that of the tail size in Figure 3.9. When surfactant tail size is fixed, increasing the head size enhances the hydrophilicity of the surfactant molecules. As a result, a water-in-oil microemulsion($\tau < 0$ with small head size) can be transformed to an oil-in-water microemulsion($\tau > 0$ with large head size). Similarly, increasing the tail size makes the surfactant less hydrophilic, so that the original oil-in-water microemulsion ($\tau > 0$ with small tail size) becomes a water-in-oil microemulsion($\tau < 0$ with large tail size).

3.3.5 Single-Tail Surfactant vs Double-Tail Surfactant

Compared with the studies on single-chain surfactants, relatively less comprehensive understanding has been made on the effect of branching on surfactants interfacial properties. It was known experimentally that some double-chain surfactants[117,

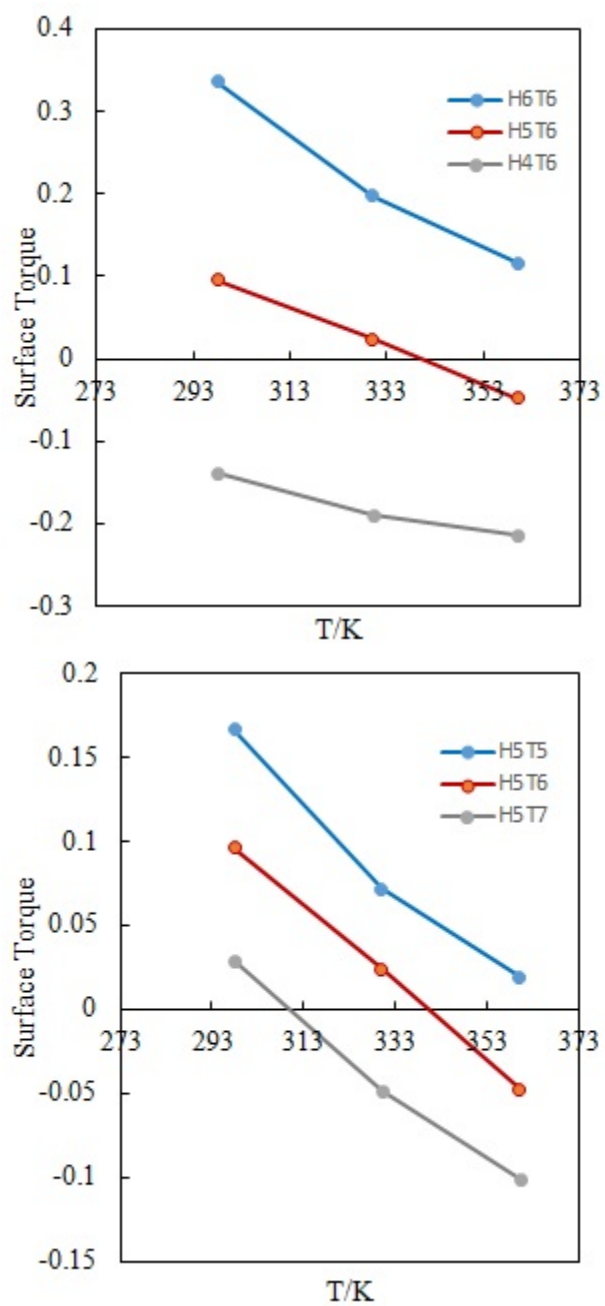


Figure 3.7 : Effect of temperature on surface torque density at zero interfacial tension and 1 atm.

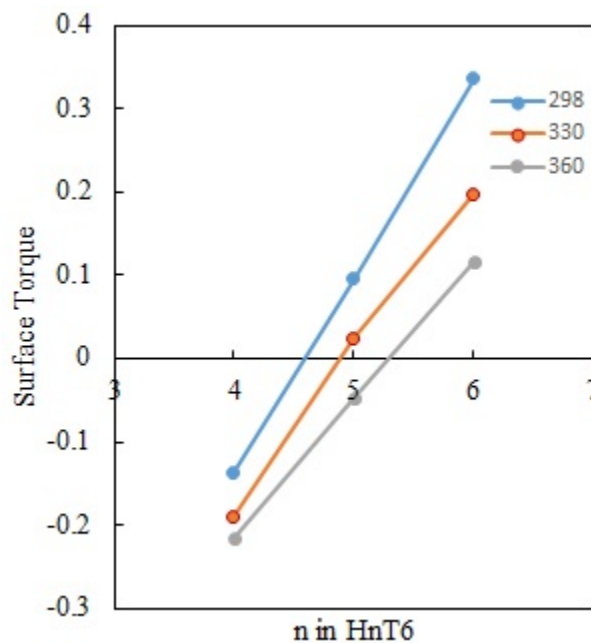


Figure 3.8 : Effect of head size on surface torque density at various temperature, 1 atm and zero interfacial tension. The tail size is fixed to 6 segments.

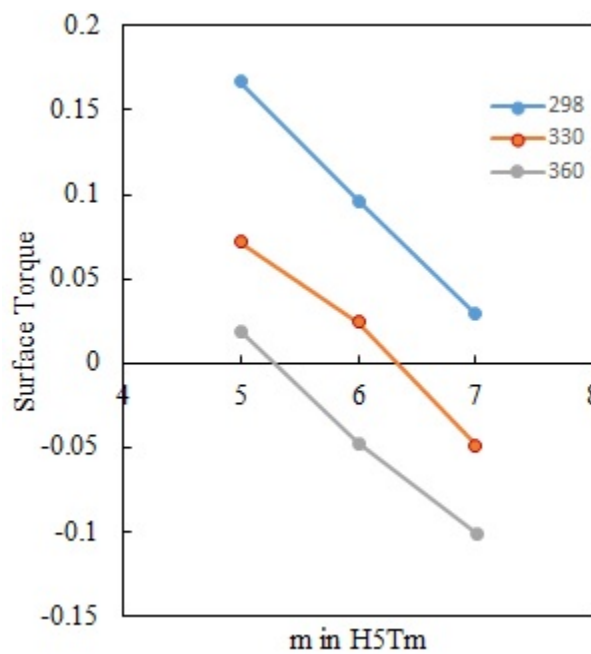


Figure 3.9 : Effect of tail size on surface torque density at various temperature, 1 atm and zero interfacial tension. The head size is fixed to 5 segments.

118, 119] are capable of producing ultra-low interfacial tensions. We also know that interfacial tension is a function of surfactant's ability to reduce the interfacial tension and the density of surfactant molecules present at the interface. It was shown by Emborsky et al.[120] and other researchers[121, 122] using theoretical approaches that double-tail surfactants are less effective in partitioning to oil/water interface(i.e. they need higher bulk surfactant concentration to reach a certain amount of surface excess at the interface) compared with their equivalent single-tail surfactants. On the other hand, double-tail surfactants are more efficient in reducing the interfacial tension for a given surface density of surfactant molecules at the interface compared to single-tail surfactants. Their efficiency in reducing the interfacial tension is attributed to the greater excluded volume effect from the two surfactant tails that reduces the contact between oil and water[120]. Double-tail surfactants are also known to favor the formation of inverse micelles and water-in-oil microemulsions[123]. This can also be rationalized from the theory of packing parameter developed by Israelachvili et al.[23].

Here, we compare the surface torque densities for two model nonionic surfactants - H5T6 and T3H5T3. H5T6 is a single chain surfactant while T3H5T3 is a tri-block copolymer (a double-tail surfactant, other types of double-tail surfactants with branched tails can be readily studied in iSAFT[124]). It is anticipated that T3H5T3 favors the formation of water-in-oil microemulsions more than H5T6 due to its bulky hydrophobic parts. The prediction from iSAFT (Figure 3.10) is consistent with our anticipation. Again, the calculations are performed at 1 atm and zero interfacial tension which is needed for the formation of microemulsions. We can see that over the temperature range, the double-tail T3H5T3 surfactant always produces a water-in-oil microemulsion. On the other hand, the single-tail H5T6 surfactant can produce

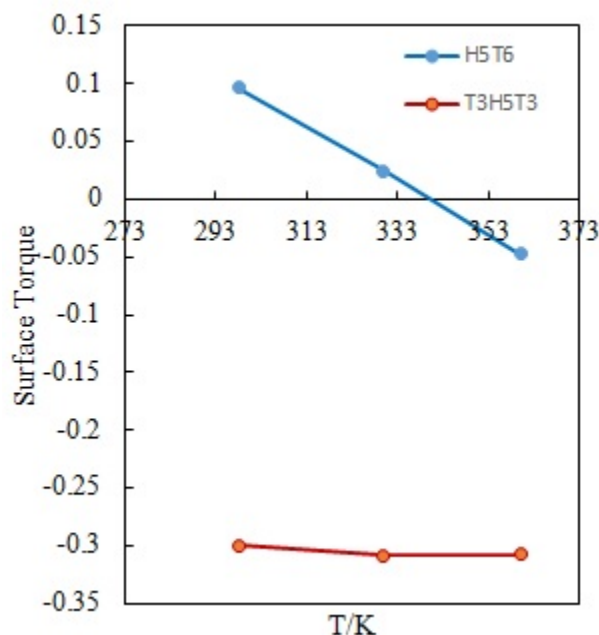


Figure 3.10 : Surface torque densities of single tail H5T6 and double-tail T3H5T3 surfactants at zero interfacial tension and 1 atm.

an oil-in-water microemulsion at low temperature and undergoes phase inversion as temperature raises.

To better understand why this model double-tail surfactant cannot produce an oil-in-water microemulsion at low temperature, we investigated the microscopic mechanical property of the interface or stress profile.

The stress profiles of the tensionless oil/water interfaces with H5T6 and T3H5T3 at 298 K and 1 atm are given in Figure 3.11(a) and Figure 3.11(b), respectively, along with density profiles(Figure 3.11(c) and Figure 3.11(d)). From the density profiles we can see that, as discussed before in the work by Emborsky et al.[120], double-tail surfactant(T3H5T3) is more efficient in reducing the interfacial tension, and lower surfactant surface concentration is needed to produce ultra-low(0) interfacial tension compared with the single-tail surfactant(H5T6) studied in this case. Although the

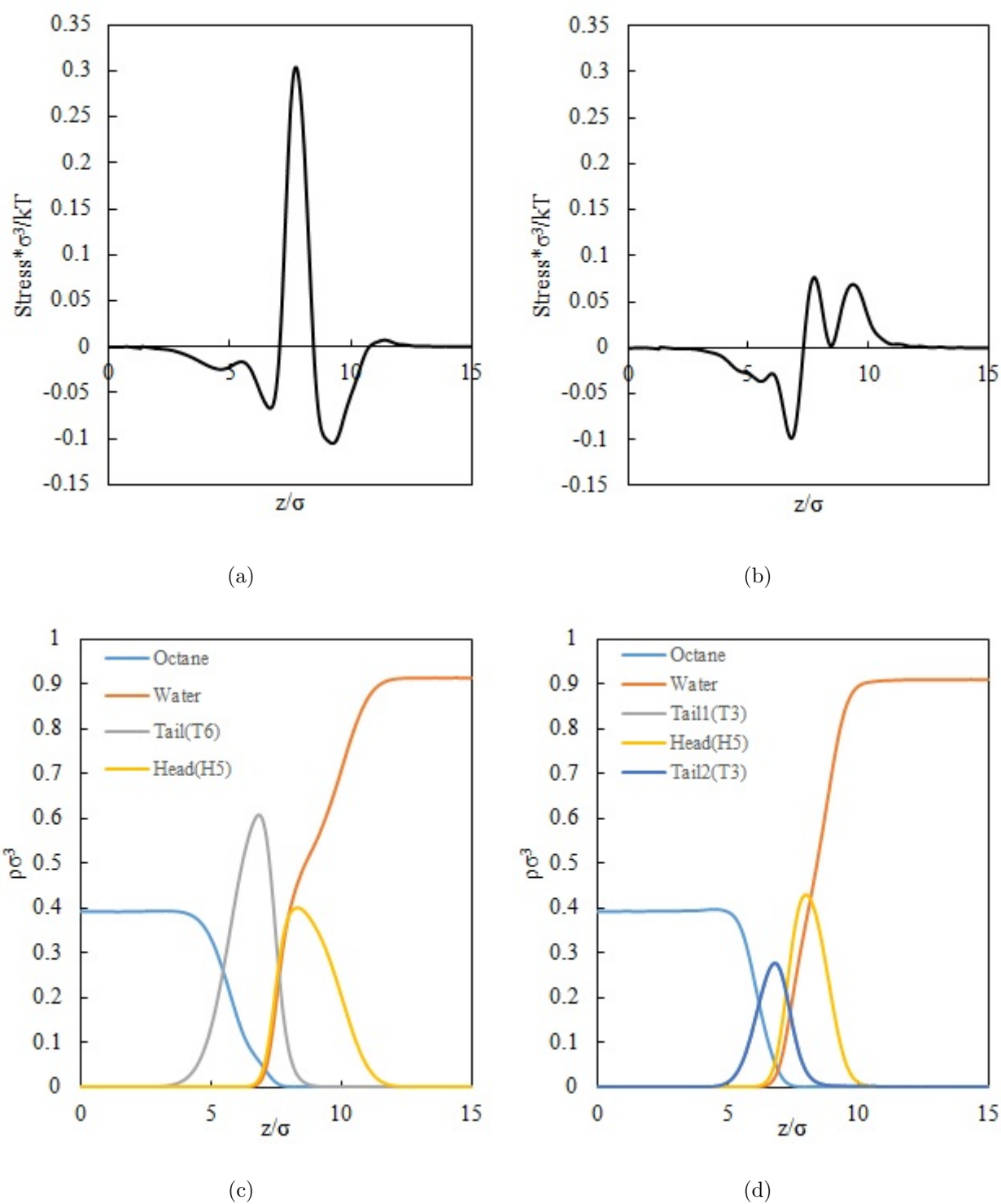


Figure 3.11 : Density profiles(c, d) and stress profiles(a, b) of single-tail surfactants(a, c) and double-tail surfactants(b, d) under zero tension at 298 K and 1 atm. In d, the density profiles of the two tails are overlapping.

interfacial tensions are both equal to zero, the stress profiles or the microscopic mechanical property of the interfaces are very different. The stress profile of the interface with single-tail surfactant(Figure 3.11(a)) has three main peaks: 1 positive peak (under tension) and two negative ones (under compression). The negative stress on the water-rich region which was not observed in the bare octane/water interface is primarily due to the presence of surfactant molecules and the staggering of surfactant heads into water phase. Because of the existence of this compressed region on the water side of the interface, water wants to expand and be the continuous phase, and an oil-in-water microemulsion forms. On the other hand, for the double-tail surfactant(Figure 3.11(b)), the head group cannot stagger far into the water phase due to the constraint imposed by the tails. As a result, no compressed region is present on the water side of the interface. The stress is negative on the oil side(under compression) and positive on the water side(under tension). Hence, the oil side tends to expand and water side tends to shrink. The overall effect is: the interface tends to bend toward the water phase and a water-in-oil microemulsion forms.

Although the excluded volume effect of the tails is important to surfactants efficiency in lower the interfacial tension, the constraining effect of surfactant tails on the configuration of surfactant heads should not be ignored. Due to the presence of double tails, the surfactant heads are more constrained in the water rich region close to the oil phase so that the tension in that region is released more efficiently.

3.4 Conclusion

In this work, the stress profile was obtained from iSAFT density functional theory and compared with molecular dynamics simulation results. Good agreement between theory and MD simulation was observed. The Method of Moments was implemented

in the iSAFT framework to study the effects of surfactant formulation on the formation of microemulsions. The effects of temperature, head size, tail size and surfactant structure(branching) were studied and compared with experimentally observed trends. The theory showed trends consistent with experiments. This implementation of iSAFT and extension of Winsor-R theory using the Method of Moments can be used to facilitate planning of experiments by scanning surfactant formulations and conditions. As a limitation in this work, no micelle formation is considered. However, micelles limit the effectiveness of surfactants in lowering the interfacial tension, which will be the subject of next chapter.

Chapter 4

Effect of Surfactant Architecture on Micelle Formation and Interfacial Tension

4.1 Introduction

Surfactants play important roles in commercial and industrial applications, such as personal care products and enhanced oil recovery (EOR)[54, 125]. EOR has emerged during past decades as a method to recover oil trapped in the reservoir rock after water flooding. As an EOR technique, surfactant flooding involves injection of surfactants into a reservoir to reduce the interfacial tension between the oil and water phases. At lower interfacial tension, crude oil trapped by capillary effects becomes mobile and can more easily be displaced by injected fluids, which results in higher production. Researchers have found that ultralow interfacial tension (below 10^{-3} mN/m) usually appears with a thermodynamically stable middle-phase microemulsion. By optimizing surfactant architecture according to reservoir composition and conditions (temperature, pressure, salinity, etc), the middle-phase microemulsion can be obtained, reaching ultralow interfacial tension and increasing oil recovery efficiency.

Winsor[111] proposed the R-ratio theory to describe the phase behavior of ternary oil/water/surfactant systems. The R-ratio is defined as the ratio of energies of interaction between surfactant layer and oil-rich phase to that between surfactant layer and water-rich phase. For a planar surfactant layer, if the interaction between surfactants and oil phase is more favorable, corresponding to $R > 1$, the surfactant layer

would tend to increase the area of contact with the oil phase and bend toward the water phase. Hence, oil would tend to be the continuous phase and a water-in-oil microemulsion is favored. If the interaction between surfactant layer and water phase is greater, which corresponds to $R < 1$, water tends to become the continuous phase and an oil-in-water microemulsion is favored. Otherwise, if the interaction energies are the same, which corresponds to $R = 1$, a middle-phase microemulsion is favorable. The R-ratio can also be viewed as the tendency of surfactant layer to become convex toward the oil phase over the tendency of surfactant layer to become convex toward the water phase. Following Winsor's pioneering work, Fraaije et al.[22] recently proposed an analogous but more quantified method to predict the formation of a microemulsion, referred to as Method of Moments. In this model, the stress profile across a planar interface is calculated, based on which the surface torque density is examined. The surface torque density can be interpreted as the tendency of surfactant layer to become convex toward oil minus the tendency of surfactant layer to become convex toward water, similar to Winsor R-ratio. Thus, it was shown that an R-ratio equal to 1 is equivalent to surface torque density equal to 0, at which condition a middle-phase microemulsion is favorable. In Fraaije et al.'s work, the stress profile was calculated from Dissipative Particle Dynamics[126]. The stress profile can also be calculated from Molecular Dynamics Simulation[102], or Classical Density Functional Theory[127]. The Method of Moments quantitatively bridges the gap between surfactant architecture and their bulk phase behavior. But a challenge remains in this method: it requires interfacial tension to be 0 and its accuracy depends on the method used to calculate interfacial tension. The ability of surfactant to acquire ultralow interfacial tension is determined by its efficiency at the oil-water interface, which is influenced by the equilibrium among micelles, surfactant monomers in so-

lution and surfactant at the interface. This equilibrium is achieved when surfactant concentration reaches the critical micelle concentration (CMC). To correctly calculate interfacial tensions and apply Method of Moments, a model has to capture this equilibrium, the formation of micelles and the CMC in the first place. However, none of the previous mentioned models has this capability, which contributes to part of our motivations.

Several models have been proposed to describe micelle formation and predict the CMC. Although empirical correlations may be established based on fitting to extensively measured data[128], predictive theoretical models are preferred since they require less to fit while providing greater understanding of the physics behind micelle formation. Two approaches are usually applied to construct models predicting the CMC[129]. One is the phase-separation approach, in which the micelle is assumed to be a bulk homogeneous surfactant rich phase[130]. The CMC is obtained by conducting phase equilibrium calculations. But this assumption is questionable since the distribution of surfactant molecules inside a micelle is not uniform. The other approach is the kinetic or mass-action approach[131], which involves solving the ‘chemical’ equilibrium between surfactant monomers and micelles. Parameters including the stability constants are fit to experimental CMC data. However, although the experimental CMC values may successfully be reproduced, neither molecular-scale structural information of the micelle nor interfacial properties such as interfacial tension is available from these two approaches.

Recently, models based on statistical mechanics such as classical density functional theory (DFT) have been developed to model the meso-scale structure of complex fluids. DFT has shown its strength in modeling inhomogeneous and complex fluids and excellent agreement with molecular simulations and experiments for a variety of

systems, including the behavior of polymer brushes[132, 133, 134, 135, 136], phase behavior and structure of block copolymers[137, 138, 139], interfacial properties of oil/water systems[140, 36], and the impact of surfactant architecture on interfacial properties[120], etc. The theory can be computationally more efficient than molecular simulations since density fields rather than trajectories of individual molecules are calculated, and the method takes advantage of system symmetry. More importantly, due to the limitation of computing resources, molecular simulation cannot model true thermodynamic equilibrium between surfactant monomers and aggregates. Because low surfactant monomer concentration in the bulk would result in large numbers of solvent molecules in the simulation box, simulations cannot be efficiently conducted within reasonable period of time, while DFT does not have this issue. These advantages make DFT a more suitable approach in modeling micelle formation and surfactant phase behavior compared with simulation techniques.

The goal of this work is to demonstrate the feasibility of applying interfacial Statistical Associating Fluid Theory(iSAFT) DFT[78, 67] to predict the CMC and describe micelle/reverse micelle structure for model nonionic surfactants, and to establish the theoretical basis for molecular understanding of the impact of surfactant architecture on surfactant phase behavior. In this work, we apply iSAFT to investigate the effect of surfactant architecture on the CMC, the micellar structure, aggregation number, and interfacial tension. Furthermore, the formation of swollen micelle and reverse swollen micelle are also studied. To our knowledge, this is the first time DFT is applied to model such systems.

4.2 Parameter Estimation

In iSAFT, five physical model parameters, m , σ , ε , ε_{assoc} , and K , are involved. m represents the number of segments in each molecule, σ denotes the hard sphere diameter of a segment, ε represents the depth of Lennard-Jones interaction energy, ε_{assoc} is the association energy and K denotes the bonding volume. The optimum set of these five parameters are regressed such that properties such as vapor pressures and saturated liquid densities calculated from the theory agree with experimental data. In this work, the systems involve water, oil(octane) and surfactant molecules. As mentioned above, water is modeled as one spherical segment with four association sites: two electron donors and two acceptors. Octane is modeled as a chain that consists of 4 tangentially bonded spherical segments, each segment representing two CH₂ group. Surfactants, being amphiphilic, are modeled as a chain built of oil-like segments and water-like segments[120, 66, 141].

The comparison of vapor pressures and saturated liquid densities between results from iSAFT and experiments are shown in Figure 4.1. For the segments in the head of surfactants, the water diameter and Lennard-Jones energy are used. Instead of four association sites, each head segment carries two association sites (both are electron donor sites). This model surfactant shares some similarity with the poly (ethylene oxide) alkyl ether (CxEy) surfactants. On one hand, the model surfactant is nonionic and has both hydrophobic and hydrophilic segments. On the other hand, each hydrophilic segment can form hydrogen bond(s) with water, similar to the ethoxy(EO) group in CxEy surfactant. So in the Results and Discussion section, we will compare with experimental data of some CxEy surfactants to qualitatively validate our approach. The schematics of the model water, octane, and surfactant molecules are shown in Figure 2.2. The values of parameters used are given in Table 4.1. Binary

Table 4.1 : Summary of Parameters

	m	$\sigma(\text{\AA})$	ε/k_B (K)	ε_{assoc}/k_B	K/σ^3
water	1	3.0	328.6	1747.3	0.004432
octane	4	3.6	294.05		
Head segments	x	3.0	328.6	1747.3	0.004432
Tail segments	y	3.0	294.05		

interaction parameter between water and octane is fitted to solubility of octane in water, and the final value is 0.07. For the cross interaction between water and head segments and between octane and tail segments, the binary interaction parameter is 0. For the cross interaction between water and tail segments, and between head segments and octane or tail segments, ε/k_B is set to 100 K, mimicking unfavorable interaction between unlike components.

A computational grid is defined with spacing of 0.05σ between density points. To simplify the calculation, we assume the system is spherically symmetric and the origin of the coordinate system is at the center of the micelle. In other words, the density profile or structure of the micelle is only a function of radial distance r from the center of micelle. The aggregation number (number of surfactant molecules in one micelle) is obtained by integrating the equilibrated density profile over the space. For calculations of interfacial tension isotherm, the interface is assumed planar. The interfacial tension γ is the excess grand potential, $\gamma = \frac{\Omega - \Omega_{bulk}}{A}$, where Ω_{bulk} and Ω are the grand potentials of the bulk phase and of the system respectively, which are obtained from Eq. (2.17).

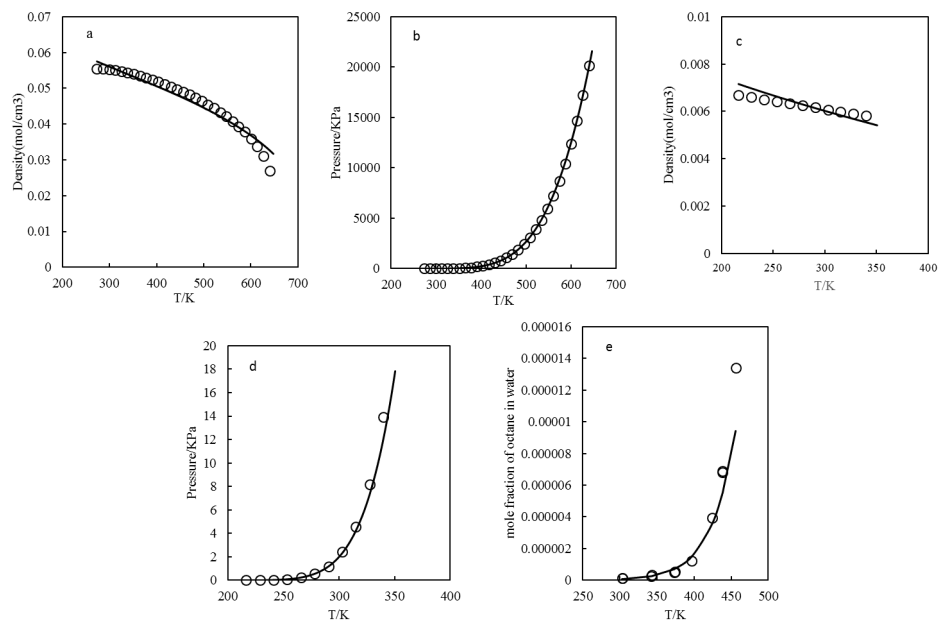


Figure 4.1 : Liquid density(a, c) and saturated vapor pressure(b, d) of water and octane respectively from theory(line) and experiments(circle). Solubility of octane in water(e) from theory(line) and experiments[7](circle).

4.3 Results and Discussion

4.3.1 Water/surfactant binary mixtures

a. Determination of the CMC

In surfactant systems, the CMC is defined as the minimum concentration of surfactants necessary to form stable micelles. By assuming that the micelle formed is spherically symmetric[142], the CMC can be determined by iSAFT DFT written in spherical form. To obtain the value of the CMC, we compare the grand potentials of the systems with and without the formation of a micelle at the same bulk surfactant concentration. Since volume, temperature, and bulk chemical potentials are fixed, the system with lower grand potential is the stable one. Hence, the CMC can be regarded as the bulk surfactant concentration when the grand potential of system

with a micelle is the same as in the system without a micelle.

In Figure 4.2, we show the grand potential as a function of bulk surfactant mole fraction for H_5T_4 surfactant (5 head segments and 4 tail segments). We can observe that at low surfactant concentration, the system with a micelle in the center has greater grand potential than that without a micelle, which means the micellar system is not stable and the CMC has not been reached. As we increase the concentration of surfactants in bulk, the grand potential of the micellar system decreases and crosses that without a micelle. At the cross, the micellar phase is as stable as the non-micellar phase; this is the CMC. If we further increase the bulk concentration of surfactants, the grand potential of micellar phase further decreases, which means the micellar phase is energetically more favorable and more micelles will form until the bulk surfactant concentration is reduced to the CMC. Note that only one micelle is considered in our calculation and hence the interaction between micelles are neglected.

b. Micelle structure

Figure 4.3 shows the reduced number density profile of surfactant and water as a function of radial distance r from the center of a micelle. As we can see, the structure of the micelle formed by H_5T_4 surfactant is similar to the conventional picture of a micelle structure. In the center of the micelle, hydrophobic tail segments aggregate to expel hydrophilic segments and form a hydrophobic core. The iSAFT DFT predicts a depletion of surfactant tail at the center of micelle, which is also observed in molecular simulations[8, 143]. The average density of hydrophobic segments (T4) in this inner core is approximately equal to the reduced bulk density ($\rho\sigma^3 = 0.6815$) of an alkane built of four tail segments at the same temperature. The hydrophilic head segments are exposed to water molecules and fully hydrated. The hydration of the head groups effectively expands the head group helping to stabilize the micelle structure. We can

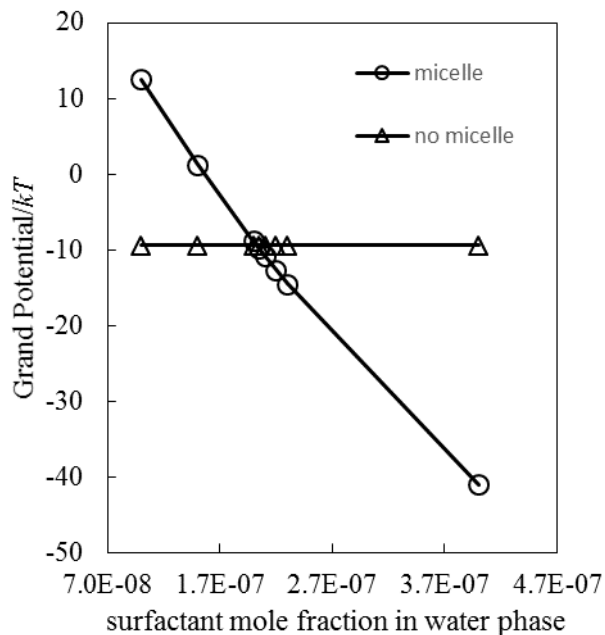


Figure 4.2 : Comparison of Grand Potential for the CMC determination.

also observe that the radius of the micelle is approximately 8σ which corresponds to 24 Å; this value is consistent with experimentally measured values ranging from 22 to 24 Å [144, 145]. The water density is essentially zero inside the hydrophobic core of the micelle, and increases monotonically to its bulk value. Since the model surfactant shares some similarity with poly (ethylene oxide) alkyl ether (CxEy) surfactant, it is reasonable to compare the micellar structure predicted from our model with that from molecular dynamics simulation [8] of CxEy, which is reprinted in the bottom panel in Figure 4.3. Instead of density profile, only center-of-mass based radial distribution function is available. The radial distribution function is defined as the density profile normalized by a constant - average density in the simulation box. It can be seen that the micelle from iSAFT calculation is similar to that from MD simulation. What has to be pointed out is, in MD simulation, the number of surfactants in a micelle is

artificially set, which may affect the structure of the micelle[8].

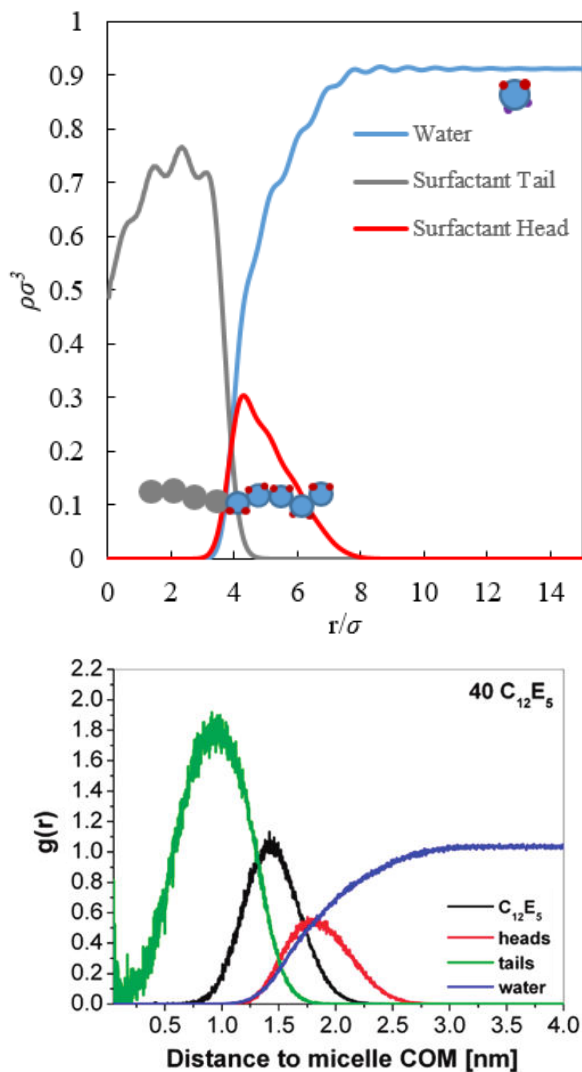


Figure 4.3 : The top panel shows the structure of micelle formed by H_5T_4 surfactants from DFT calculation. The bottom panel is the radial distribution functions $g(r)$ for micelle formed by 40 $C_{12}E_5$ surfactant molecules. Reprinted with permission from ref [8]. Copyright 2011 American Chemical Society.

c. Effect of surfactant architecture on the CMC

The effect of head size on the CMC is obtained. The size of tail is fixed to 4 tail segments, and the head size ranges from 4 to 7 segments. Experimentally, the

CMC increases monotonically as the head size rises[146], same as what we observe from iSAFT (Figure 4.4a). When the head size increases, the hydrophilicity of surfactant goes up that increases the solubility of surfactant in water. Thus, a higher concentration of surfactant molecules is necessary to form aggregates. The larger than expected change in the CMC with the number of head segments could indicate that the hydrogen bonding interaction is too strong and needs to be revised to show quantitative agreement.

For the effect of tail size on the CMC, the head is fixed to 6 segments and the tail size is changed consecutively from 3 to 6 segments. The result is shown in Figure 4.4b. When the size of tail increases, the CMC decreases. This is in qualitative agreement with experimental observation[147]. The model shows larger dependence of the CMC on tail length than seen experimentally. This might be due to the lack of attraction between water and tail groups in the model.

Experimental results show that the CMC depends much more strongly on the size of tail than that of head. The experimental results[146, 147] showing the CMC as a function of the size of tail and head are summarized in Table 2. We can observe that the CMC remains in the same order of magnitude when the head size is altered from four ethoxy groups to eight ethoxy groups, but it changes orders of magnitude when the tail size is increased from 10 alkyl groups to 14 alkyl groups. This experimental trend can be captured qualitatively by iSAFT. From iSAFT, the CMC rises roughly by 4 times when the head size is increased by one ethoxy group, but it decreases roughly by 40 times when the tail size is increased by one CH_2 group (one tail segment represents 2 CH_2 groups). Hence, the CMC depends much more strongly on the size of surfactant tail, which is consistent with experimental observation.

d.Effect of surfactant structure on aggregation number

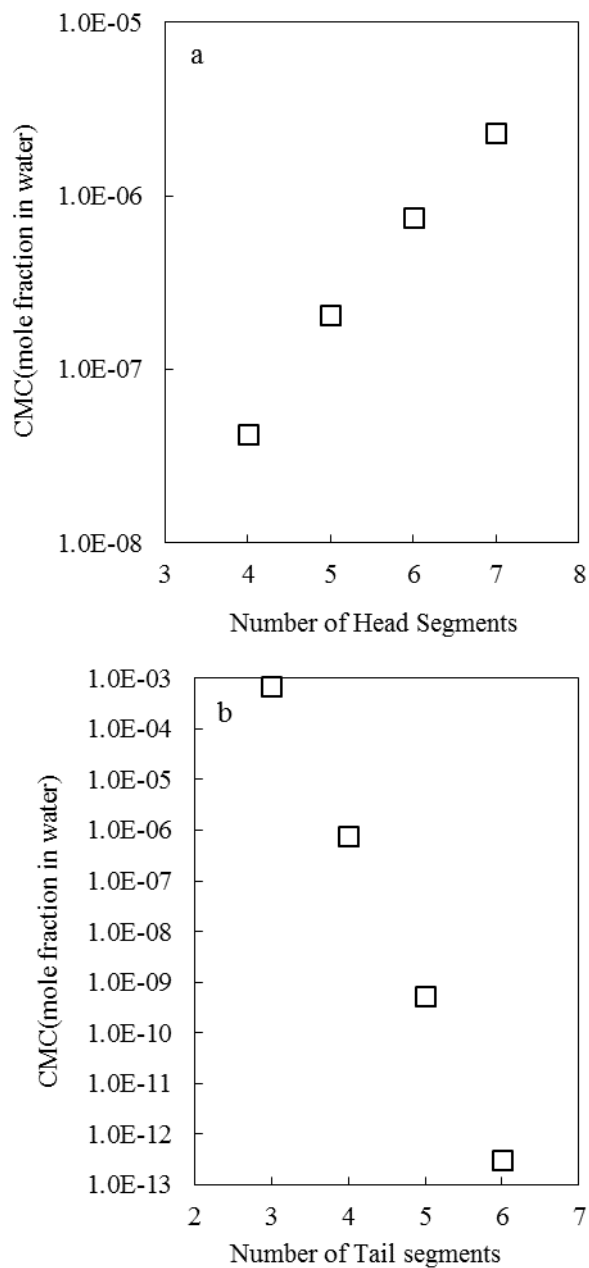


Figure 4.4 : Effect of surfactant architecture on critical micelle concentration. (a) The effect of head size on the critical micelle concentration. All surfactants have 4 tail segments. (b) The effect of tail size on the critical micelle concentration. All surfactants have 6 head segments.

Table 4.2 : Effect of head size and tail size on the CMC from experiment

From ref. [146]	$C_{12}E_4$	$C_{12}E_6$	$C_{12}E_8$
CMC(mole/cm ³) at 30°C	$5.3 * 10^{-8}$	$6.8 * 10^{-8}$	$7.6 * 10^{-8}$
From ref. [147]	$C_{10}E_8$	$C_{12}E_8$	$C_{14}E_8$
CMC(mole/liter) at 30°C	$9.3 * 10^{-4}$	$6.9 * 10^{-5}$	$8.0 * 10^{-6}$

Another physical quantity associated with surfactant systems is the aggregation number. It describes the number of surfactant molecules present in a micelle. This quantity is relatively hard to measure experimentally, involving the use of static light scattering[148], fluorescence quenching methods[149], etc. And the aggregation number measured experimentally is the mean aggregation number but the micelles are not truly monodisperse; there is continual interchange between molecules in the bulk phase and the micelles. In iSAFT, the mean aggregation number of a micelle can be calculated from the density profile, and the results are shown in Figure 4.5. From the figure, we can see that the aggregation number is in the range of 30 – 70; this is consistent with experimental values in the range of ionic and nonionic surfactant molecules[149]. It is observed that when the size of tail increases, the number of surfactant molecules present in the micelle also rises. But when the size of head increases, the aggregation number decreases. In other words, when the hydrophilicity of surfactant increases (either by decreasing the tail size or increasing the head size), the aggregation number would decrease. This observation can be explained from the point of view of surfactant packing in the micelle[150]. The conical shape of the hydrated surfactant determines the size of the micelle. Larger tail or smaller head would result in favorable shape contributing to greater aggregation number.

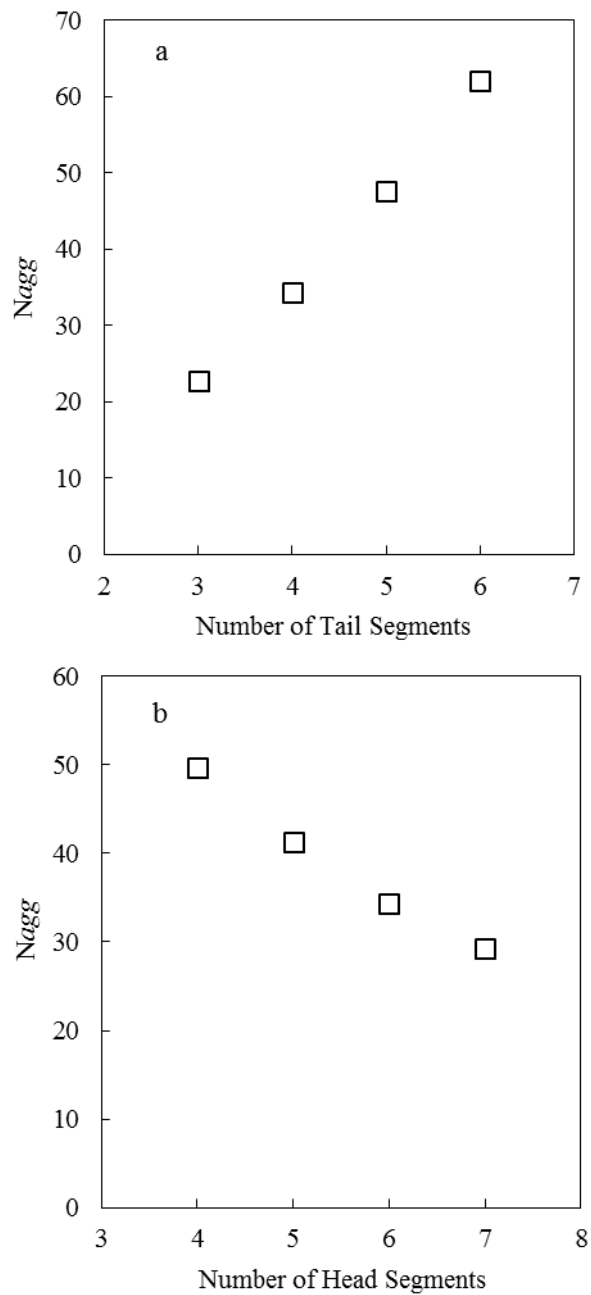


Figure 4.5 : Effect of surfactant structure on aggregation number. (a) The effect of tail size on the aggregation number. All surfactants have 6 head segments. (b) The effect of head size on the aggregation number. All surfactants have 4 tail segments.

e. Effect of surfactant structure on interfacial tension

Due to its amphiphilic nature, surfactant molecules spontaneously partition to the interface and lower the interfacial tension. This is why surfactants find great application in the field of enhanced oil recovery, personal care products, etc[54, 125]. For these applications, it is helpful to have some insights into the effect of surfactant structure on interfacial or surface tension. Previous work with iSAFT[120] did not consider micelle formation and specific association sites. In this work, we take both micellization and association into account, and obtain the interfacial tension isotherm for each specific surfactant.

Here we investigate the binary mixtures consisting of water and surfactant. The surfactants of interest are H_4T_4 , H_5T_4 , H_6T_4 , H_6T_5 , and H_6T_6 . The CMCs were obtained by conducting iSAFT calculations in spherical coordinates at constant temperature (298 K) and pressure (1 bar). The interfacial tensions γ are obtained from iSAFT by calculating the vapor-liquid interfacial profile of a planar interface at constant temperature and over a range of surfactant concentrations with $\gamma = \frac{\Omega - \Omega_{bulk}}{A}$. Here, the assumptions we made are: 1) the surface is planar and symmetric in the $x - y$ plane; 2) the CMCs are not changed when the pressure is changed from 1 bar to vapor/liquid coexistence condition at 298 K since such a small change in pressure has little effect on liquid phase properties.

The iSAFT results, shown in Figure 4.6, are in very good qualitative agreement with experimental results given by Lin et al.[9] and Zhmud et al.[10], which are reprinted in Figure 4.7. Some observations can be made. The interfacial tension is constant for surfactant concentrations above the CMC since additional surfactant partitions to micelles instead of the vapor-liquid interface. We also observe that a surfactant with smaller head or larger tail is more efficient in lowering the interfacial

tension when the concentration of surfactant is below its CMC. Thus a more hydrophobic or less hydrophilic surfactant partitions more readily to the interface and has a lower CMC. Traube's rule[151] can be observed in the second plot, where each increase in surfactant carbon number shifts the interfacial tension curve by decreasing surfactant concentration a constant factor. A surfactant with a smaller head can reach lower interfacial tensions at concentrations above the CMC, which is in qualitative agreement with experiment[119]. Interestingly, the interfacial tension above the CMC is independent of tail length. So the effectiveness of a surfactant in lowering the interfacial tension is more affected by the head of the surfactant.

4.3.2 Water/octane/surfactant ternary mixtures

a. Critical micelle concentration and swollen micelle

The results of water/surfactant binary mixtures were discussed, but what will happen to the micelles when we introduce oil into the system? iSAFT predicts the tendency for oil to be solubilized in the center of a micelle, a swollen micelle.

The CMC for a ternary mixture is determined similar to that for a binary mixture. A series of flash calculations are done at 25 °C and 1 bar with different concentrations of surfactant in the aqueous phase. The CMC is determined based on the grand potential of the system with or without micelle formed. The structure of a swollen micelle is shown in Figure 4.8. It is observed that octane molecules accumulate in the center of the micelle and surfactant helps to decrease the contact between octane and water, hence lowering the free energy of the system.

The CMCs of octane/water/surfactant ternary mixtures are given in Figure 4.9. The CMCs follow the same trend as those of water/surfactant binary mixtures. The presence of oil slightly decreases the CMC values because octane helps stabilize the

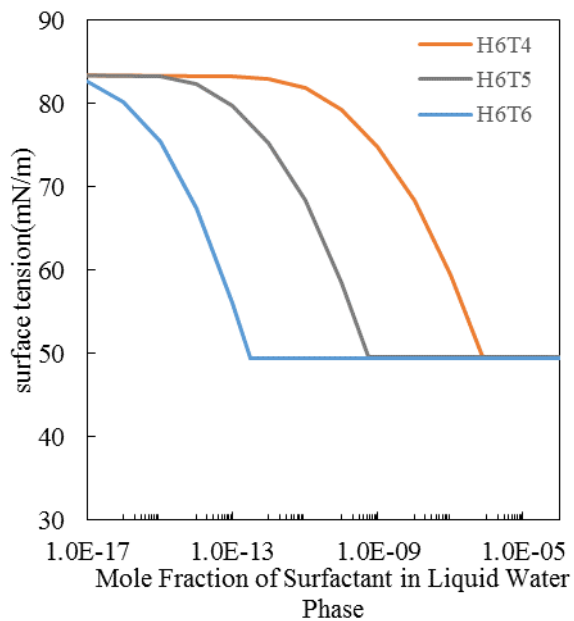
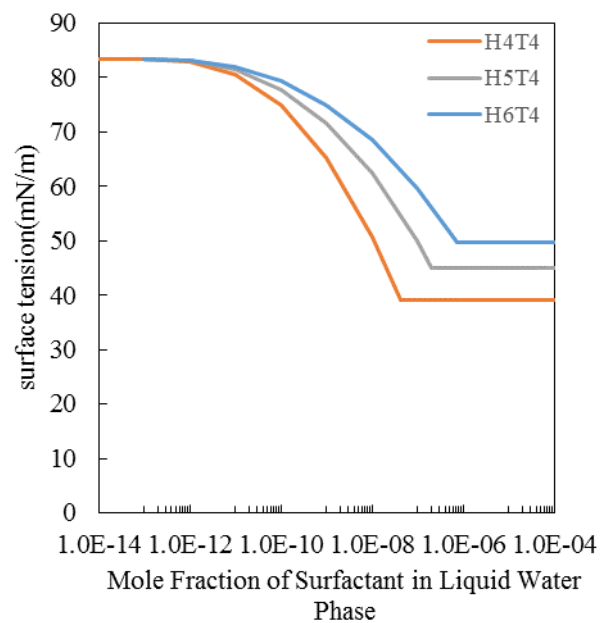


Figure 4.6 : Surface tension as a function of surfactant concentration from iSAFT.

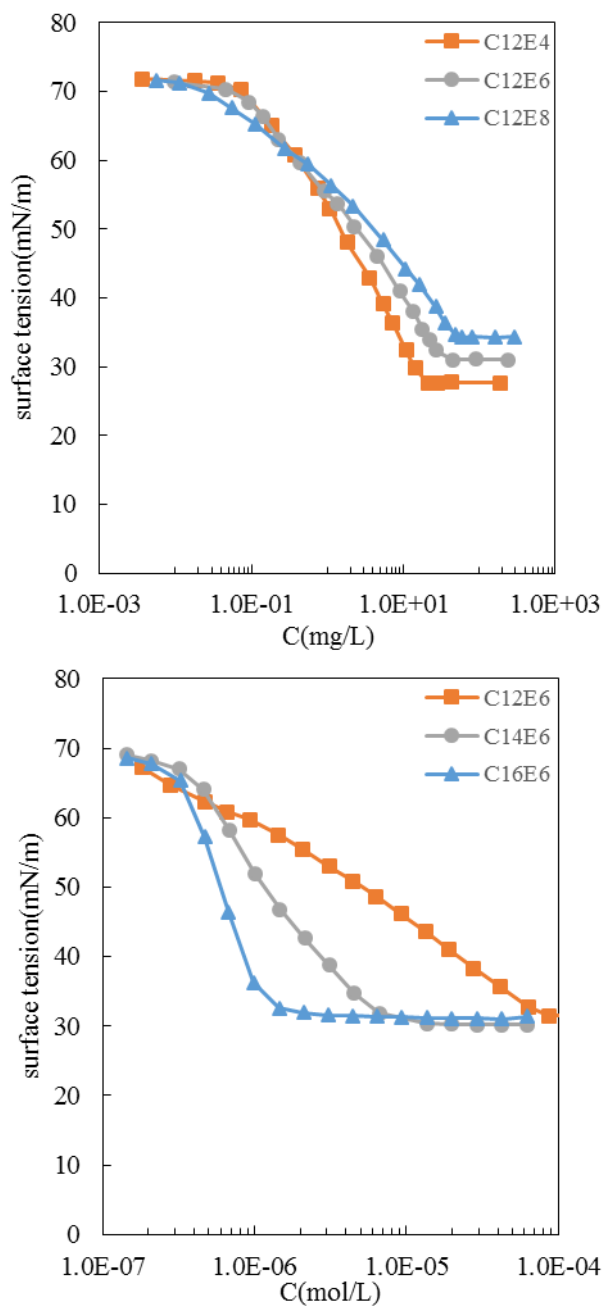


Figure 4.7 : Surface tension isotherm. The top panel reprinted with permission from ref [9]. Copyright 1999 American Chemical Society. The bottom panel is reprinted with permission from ref [10]. Copyright 2000 American Chemical Society.

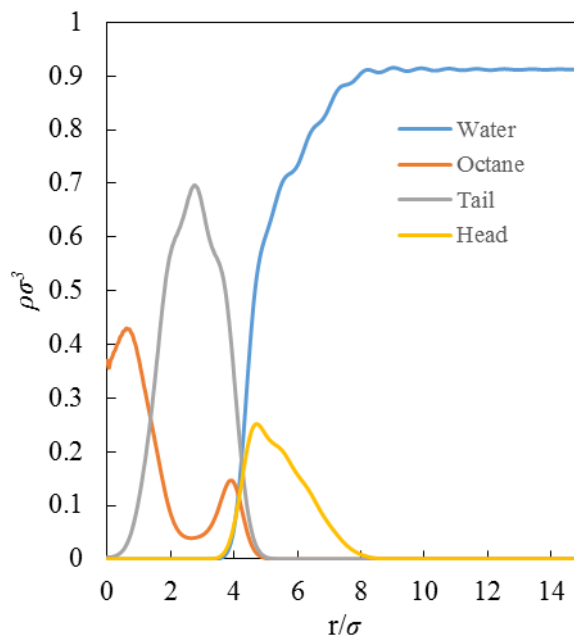


Figure 4.8 : Structure of swollen micelle formed by H5T4/octane/water at 25°C and 1bar .

micelle [119] in the same way as increasing the surfactant tail length reduces the CMC.

b. Reverse swollen micelle

The shape of surfactant molecules determines the structure of surfactant aggregates. When a surfactant molecule carries a large head and small tail, its conical shape would favor the formation of micelle in water. However, if the molecule carries a large tail and small head, the formation of micelle in water would not be that favorable since it is difficult for the molecules to fit. Instead of forming micelles in water, formation of reverse micelles in oil may be more favorable. With this simple idea, researchers[150, 152] proposed the surfactant packing parameter to describe the favorable types of micelle to be formed by different surfactants.

By employing the iSAFT potential parameters listed in Table 4.1, reverse swollen

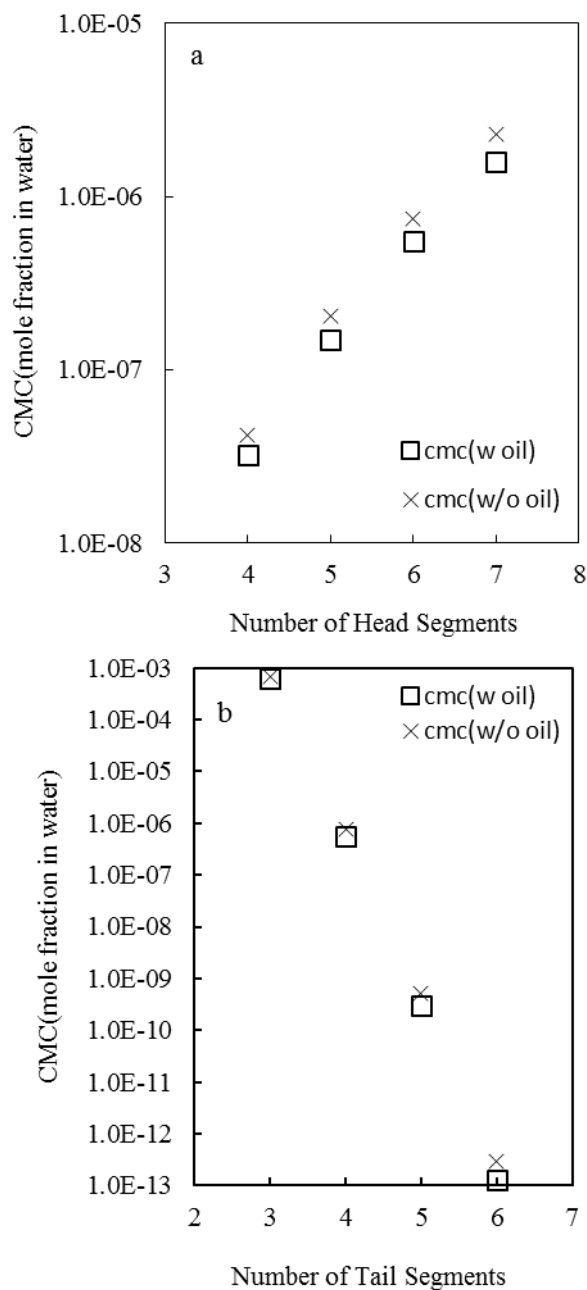


Figure 4.9 : Comparison of the CMC values of surfactant/water systems and surfactant/octane/water systems. (a) The effect of head size on the critical micelle concentration. All surfactants have 4 tail segments. Squares are CMCs with oil present and crosses are CMCs without oil. (b) The effect of tail size on the critical micelle concentration. All surfactants have 6 head segments. Squares are CMCs with oil present and crosses are CMCs without oil.

Table 4.3 : iSAFT parameters for surfactant that forms reverse micelle

	m	$\sigma(\text{\AA})$	ε/k_B (K)	ε_{assoc}/k_B	K/σ^3
Head segments	x	3.0	328.6	1247.3	0.004432
Tail segments	y	3.6	294.05		

micelle cannot be obtained since the shape of surfactant molecule described by those parameters does not favor the reverse micelle formation. The shape of surfactant molecule may be altered by changing conditions such as temperature[152], but the study of temperature effect is beyond the scope of this paper and will be considered in the following papers. Instead of altering conditions, we simply choose values of parameters more favorable to form a reverse micelle. The set of parameters are given in Table 4.3.

From the table, we can see that the diameter of tail segments is increased and the association energy between surfactant head and water is decreased. As a result, the surfactant molecules have a larger tail and smaller head that favors the formation of reverse micelle. Following the same procedure described above, the calculated reverse swollen micelle structure is shown in Figure 4.10. When the system free energy is minimized, it is predicted that water molecules accumulate in the center of the reverse micelle. By altering the structure of surfactant, the structure of a micelle or reverse micelle can be optimized for various applications.

4.4 Conclusion

In this work, iSAFT classical density functional theory is extended to study the effects of surfactant architecture on critical micelle concentration, aggregation number,

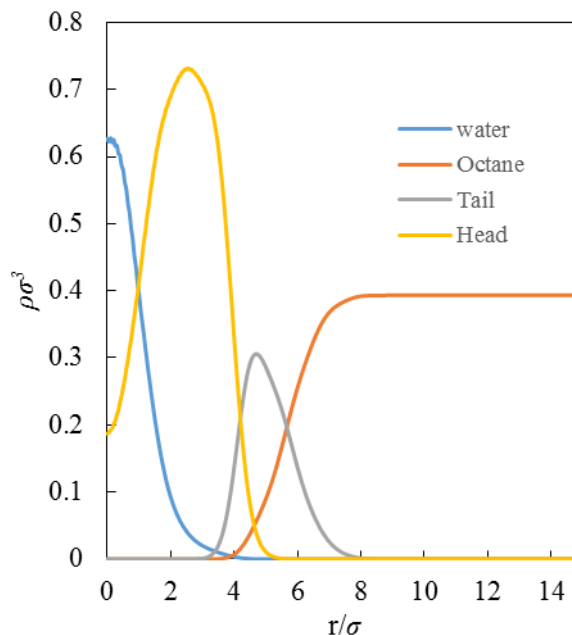


Figure 4.10 : Structure of reverse micelle formed by H5T4/water/octane using the parameters listed in Table 4.3.

and interfacial tension. The model has been shown to describe micelle formation and interfacial properties of surfactants in qualitative agreement with experimental results. Additionally, the formation of swollen micelle and reverse swollen micelle are also described by this model and the phase transition from oil-in-water emulsion to water-in-oil emulsion can be captured successfully. To our knowledge, this is the first time classical density functional theory, particularly with explicit hydration of the head group, has been applied to such systems. In the future, investigations on effects of external conditions such as temperature and pressure on the structure of the micelle and formation of microemulsion will be made. The ultimate goal is to apply iSAFT in the molecular design of surfactant formations for enhanced oil recovery and other applications.

Chapter 5

Simulation Studies on the Role of Lauryl Betaine in Modulating the Stability of AOS Surfactant-Stabilized Foams

5.1 Introduction

Gases such as CO₂, N₂, air, and hydrocarbon gases (mainly methane) are typically injected into oil reservoirs to displace oil to enhance its recovery [153, 154]. However, since the gas phase has low density and low viscosity relative to the oil that it intends to displace, the gas phase can finger through or break through to the top of the reservoir resulting in poor sweep efficiency. Foams are used to counteract this problem.

A foam is a colloidal system consisting of a dispersed gas phase and a continuous liquid phase, which is thermodynamically unstable relative to the parent liquid and gas phases. By virtue of having a higher viscosity, this two phase system offers better mobility control in gas injection or gas flooding [54]. Thus by applying foam, progression of injected media (gas) in reservoirs can be controlled, leading to the elimination of gas breakthrough and the increase in sweep efficiency [155], including of oil from low permeability regions [60].

The stability of foam is important to its application in enhanced oil recovery. Oils, especially the lighter components, can weaken foam. The stability of the foam in the presence of emulsified oil depends on the stability of the asymmetric oil/water/gas pseudo-emulsion film [156, 157, 158]. If the pseudo-emulsion film — a water film

separating the gas phase and the oil drop — is stable, the oil drop cannot penetrate the gas/water interface thereby ensuring the integrity of the film. (In this instance, the disjoining pressure between the gas/water and oil/water interfaces exceeds the capillary pressure due to the curvature of the air/water and oil/water interfaces[159, 154].) However, if the pseudo-emulsion film is unstable, oil enters the gas/water interface weakening foam stability.

Surfactants can help stabilize foams. It has been found that certain surfactants can generate stronger foam than others. Alpha olefin sulfonate (AOS 14-16) is commonly recognized as a good foamer, where the number (14 to 16) indicates the number of carbon atoms in the surfactant tail moiety (this nomenclature will be carried hereafter). In contrast, the NI blend (4:1 blend of Neodol 67-7PO sulfate and internal olefin sulfonate (IOS 15-18)) does not generate a strong foam. However, mixing lauryl betaine (LB) with the NI blend can generate foam that is even more stable than the one generated by AOS itself [160]. Thus lauryl betaine, a foam booster [161], can help stabilize foam even in the presence of oil[160]. It has been speculated that the zwitterionic lauryl betaine helps screen the charge carried by the ionic surfactant at the interface inducing closer packing of surfactants. The closer packing is thought to lead to a higher charge density and hence a greater electrostatic repulsion between the interfaces comprising the pseudo-emulsion film. The enhanced electrostatic repulsion is expected to increase the disjoining pressure between the two interfaces preventing film coalescence[162]. The close packing surfactant monolayer has also been shown to have higher surface shear viscosity, which slows down the drainage of liquid from the film[163]. However, a clear molecular scale analysis of the foam enhancement by LB is as yet unavailable. But an understanding of the molecular basis of the synergistic action of surfactant blends has the potential to lead to rationally designed

surfactant blends for use in foam enhanced oil recovery. Our effort is motivated by this perspective.

The oil/water interface is a building block of the pseudo-emulsion film. Although direct simulation of the rupture process of the pseudo-emulsion film seems to be straightforward to perform, it would be too computationally expensive in current stage considering the thickness of the film and the time scale(nanosecond) simulated. Hence to better understand the role of the zwitterionic LB in boosting foam we seek molecular scale insights into the synergistic behavior of AOS 14-16 and LB in modulating the behavior of octane/water interface, where octane serves as our model hydrocarbon phase. We use molecular dynamics simulations to investigate the behavior of various mixtures of AOS and LB. We find that for some compositions of LB, the tighter packing of surfactants is indeed encouraged, as has been suggested on the basis of experiments. We elucidate the molecular basis of this tighter packing and its consequence for the enhancement in the surface dilatational modulus of the octane/water interface, a key measure of film stability.

The rest of this chapter is organized as follows. In the following section we present the molecular dynamics methods we used. In Section III, we present the results and discussion, and in Section IV we present our conclusions.

5.2 Molecular dynamics simulations

The structures of lauryl betaine (LB), alpha olefin sulfonate 14 (AOS-14), and octane were prepared using the *xleap* module of AMBER[44]. The molecular structures of LB and AOS-14 are shown in Fig. 5.1 with the partial charges of head group atoms labeled. These initial structures were optimized at the HF/6-31G* level of theory using Gaussian 09[164]. The RESP charges for LB, AOS-14, and octane were derived

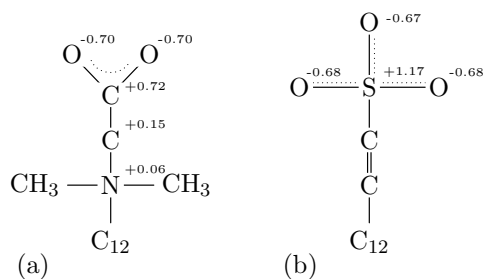


Figure 5.1 : Schematic of the head-group of (a) lauryl betaine (LB) and (b) alpha olefin sulfonate 14 (AOS-14). LB is zwitterionic, while AOS-14 is anionic. Lauryl betaine has an alkyl chain length comprising 12 carbons, while AOS-14 has an olefinic chain comprising 14 carbon atoms.

based on these geometry optimized structures using the R.E.D.-III.5 tool [165]. Force field parameters were assigned using generalized AMBER force field [166, 49] with the *antechamber* of AMBER. Water was modeled using the TIP4P-2005 model [167]. Molecular simulations were performed using the GROMACS [101] 4.6.5 simulation package.

All simulations were performed in the isothermal-isobaric (NpT) ensemble at a temperature of 300 K and pressure of 1 bar. The temperature is controlled via a modified Berendsen thermostat [168] and the pressure is controlled using the Parrinello-Rahman [169] barostat. We allow for a semi-isotropic pressure coupling so that the x and y dimensions of the simulation box could alter independently from the z dimension. This pressure coupling scheme has been widely used in previous studies of tensionless monolayer/bilayer [170, 171, 172]; here we assume the LB/AOS-14 monolayer is tensionless based on the fact that the interfacial tension measured is close to zero for this LB/AOS system [173]. Allowing for semi-isotropic fluctuations of the cell volume also greatly reduces the computational effort to study the monolayer [174]. We monitor the convergence of the x - and y -dimensions of the box in the pre-

equilibration conducted over 40 ns. After the lateral dimensions are reliably stable, we perform a production run for 10 ns.

We use the leap-frog algorithm [175] with a 2 fs time step to integrate the equations of motion. The SETTLE algorithm [176] is applied to water molecules and other bonds in the system are constrained by LINCS algorithm [177]. Periodic boundary conditions are applied in all directions. Electrostatic interactions are described using the particle mesh Ewald technique with a real-space cut-off distance of 1.4 nm. The same distance was used to cut-off van der Waals interactions.

It is not feasible to study the spontaneous self-assembly of the surfactants at an octane/water interface. So all simulations were started from preassembled configurations with the water phase in the center of the simulation cell, sandwiched by two octane slabs, and surfactants located at the octane/water interface. The surfactants were placed randomly at the interface. The counterion Na^+ is placed randomly in the water phase. The initial box dimension is $10 \text{ nm} \times 10 \text{ nm} \times 11 \text{ nm}$. The initial thickness of the water phase is 6 nm. The Packmol [178, 179] program was used to preassemble the simulation cells. Seven (7) simulations with different LB to AOS-14 ratios covering the whole range of composition were considered as indicated in Table 5.1. The difference in the number of water molecules will not affect the result since only the oil/water interface is of an interest and the transport of surfactants from the interface to the bulk region is limited due to the short time scale(ns) in molecular dynamics simulation.

5.3 Results and discussion

We first discuss the role of LB in modulating the structural properties of the monolayer. Subsequently, we discuss the energetics, particularly the role of LB in modu-

Table 5.1 : Compositions of the various systems studied in this work. The number of molecules in each system is noted in the columns.

System	AOS-14	LB	Na ⁺	octane	wate
1	400	0	400	1900	13944
2	360	40	360	1900	16087
3	280	120	280	1900	13853
4	200	200	200	1900	13777
5	120	280	120	1900	15723
6	40	360	40	1900	13549
7	0	400	0	1800	13463

lating monolayer elasticity.

5.3.1 Area per molecule

The interfacial area per molecule has been shown to correlate with the surface shear viscosity, with a smaller area per molecule correlating with a maximum in the surface shear viscosity and a minimum in drainage of the film in a foam [163]. Since calculating shear viscosity directly from simulations is a daunting computational exercise, we instead examine the behavior of the average area per molecule and rely on the correlation of the surface shear viscosity with area per molecule to guide our investigation of the present system. To this end, we calculate the area of the simulation cell in the $x - y$ plane and, by neglecting the minor buckling of the interface, equate this quantity to the interfacial area occupied by the surfactant. The buckling of the interface is very minor to the system containing AOS and is mainly introduced by the dipole moment carried by LB heads making the alignment of LB molecules in the interface

difficult. (The snapshots of the simulation boxes are provided in the supplementary material(Appendix B).) On this basis we calculate the area per molecule (Fig. 5.2).

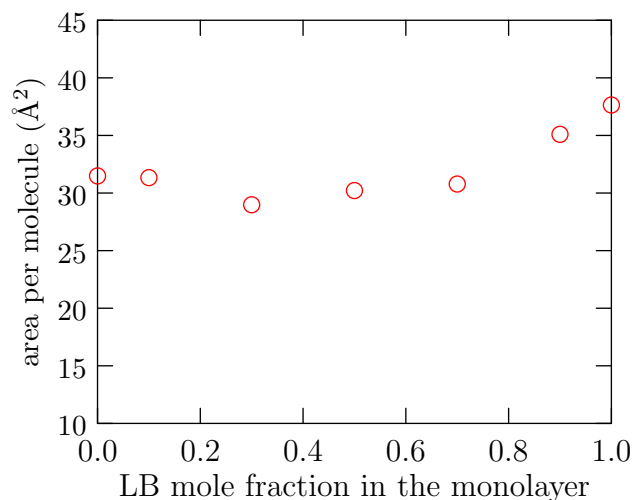


Figure 5.2 : Area per molecule averaged over 10 ns. The standard error of the mean is negligible compared to the size of the symbol.

If LB and AOS formed an ideal solution, the area per molecule would depend linearly on the LB mole fraction. However, this is not the case. Instead the trend is non-monotonic with a minimum around 30% LB mole fraction. The interface with pure AOS-14 has an area per molecule of approximately 32 \AA^2 . As the mole fraction of LB in the surfactant monolayer increases, the area per molecule stays roughly constant until the mole fraction of LB reaches 10%. Then it reaches a minimum at 30% LB mole fraction. Between 30% LB and 70% LB there is a modest increase in area, with a more pronounced increase in area after 70% LB. For pure LB, the area per molecule is 38 \AA^2 . (The interfacial area is higher for pure LB compared to AOS, partly due to the larger size of the head group (Fig. 5.1).) The overall trend agrees with area estimated using the experimentally measured surface tension isotherm and its interpretation within regular solution theory[173]. Based on the experimentally

identified correlation between area per molecule and surface shear viscosity, we expect the interface with 30% LB should show a high shear viscosity and also produce a foam that is more stable than that obtained using pure AOS alone.

5.3.2 Surface distribution of LB in the monolayer

Figure 5.3 compares the pure component pair correlation g^{N-N} (for LB) and g^{S-S} (for AOS) with the N-S correlation function g^{N-S} for an LB composition of 30%. (NB: the

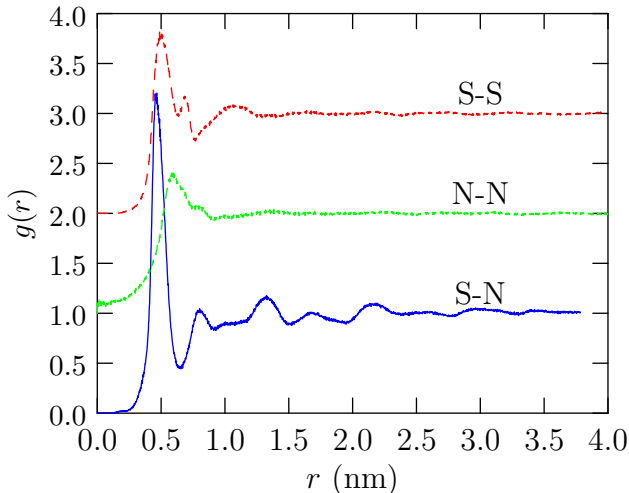


Figure 5.3 : Pair correlation functions for various surfactant systems. S-N correlation (blue curve) in 3:7 mixture of LB and AOS; N-N correlation for neat LB (green), and S-S correlation for neat AOS (red).The curves are offset for clarity.

pair correlation functions are measured in the $x-y$ plane. Further, for pure LB, g^{N-N} does not equal to 0 at $r = 0$ due to slight buckling of the interface.) The correlation functions reveal that at the composition leading to a minimum area, the first peak of g^{N-S} occurs at a smaller separation (relative to the pure component correlations) and has a substantially higher peak. This enhanced local order is suggestive of favorable interactions between the anionic surfactant (AOS) and the foam booster (LB).

The z -dependent density distribution $\rho(z)$ (Fig. 5.4) provides additional insights into the aforementioned favorable interaction. We find that the N (from LB) and S (from AOS) atoms are nearly in the same plane, whereas the carboxylate group (from LB) juts into the aqueous phase. This configuration should maximize the electrostatic interaction between the head groups and also aid in the solvation of the

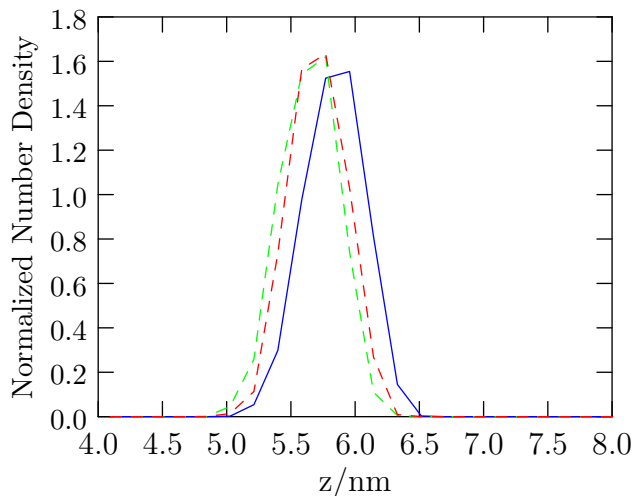


Figure 5.4 : Normalized density profile for nitrogen (green), sulfur (red), and carboxylate carbon (blue) in 3:7 mixture of LB and AOS in a direction perpendicular to the interface. $z = 0$ nm defines the center of the octane slab and $z = 8.8$ nm approximately corresponds to the center of the water slab. The density distribution of each component is normalized by $\int \rho(z)dz$, where the integration is across the oil/water interface.

carboxylate. On the other hand, a configuration where C (from LB) and S (from AOS) are in the same plane, as would be needed to maximize packing of the alkyl chains, is clearly disfavored due to the electrostatic repulsion between C and S and the expected diminished hydration of the carboxylate group. Our simulation results confirm the structural configuration suggested by Wydro et al. [180], but there is a caveat. In the analysis by Wydro et al., guided by the conventional assignment of formal +1 or -1 charges to charge sites on surfactant head-groups, one LB pairs with one anionic

Table 5.2 : Local composition versus overall composition of LB in the monolayer. The local composition is given by $LB_{local} = (N_{LB} + 1)/(N_{LB} + N_{AOS-14} + 1)$, where N is the number of particles (either LB or AOS) within the first shell of the distinguished LB molecule. (These N values are standardly obtained from the pair correlation.)

$LB_{overall}\%$	N_{AOS}	N_{LB}	LB_{local}
10	3.68	0.11	23.22
30	3.42	0.42	29.36
50	2.33	0.96	45.73
70	1.36	1.73	66.76
90	0.38	2.08	89.06

surfactant. However, with head-groups with a partial charge distribution, as is the case in our simulation models, this 1:1 pairing is not expected. Indeed, analysis of local composition around an LB molecule versus the overall composition (Table 5.2) shows that in all the systems except the one with 10% LB, the local composition is nearly the same as the overall composition, indicating that the system is well-mixed and no 1(LB):1(AOS) pair pattern exists. (The discrepancy is high for the 10% LB system because of sampling limitations associated with the smaller total number of LB molecules.)

5.3.3 Role of LB in the structure of surfactant monolayer

The foam booster LB also impacts the structure of surfactant monolayer in a concentration dependent fashion. To study this we calculate the tilting angle of the LB head and the order parameter of surfactant tails.

The orientation of the head of LB is investigated by measuring the angle between the carbon-carbon vector in the -N-C-CO₂ head-group of LB and the monolayer

normal z axis. The results are shown in Fig. 5.5. We find that the head group of LB

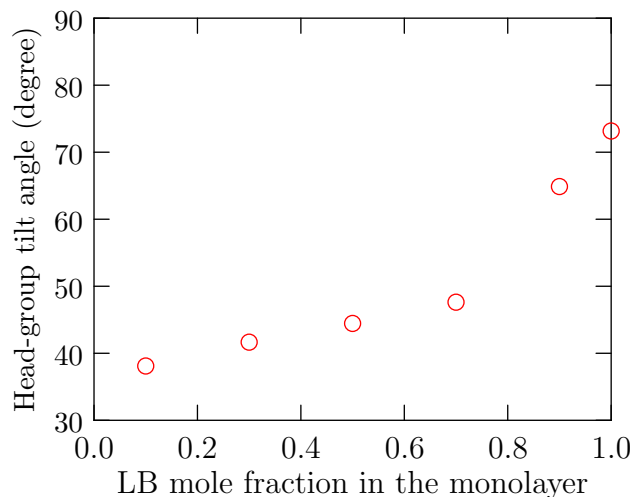


Figure 5.5 : Angle between C-C vector in the LB head-group (-N-C-CO₂) and the monolayer normal. The standard error of the mean is negligible on the scale of the graph.

is tilted relative to the monolayer normal and the tilt angle increases with increasing LB concentration. After about 70% LB, the tilt angle increases faster and the head of LB becomes nearly parallel to the monolayer.

The re-orientation of the LB head-group can be modulated by the anionic surfactant AOS-14. In essence, the favorable interaction between the S (AOS) and N (LB) surfactant atoms and the hydration of the carboxylate group of LB can inhibit the tendency of pure LB head-groups to become nearly parallel to the monolayer. This change of orientation alters the effective head group size and thus the area per molecule (Fig. 5.2). Thus despite the fact that the LB head-group (in pure LB) occupies a larger area than the head group in pure AOS, in the mixture, the effective head-group size is lower because the flexibility the head-group is suppressed by favorable interactions. Of course, when the proportion of LB is high ($\geq 70\%$), favorable

AOS-LB interactions are not sufficient in constraining the head-group orientation leading to an increase in area per head group (Fig. 5.2).

The ordering of the surfactant tails is also affected by the interaction between head-groups. To explicate this, we define an order parameter

$$S = \frac{3 \langle \cos^2 \theta \rangle - 1}{2}, \quad (5.1)$$

where θ is the angle between the vector of interest and the monolayer normal (z axis) and $\langle \dots \rangle$ indicates ensemble average. For the surfactant tail, the order parameter is defined per carbon site (i), where θ is angle between the normal and the vector connecting the two adjacent carbon atoms $i - 1$ and $i + 1$. Clearly, S ranges from $-\frac{1}{2}$ to 1. When $S = -\frac{1}{2}$, the vector is parallel to the monolayer/interface, whereas when $S = 1$, the vector is normal to the monolayer/interface. When $S = 0$, the vector of interest does not have preferential orientation.

In Fig. 5.6 we present the order parameter averaged over all carbon atoms in surfactant tails. The lower bound is the order parameter of the carbon atom that is next to the terminal one. Terminal carbon atoms have smaller order parameter since they are less confined. Several interesting points can be observed. First, a surfactant monolayer consisting of pure AOS-14 is slightly more ordered than the monolayer formed by pure LB. This result is consistent with the area per molecule, pair correlation function, and flexibility of the LB head-group. When the LB head-group lays flat on the interface (C-C bond vector in the head is nearly parallel to the interface), the alkyl tail LB has more freedom and hence is less ordered than AOS-14. Second, the averaged order parameter remains constant as LB mole fraction increases, decreasing only after the LB mole fraction increases beyond 70%, when there fewer AOS molecules to bind with the LB molecules. What this shows is that, although the LB molecule has a larger head group which could decrease the ordering

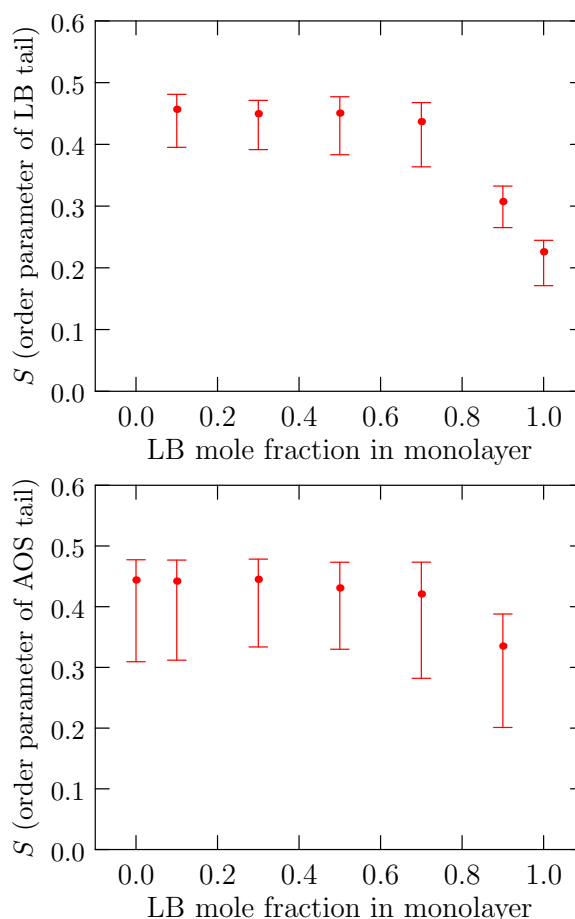


Figure 5.6 : Average order parameters for surfactant hydrocarbon chains of LB (left panel) and AOS-14 (right panel).

of surfactant tails, this negative effect is offset by the favorable interaction between LB and AOS-14.

Accepting the correlation between surface shear viscosity, packing of surfactant molecules at the interface, and foam stability [163], the above observations suggest why LB alone is not a good foamer: LB alone cannot form a closed packed monolayer needed to increase the shear viscosity. However in surfactant blends, the synergistic effects discussed above can lead to better packing than either pure component surfactant. This is why LB is a foam booster but not a good foamer[181].

5.3.4 Binding energy of LB and surface dilatational modulus

As a final piece in confirming the structural analysis above, we calculated the binding energy of one distinguished LB molecule with the rest of surfactants in the monolayer. The binding energy was calculated by summing up the potential energy of interactions between a distinguished LB and the rest of the surfactant molecules in the same monolayer. This was conducted over all the LB molecules in the system and an average value was calculated over time and number of LB molecules. Fig. 5.7 shows that the binding energy of the distinguished LB decreases as the proportion of LB increases in the monolayer till it reaches a minimum at about 30% composition. Subsequently the binding energy increases, indicating that favorable interaction of the LB with the rest of the surfactants is maximized at about 30% composition.

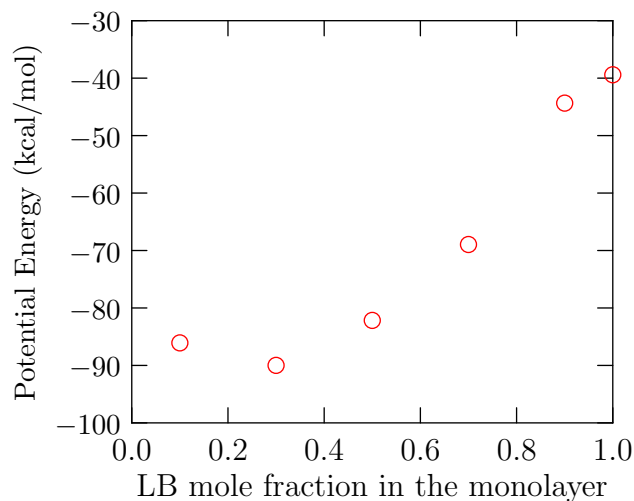


Figure 5.7 : Binding energy of a distinguished LB with the rest of surfactants in the monolayer. The statistical uncertainty is smaller than the size of the symbols.

All of the above analysis suggests that the interface will most resist expansion, a precursor for breakage of the pseudo-emulsion film, at an LB composition of 30%.

We quantify this property using the surface dilatational modulus defined as [182]

$$\varepsilon = \frac{d\sigma}{d \ln A} \quad (5.2)$$

where ε denotes surface dilatational modulus, σ is the interfacial tension, and A is the surface area. The surface dilatational modulus is related to the Gibbs Elasticity ($E = \frac{2d\sigma}{d \ln A}$) that describes the stability of a thin film. However, due to the existence of interaction between the two interfaces, that is to say there is a finite disjoining pressure, the Gibbs elasticity cannot be obtained simply by multiplying surface dilatational modulus by a factor of two.

Physically the surface dilatational modulus describes the capacity of the interface to increase its interfacial tension upon an increase of surface area. Greater the dilatational modulus, greater is the work required to stretch and break the interface. Thus ε is a direct measure of the stability of a monolayer to resist the perturbation. Additionally, it has been shown experimentally that surface elasticity is important to the foam stability[183]. We calculated the surface dilatational modulus using Eq.(5.2) together with a 7% areal perturbation[184] applied to each monolayer in our simulation cell. The interfacial tension of each perturbed surfactant monolayer was collected from ≈ 6 ns production runs using the pressure tensor method[185] integrated in GROMACS and the dilatational modulus was calculated by numerical differentiation.

The calculated dilatational modulus is shown in Fig. 5.8. The surface dilatational modulus of AOS-14 has been measured experimentally at the gas/water interface by Huang et al.[186]. The measured dilatational modulus of AOS-14 is around 6 mN/m while that of AOS-16 is around 40 mN/m. Our results of AOS-14 at the oil/water interface is 39 mN/m which is within the same range of values. (A strict comparison is limited by the different interfaces considered and also by limitations in the simulation

MD that cannot capture the exchange of surfactant molecules between bulk solution and interface.) The result shows that the surfactant monolayer consisting of 30% LB has the greatest surface dilatational modulus, indicating the highest resistance to external perturbation. In contrast, the monolayer consisting of pure LB has the smallest modulus, indicating the lowest stability. So LB by itself is not a good foamer in this circumstance. The trend of surface dilatational modulus is in good accord with our analysis of the area per molecule (Fig. 5.2) and the binding energy of LB (Fig. 5.7). Indeed, as the film is expanded by an external perturbation, the average inter-surfactant distance will be increased thereby increasing (making less favorable) the binding energy between the surfactant molecules. But as the binding energy analysis shows, this will be most unfavorable for the interface with 30% LB.

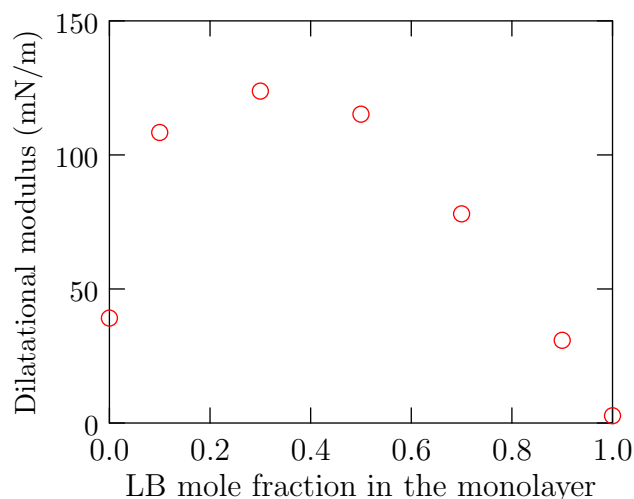


Figure 5.8 : Surface Dilatational Modulus obtained using Eq. 5.2. The surface tension in Eq. 5.2 was calculated using the pressure tensor for systems differing in area by 7% from the equilibrium value.

5.4 Conclusion

We investigated the surfactant monolayer stabilized by the anionic surfactant AOS-14 and the foam booster lauryl betaine (LB) at an octane/water interface using molecular dynamics simulation. Favorable interaction between head-groups and the flexibility of the LB head-group are found to be important in determining the synergistic interaction between the surfactants. The head-group of LB is flexible enough that it tends to orient parallel to the oil/water interface, in turn leading to poor packing and a higher area per head-group (relative to the anionic surfactant AOS). On the basis of the experimentally observed correlation between surface shear viscosity, packing of surfactant molecules at the interface, and foam stability, LB alone is not expected to be a good foamer. However, in the AOS-LB blend, the foam booster (LB) mediates and enhances the effective interaction between the AOS molecules leading to an overall closer packing than either pure surfactant; this effect is enhanced for a 30% composition of LB in the monolayer. For this mixture, the binding energy of a distinguished LB in the monolayer is the lowest and the dilatational modulus of the monolayer is the highest, indicating stability of the interface to distortion.

In this work we have not investigated the impact of specific salt type and composition on foaming. Additionally, the branching of surfactants may also affect their interfacial properties[187, 188]. These aspects are undoubtedly important in designing surfactant blends to stabilize foam. Investigations along these lines are part of our on-going work.

Chapter 6

Molecular Dynamics Simulation Study on the Adsorption of Naphthenic Acids on Calcite (10 $\bar{1}$ 4) Surface

6.1 Introduction

Wettability is defined as the tendency of one fluid to spread on, or adhere to, a solid surface in the presence of other immiscible fluids and it refers to the interaction between fluid and solid phases. The wettability of reservoir rock is an important factor affecting the efficiency of water-flooding processes. An oil-wet rock matrix will prevent water from spontaneous imbibition[189] and the injected fluid(water) must overcome the barrier introduced by capillarity to displace the original oil in place(OOIP). Hence, the oil recovery from oil-wet reservoirs can generally be very poor[190] by water-flooding processes. If the wettability of the reservoir rock is altered from oil-wet to water-wet, the injected fluid(water) can spontaneously invade the rock matrix, resulting in more oil being displaced[191] and improved oil recovery. It was recognized that the wettability of rock surface can be greatly modified by the adsorbents such as organic acids present in crude oil and later adsorbed on the surface[192]. Once adsorbed, the hydrophobic tails of the organic acids can behave like the anchors for the adsorption of oil molecules onto the surface[193], showing a change in wettability. To better understand the wettability of reservoir rocks and develop new techniques for improving oil recovery, studying the mechanism of the

adsorption process of the acids onto minerals can be an important contribution.

The wettability of carbonates attract lots of attention due to the fact that about 50% of world discovered oil reserves are in carbonates[194] and carbonate reservoirs dominate the Middle-East petroleum fields. Although carbonate surface is originally hydrophilic or water-wet, around 80% carbonate reservoirs are preferentially oil-wet under reservoir conditions, making water flooding less effective. The reason why carbonate reservoirs are oil-wet or mixed-wet can be largely attributed to the adsorption of carboxylates from the crude oil to the surfaces[192, 190, 195]. Considerable effort has been made on developing new methods to mediate the adsorbed acids and alter the wettability of carbonate surfaces. It was found that cationic surfactants such as $R-N^+(CH_3)_3$ are able to desorb the adsorbed carboxylates due to the strong electrostatic affinity between the adsorbed carboxylates and cationic surfactants and the formation of cat-anionic surfactant pairs[195]. It was also proposed that potential determining ions such as Ca^{2+} , Mg^{2+} , and SO_4^{2-} can help desorb carboxylates[196, 197] from the surface. Additionally, Seethepalli et al.[190] showed that anionic surfactants can be effective in changing the wettability of the calcite surface from an oil-wet state to an intermediate or water-wet state. Not related to the desorption of carboxylates, this wettability alteration process may be explained by the adsorption of anionic surfactants onto the adsorbed layer of carboxylates through their hydrophobic tails and hydrophobic interactions, exposing their hydrophilic heads and making the surface hydrophilic[191]. It was also mentioned that adding potential determining ions such as carbonates dramatically decreases the loss of anionic surfactants. Nonetheless, a molecular-level understanding of the interaction between carboxylates and carbonate surfaces is still lacking in the literature and will be the subject of this chapter.

To investigate the interaction between carboxylates and carbonate surfaces, we

opt to calculate the free energy of adsorption of deprotonated naphthenic acids on calcite ($10\bar{1}4$) surface using molecular dynamics simulation. It was found that the adsorption free energy can be greatly affected by the hydrophobic moiety of the acids: longer tail naphthenates adsorb more strongly. Furthermore, the free energy of adsorption exhibits an inverse-temperature behavior: an increase in temperature enhances the free energy of adsorption, a signature of hydrophobic interactions[198]. This agrees with the experimental observation made by Young et al.[199], who showed that the adsorption of carboxylic acids on calcite surfaces is an endothermic process and increases with temperature at low carboxylic acid concentration. Based on these two findings, it can be inferred that hydrophobic tails can be important in the adsorption of acids onto calcite ($10\bar{1}4$) surface. Hydrophobic interactions affecting the adsorption of amphiphilic molecules onto charged surface is not a new finding: it was shown experimentally by Hu et al.[200] that this interaction is very important to the adsorption of dye molecules on resins. By decoupling the free energy of adsorption to entropic and enthalpic contributions, it was found that the adsorption process is driven by entropy, another signature of hydrophobic effect, which also confirms Young et al.'s speculation[199]. The free energy of adsorption is further compared against that of a potential determining ion carbonate. We showed that, it is energetically favorable for the carbonate ion to displace naphthenic acids with shorter tails from the ($10\bar{1}4$) surface. However, it can be inferred that the displacement will be less favorable when the acids bear bulkier tails.

6.2 Model and Methods

Here, the calcite surface being studied is the ($10\bar{1}4$) surface. As the most abundant calcite surface on Earth, the ($10\bar{1}4$) surface has been shown to be the most stable

among all calcite facets theoretically and experimentally[201, 202]. To model the calcite crystal and the $(10\bar{1}4)$ surface, the force field developed by Raiteri et al.[203] is utilized. In this force field, the intramolecular interactions between atoms in the carbonate group are ignored, resulting in a rigid molecule force-field. Based on the detailed geometric information of the unit cell in the work by Stockelmann et al.[204], the calcite crystal was constructed. The crystal made of $6 \times 6 \times 6$ unit cells(432 CaCO_3) in $x - y - z$ directions was put in the center of the simulation cell covered by two layers of water modeled with TIP4P2005 water model[167]. The thickness of the mineral slab is approximately 2 nm and that of each water slab is around 4 nm. To avoid unphysical water density, two vapor slabs(2 nm thick each) are placed above the two layers of water respectively. The final dimensions of the cubic simulation cell are $4.8576 \times 2.994 \times 14$ nm in x , y , and z directions (Fig. 6.2).

The GROMOS 54A7 force field[205] is used to describe the rest of interactions between different species in the system. The molecular structure of the deprotonated naphthenic acid ($\text{C}_5\text{-C}_9\text{-CO}_2^-$) was derived based on the average molecular weight(248 g/mol) of the experimentally accessible naphthenic acids, where C_5 represents cyclopentyl group. The schematic of the molecular structure of the acid $\text{C}_5\text{-C}_9\text{-CO}_2^-$ is shown in Figure 6.1. The topology of the molecule was generated using PRODRG server[206]. To study the effects of tail length on the free energy of adsorption, an acid with shorter tail length($\text{C}_5\text{-C}_2\text{-CO}_2^-$) was also constructed in the same fashion.

Molecular dynamics simulations were performed in GROMACS/4.6.5 simulation package[101] in the NVT (fixed number of particles N , volume V and temperature T) ensemble. The temperature was controlled via a modified Berendsen thermostat[168] scheme. We used the leap-frog algorithm[175] with a 2 fs time step to integrate the



Figure 6.1 : Schematic of $C_5-C_9-CO_2^-$ where C_5 represents cyclopentyl.

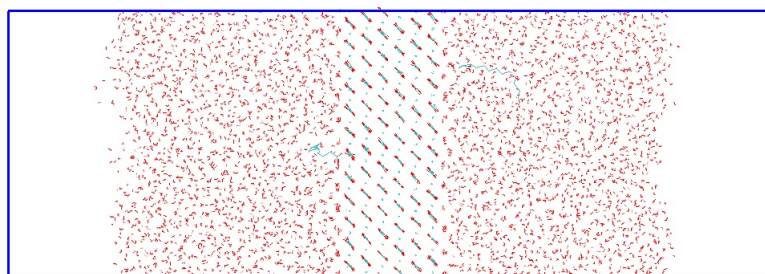


Figure 6.2 : Illustration of the simulation box. The calcite crystal(in the middle) is sandwiched by two water phases(red dots) which is in coexistence with their vapor phases(blank space). The green lines in water phase represents deprotonated naphthenic acid molecules.

equations of motion. The SETTLE algorithm[176] was applied to water molecule and other bonds in the system were constrained by LINCS algorithm[177]. Periodic boundary conditions were applied in all directions and the particle mesh Ewald technique was used for the electrostatic interactions. A cut-off distance of 1.4 nm was used for the real-space electrostatics and van der Waals interaction.

Simulating the adsorption process of molecules from the water phase to calcite surface is time-consuming and computationally expensive in molecular dynamics simula-

tion. To accelerate this adsorption process and calculate the free energy of adsorption, the steered molecular dynamics simulation(SMD) technique is utilized[207]. An external force is assigned to the carboxylic group of the molecule to pull it toward the surface. After sampling the configurations of the molecule at different distance to the surface, the weighted histogram analysis method(WHAM)[208] in the *g_wham* module [209] is used to calculate the free energy of adsorption. This methodology has been applied by Lemkul et al.[210] to study the stability of Alzheimer’s Amyloid Protofibrils and by Chun et al.[192] to study the desorption of a carboxylic acid from an oil/calcite interface.

To decouple the entropic and enthalpic contributions to the free energy of adsorption, we rely on the potential of mean force or free energy profiles obtained at different temperatures. The entropy S can be obtained by[211],

$$-S(z) = \frac{\Delta A(z, T + \Delta T) - \Delta A(z, T)}{\Delta T} \quad (6.1)$$

where A is the Helmholtz free energy obtained from umbrella sampling, z is the reaction coordinate defined as the normal distance between the center of mass(COM) of carboxylic group of the acid and the calcite surface, and T is absolute temperature. The enthalpic contribution to the free energy, $\Delta H(z)$, can be calculated in NVT ensemble using the following equation:

$$\Delta H(z) = \Delta U(z) = \Delta A(z) + T\Delta S(z). \quad (6.2)$$

6.3 Results and Discussion

6.3.1 Water Structure at the Calcite/Water Interface

Recognizing that the adsorption of carboxylates can be affected by the solvent environment, the structure of water close to the calcite surface is of an interest. The

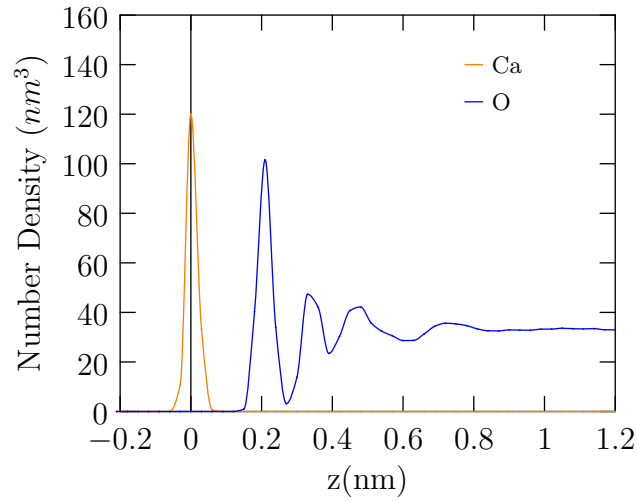


Figure 6.3 : Number density distribution of calciums in calcite and oxygens in TIP4P/2005 water model.

structure of the liquid water in contact with the calcite surface has been studied both computationally [212, 213, 214, 203] and experimentally[215]. At the calcite/water interface, water molecules are highly structured due to strong electrostatic interaction between water molecules and the calcite surface and this is illustrated in Figure 6.3 in which the number density of oxygens of water molecules is plotted against z axis that is normal to the calcite surface. The origin of coordinate is chosen to be the average position of calciums in the outermost layer of the calcite ($10\bar{1}4$) surface. This definition of the position of the calcite surface will be carried hereafter. We can see that four(4) layers of water molecules are present within 8 \AA to the surface. After 8 \AA , the water density converges to its bulk value.

Due to the strong interaction between water and calcite, it can be anticipated that water molecules are confined in certain orientations close to the surface. The orientations of water molecules can be illustrated by examining the angle between the dipoles of water molecules and z axis that is normal to the surface. The averaged

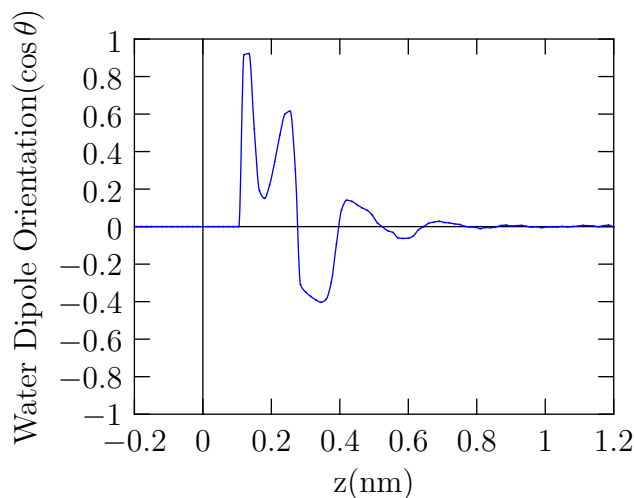


Figure 6.4 : Orientation of water molecules. x axis is the distance of oxygen atoms from the surface. y axis represents the cosine values of the angles between dipoles of water molecules and surface normal averaged over molecules and time.

cosine values of the angles as a function of distance from the surface are plotted in Figure 6.4. Clearly, water molecules are highly ordered. We can see that, about $1 - 3 \text{ \AA}$ from the surface, the cosine value is positive, meaning that the first layer of water molecules (defined by the position of oxygens) are at acute angle to the normal of the calcite surface with oxygen atoms binding to the calcium atoms of the surface. When z is in the range from 3 \AA to 4 \AA , the values are negative, indicating that the second layer of water molecules are at obtuse angle to the normal of the surface with hydrogen atoms of water hydrogen bonding to the surface oxygen atoms. As z further increases, the averaged cosine value converges to 0, indicating no specific ordering of water dipoles in the homogeneous bulk region. The structure of TIP4P/2005 water close to the calcite surface obtained from this study is very similar to that of other water models studied by Kerisit et al. [213] and Raiteri et al. [203].

Due to the structuring of water molecules at the surface, electrical double layers formed by oxygens (negatively charged) and hydrogens (positively charged) of water

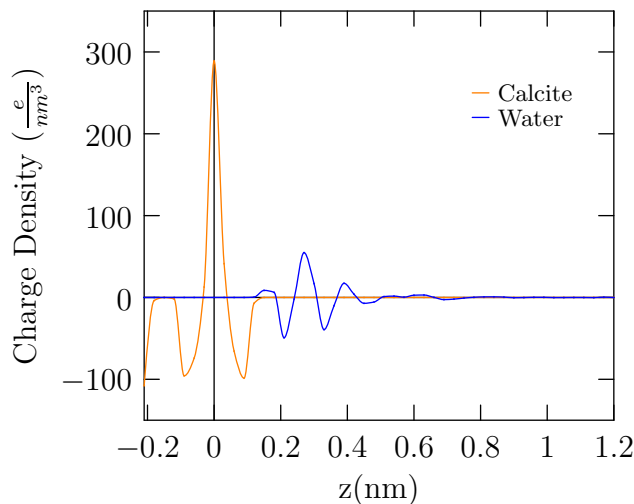


Figure 6.5 : Charge distribution of calcite/water interface

molecules are anticipated. To unveil this information, the charge density distribution is calculated and plotted in Figure 6.5. Well-defined peaks are observed and they correspond well with the density profile of oxygens of water molecules. At closest contact (around 1.5 Å), the water layer has a positive charge density, due to the aggregation of hydrogens induced by the hydrogen bonding between surface oxygens in the carbonate groups and hydrogens of water molecules. This hydrogen bonding network also contributes to the orientation of the second layer of water molecules (defined by the positions of oxygens) as mentioned before. As z increases, the charge density becomes negative due to the large number of oxygen atoms around 2 Å shown in Figure 6.3. This is due to strong electrostatic attraction between water oxygens and calcite calciums. Further apart from the surface, charge density becomes positive again, and so on and so forth. This electrical double layer structure is only prominent within 8 Å to the surface. After this critical distance, water regains its bulk homogeneous structure and the charge density converges to 0.

Due to the existence of the structured water layer and the electrical double layer induced by the calcite surface, charged species can adsorb onto the surface. This agrees with our conventional understanding. It can be anticipated that the adsorption of charged species on the calcite surface is greatly affected by the presence of water molecules, making the explicit consideration of water molecules important, which can be too computationally expensive for quantum calculations.

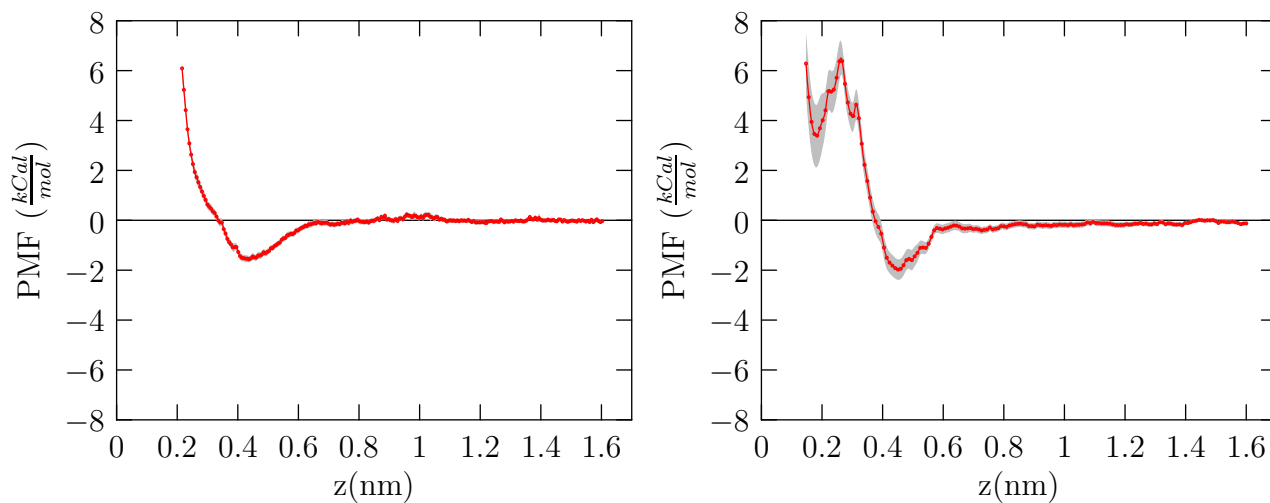
6.3.2 Adsorption of Deprotonated Naphthenic Acids on Calcite

As introduced before, organics from the crude can adsorb onto reservoir rock surfaces and alter the wettability. This has been regarded as the origin of calcite surface being preferentially oil-wet under reservoir conditions. The adsorption of acids is generally recognized to be governed by the electrostatic interaction between the charged surface and oppositely charged acid molecules but little attention was paid to the hydrophobic tails. However, the acid tails can also be important in the adsorption process. It was shown by Hu et al.[200] that the tail is very important to the adsorption of dye molecules on charged resins. To unveil the contribution of hydrophobic tails, we investigated the free energy or potential of mean force of adsorption of three different acids with various tail length: one hypothetical acid without tail, one with C₂-C₅ tail and one with C₉-C₅ tail. The one with no tail is represented by an imaginary monovalent carbonate ion. The topology of the imaginary monovalent carbonate ion is the same as the one in calcite crystal with the partial charges scaled by 0.5.

Each free energy profile as a function of distance to the surface was calculated by umbrella sampling technique and weighted histogram analysis method(WHAM). A series of MD simulations, each for 5 ns in production run, with the center of mass(COM) of the carboxylic group constrained at various distance from the sur-

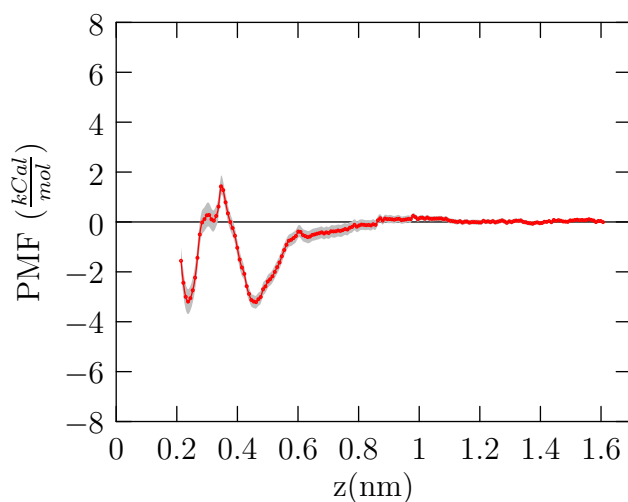
face (whose position is defined by the position of calciums at outermost layer) were conducted. To generate the initial configurations for the 5 ns sampling simulations, an independent steered molecular dynamics simulation was conducted beforehand. In this process, the carboxylic group was initially placed 2 nm from the surface and pulled toward the surface with the configurations of molecules saved at 0.02 nm intervals, which were used as the starting configurations for the umbrella sampling. The final free energy profiles are shown in Figure 6.6. Several interesting points can be observed. First, the adsorption of acids is energetically favorable, which agrees with our intuition and experimental observations. Second, two states of adsorption are observed: the acid head group can be either in direct contact with the surface forming inner sphere complex or in contact with the water layer adsorbed on the surface forming outer sphere complex. We can see that the separation of the two energy wells is 3 Å that equals the generally accepted diameter of water molecule. Hence, a single layer of water molecules is attached on the surface when the outer sphere complex is formed and stable. Third, the adsorption free energy is greatly affected by the size of the acid tails. The acid with longer tail has a larger adsorption energy and adsorbs more strongly onto the surface. So the hydrophobic moiety of the acids does affect the adsorption and should not be overseen.

The third observation can be understood based on a simple argument. Since the hydrocarbon chain cannot form hydrogen bonds with water molecules, longer hydrocarbon tail results in lower solubility of the acid in water. Further, since the water molecules at the surface are highly ordered, acid molecules displacing the water molecules from the surface can be entropically favorable, due to the release of water molecules from the interface (a low entropy state) to the bulk region (a high entropy state). These two effects contribute to the aggregation between the surface and



(a) imaginary monovalent carbonate ion("naphthenic acid" with no tail)

(b) naphthenic acid with $C_2 - C_5$ tail



(c) naphthenic acid with $C_9 - C_5$ tail

Figure 6.6 : Potential of mean force(PMF) of naphthenic acids with different tail length at 300 K: a) no tail, b) $C_2 - C_5$ tail, c) $C_9 - C_5$ tail. The PMF is normalized by kT , where k is the Boltzmann constant and T is absolute temperature. The gray shades are the statistical error estimated by using Bayesian bootstrap method.

the acid molecule. It is also implied that the calcite ($10\bar{1}4$) surface is relatively less hydrophilic compared with water. We suspect that the reorientation of water molecules at the surface contributes to a ‘hydrophobic’ surface as can be seen from the extremely low density of water at 2.7 Å shown in Figure 6.3. As a result, the similarity between the interaction between the calcite surface and the acid molecule and the attractive hydrophobic interaction is not surprising.

6.3.3 Effect of Temperature on Adsorption at Low Acid Concentration

Another representing signature of the hydrophobic interaction is that it augments with the increase in temperature. Indeed, the adsorption of carboxylic acids is a function of temperature: it was observed experimentally the adsorption of oleic acids on calcite increases as temperature rises[199] at low acid concentration. To investigate the origin of this phenomenon, the potential of mean force of the acid with C₉-C₅ tail is calculated at elevated temperatures(310 K) and shown in Figure 6.7.

Similar to the potential of mean force at 300 K, there are two energy wells at the same positions. It can be seen that, at elevated temperature, both of the inner sphere complex and outer sphere complex become more energetically favorable. Based on the free energy profiles, increasing temperature indeed enhances the adsorption at low acid concentration, which agrees with the experimental finding and further confirms the hydrophobic interaction between the acid molecule and the calcite surface.

6.3.4 Adsorption Driving Force

In the experimental work by Young et al.[199], this endothermic phenomenon is attributed to the chemisorption and it was suspected that the appearance of ‘chemisorption’ is related to the entropy of water. But no direct evidence was provided. As men-

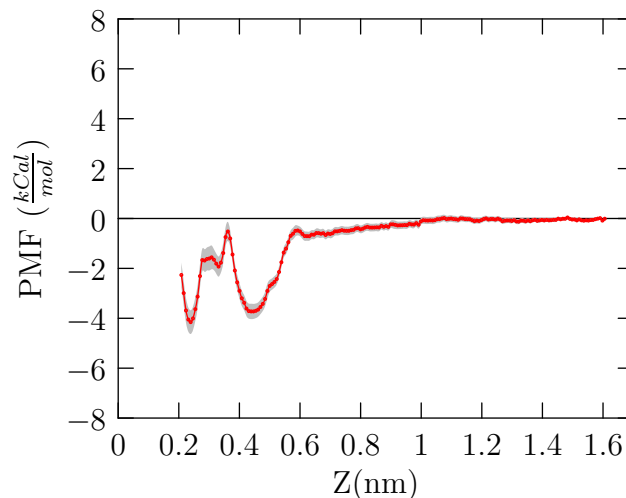


Figure 6.7 : Potential of mean force of the $C_5 - C_9 - COO^-$ naphthenic acid at 310 K. The gray shades are the statistical error estimated by using Bayesian bootstrap method.

tioned previously, the adsorption of an acid molecule may be entropically favorable due to the release of highly constrained water molecules from the surface to the less confined bulk environment. To test this speculation more rigorously, we decoupled the free energy of adsorption to two contributions: entropy and enthalpy. The entropic and enthalpic contributions to the free energy of adsorption of the acid molecule onto the calcite surface at 300 K were obtained based on Eq. 6.1 and Eq. 6.2 and the free energy profiles shown in Figure 6.6(c) and Figure 6.7. The results are shown in Figure 6.8.

We can see that the enthalpic contribution ΔH is positive, which disfavors the adsorption. In the meanwhile, the entropic contribution $-T\Delta S$ is negative, which favors the adsorption. So the adsorption process is indeed entropically driven, consolidating the existence of hydrophobic interaction and Young et al.'s speculation[199].

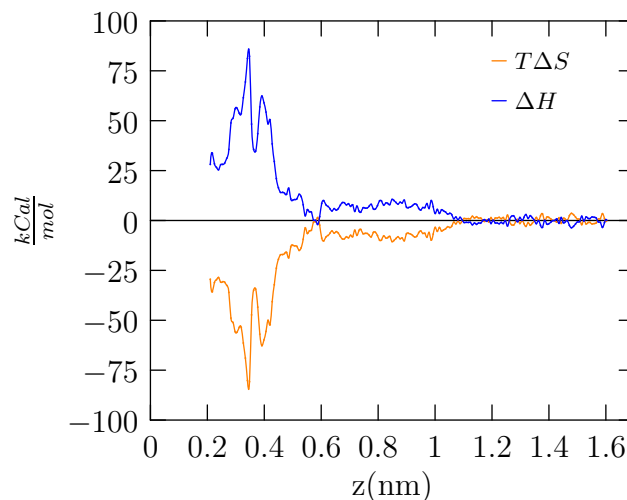


Figure 6.8 : Entropic($-T\Delta S$) and enthalpic(ΔH) contributions to the free energy of adsorption($\Delta A = \Delta H - T\Delta S$) at 300 K.

6.3.5 Free Energy of Adsorption of Carbonate Ion

It would be interesting to compare the free energy of adsorption between the naphthenic acids and carbonate ions. The free energy of adsorption of a carbonate ion as a function of distance to the surface was calculated following the same procedure described previously. The results are shown in Figure 6.9. Again, two energy wells are present with the depth around -3 kcal/mol and -4 kcal/mol, respectively, which are slightly greater than or equal to that of the naphthenic acid with the longest tail studied in this work(Fig. 6.6(c)). So it will only be slightly energetically favorable for the carbonate ion to displace the naphthenic acid with moderate tail size. So, one would expect that carbonate ions may not be able to displace the naphthenic acids with bulkier tails or asphaltene molecules from the calcite surface by itself. This observation in some sense agrees with the experimental observation, which shows that divalent anion sulfates are not able to alter the wettability without the presence of Mg^{2+} and Ca^{2+} [196]. Further investigation is needed to unveil the mechanism of

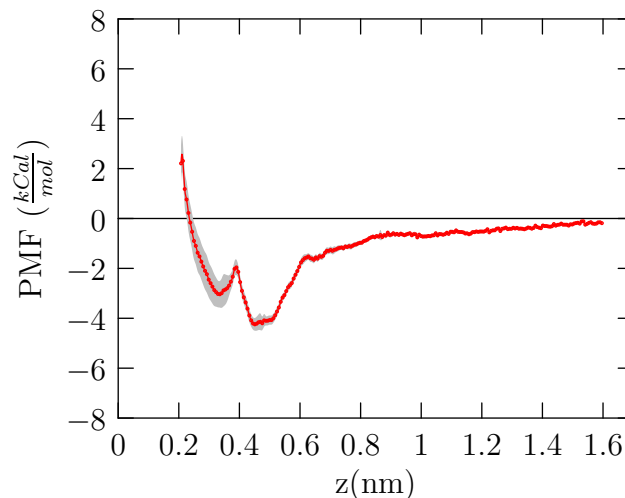


Figure 6.9 : Potnetial of mean force of the carbonate ion at 300 K. The gray shades are the statistical error estimated by using Bayesian bootstrap method.

wettability alteration and the effect of potential determining ions.

6.4 Conclusion

In this work, the adsorption free energy of deprotonated naphthenic acids on the calcite ($10\bar{1}4$) surface is studied along with that of a potential determining ion carbonate. It was shown that the adsorption of naphthenates is greatly affected by the size of the hydrophobic tails. The acid molecule that possesses longer tail adsorbs more strongly onto the calcite surface compared to shorter tail ones. Additionally, the enhancing effect of temperature on the adsorption was observed by comparing the free energy profiles, qualitatively agreeing with the experimental observation made by Young et al.[199]. These two observations suggest that hydrophobic interaction exists between deprotonated naphthenic acids and the calcite surface. The hydrophobic interaction is suspected to be related to the entropy of adsorbed water molecules. It was shown that the adsorption process is entropically driven based on the decoupled entropic

and enthalpic contributions to the free energy of adsorption.

Furthermore, we showed that the adsorption of carbonate ions can only be slightly more energetically favorable compared to the acids with moderate tail size. However, since the size of the tail can greatly affect the adsorption free energy, it can be anticipated that the carbonate ion may not be able to displace adsorbed acid molecules with bulkier tails.

Chapter 7

Concluding Remarks

In this chapter, the thesis work will be summarized. Additionally, some future research directions will be proposed.

7.1 Summary

In this thesis, molecular thermodynamic approaches such as iSAFT classical density functional theory and molecular dynamics simulation approach have been used to study the systems containing amphiphilic molecules or surfactants.

First, an iSAFT approach based on the forces acting through the interface and the Method of Moments was developed to predict the effect of surfactant architecture on the type of microemulsions formed. The stress that describes the forces in the interfacial region obtained from iSAFT was verified against molecular dynamics simulation approach, and the dependence of the types of microemulsions on surfactant architecture agrees qualitatively with experimental observation. Additionally, the effect of surfactant structure on the phase inversion temperature can also be captured. With proper determination of surfactant parameters, this new approach will potentially enable efficient screening of surfactant formulation for enhanced oil recovery process.

Second, an extension of iSAFT to model the formation of spherical surfactant aggregates(micelles) was presented. Compared with molecular simulation approach, iSAFT approach models the true thermodynamic equilibrium state between micelles

and surfactant monomers and provides an unified theoretical framework for describing the properties of complex fluid in the bulk region and also in the interfacial region. This new application of iSAFT DFT enables us to predict complete interfacial tension isotherms. Additionally, this approach can be used to study swollen micelles and inverse swollen micelles that may enable us to gain better understanding of the formation of a middle-phase microemulsion.

Third, we provided insight into the mechanism of lauryl betaine as foam booster. Using molecular dynamics simulations, a system of LB (the foam booster) and alpha olefin sulfonate (AOS-14), an anionic surfactant that is used as a foam stabilizer, was studied. It was found that the foam booster functions by screening the interaction between the anionic surfactant. Favorable interaction between foam booster and anionic surfactants leads to a closer packing of the monolayer than possible with just the pure anionic surfactant. It was also found that the closer packing is also reflected in an elevated surface dilatational modulus, indicating that the better packed monolayer will stabilize the foam. This work offers insights that can be potentially useful in rational design of surfactant blends for use in enhanced oil recovery.

In the end, the adsorption of naphthenic acids on calcite surface was studied by molecular dynamics simulation and umbrella sampling technique. It was found that both electrostatic interaction and hydrophobic interaction between acid molecules and calcite surfaces are important in the adsorption process. The adsorption free energy can be enhanced by increasing the tail size of naphthenic acids. Further, the adsorption of acids at room temperature was shown to be entropically driven and increases with the increase of temperature, which is consistent with experimental observation.

7.2 Future work

7.2.1 More Realistic Model for Surfactant

Surfactant molecules are constructed in a relatively primitive manner in this work: the same spirit as the Telo de Gama and Gubbins model[66] that the surfactants consist of water-like segments and oil-like segments was incorporated. Although some improvement has been made to the original model including explicitly considering hydrogen bonding interactions, only qualitative agreement between theoretical prediction and experimental observations has been achieved. However, a quantitative prediction is in no doubt more preferred. So more realistic parameters and model for surfactant molecules should be considered as part of the future work. A number of development has been made in our group and is worth considering for reference. For example, Marshall et al.[141] showed that the rigidity of surfactant tails can be incorporated in iSAFT by considering Wertheim's second order perturbation theory. Further, Deepti et al.[216, 140] showed that by proper fitting, iSAFT can quantitatively predict the interfacial tension isotherms of amphiphilic molecules such as alcohols and block copolymers. By developing and incorporating realistic surfactant parameters and model, iSAFT has the potential to quantitatively predict the interfacial properties of surfactants and help improve the efficiency of rational design of surfactant structure for specific applications.

7.2.2 Micelles as Drug Delivery Carriers

Owing to the similarity to natural carriers such as viruses and serum lipoproteins, the use of self-assembled block copolymer micelles in the field of drug delivery is of increasing interest to researchers and pharmaceutical industry[217]. Due to the

amphiphilic nature of block copolymers such as Pluronics, block copolymers built of poly(ethylene oxide)(PEO) and poly(propylene oxide)(PPO), etc, hydrophobic segments are expelled by the aqueous environment to form a hydrophobic core which can substantially solubilize hydrophobic drug molecules[218]. This reservoir of drug is surrounded and protected by the hydrophilic moieties. The applicability of block copolymers as drug carriers is affected by a number of properties including but not limited to water solubility of the drug-micelle complex in aqueous environment, biocompatibility or size of the micelles, micellar stability including thermodynamic stability and kinetic stability, biological half-life, morphology, drug loading or drug solubility, and release characteristics[217]. In Chapter 4, we showed that iSAFT is ready to describe a number of properties of surfactant micelles. Additionally, Kai et al.[136] showed that iSAFT is able to capture the thermoresponsive behavior of polymer brushes, which unveils the potential application of iSAFT for the design of thermo sensitive block copolymer carriers for active targeting and precise drug delivery[219].

In the future, iSAFT will be extended to study the properties of drug-micelle complexes or swollen micelles. A number of developments can be useful in improving the current iSAFT model describing micelle formation. First, iSAFT model needs to be extended to describe the micelle size distribution, which may need the calculation to be performed in higher dimension. Then, physical model parameters of the block copolymers and drug molecules need to be developed. Finally, the theory needs to be extended to model other micelle shapes such as the ellipsoid, rod-like and lamellar shape[220, 221]. After these developments, iSAFT can be used to improve the efficiency in designing polymer architecture for better and more efficient drug delivery carriers.

7.2.3 Wettability Alteration

As introduced before, the development of advanced techniques for the wettability alteration of carbonate reservoirs can greatly improve oil recovery efficiency in water-flooding processes. The wettability of rock surfaces is a function of the amount of adsorbents and properties of adsorbed organic acids. So understanding the interaction between the organic acids and the rock surface may enable better understanding of the mechanism behind wettability alteration and developing new approaches to achieve the wettability alteration. In Chapter 6, we showed the study on the adsorption of deprotonated naphthenic acids on the most stable calcite surfaces at low acid concentration and the results agree with experimental observation. The investigation on the interactions between acids and calcite surfaces at other conditions such as higher acid concentration has left to be carried out. Furthermore, a mechanism has been proposed by Zhang et al.[196] explaining the effect of potential determining ions (Ca^{2+} , Mg^{2+} and SO_4^{2-}) on the wettability alteration of chalk. It was proposed that the adsorbed acid molecules can react with Ca^{2+} at low temperature. In contrast, at higher temperature, Mg^{2+} could substitute Ca^{2+} from the surface of the mineral and replace the Ca^{2+} -acid complex. However, a verification of this proposed mechanism is still unavailable in the literature. So, in the future, this mechanism will be tested in molecular level using molecular dynamics simulation and quantum mechanics.

After thorough investigations of the interactions between acids and mineral surfaces at various conditions such as temperature, salinity, brine composition, and etc, an approach or brine formulation will be developed to effectively desorb the acid molecules from the rock surfaces and alter the wettability for improved oil recovery efficiency.

7.2.4 Solving iSAFT in Higher Dimension

In current stage, the iSAFT classical density functional theory can only be efficiently carried out in one-dimension by assuming symmetry in the other two dimensions or in two-dimension when the Fast Fourier Transform approach is incorporated[222]. Although a large range of problems can be resolved by these lower dimensional iSAFT approaches, a higher dimensional iSAFT model is still preferred when more complex systems are investigated. For example, the bicontinuous structure of a middle-phase microemulsion can only be described in 3-D and cannot be efficiently solved by current iSAFT model.

Since the free energy of the system is directly available from iSAFT, a numerical scheme that utilizes Monte Carlo sampling is promising and enables straightforward higher dimensional calculations. Additionally, the mean field approximation which ignores the pair correlation between particles can be dropped naturally in a Monte Carlo based approach. This approach has been applied by Detcheverry et al[223] to study the phase behavior of polymeric systems with free energy functional from self consistent field type theory. After incorporating this approach into iSAFT framework, the model will be capable of exploring the complex phase behavior of surfactant systems and providing insight into the structure of middle-phase microemulsions.

Bibliography

- [1] G. Torrie and J. Valleau, “Electrical double layers. i. monte carlo study of a uniformly charged surface,” *The Journal of Chemical Physics*, vol. 73, no. 11, pp. 5807–5816, 1980.
- [2] D. Boda, W. R. Fawcett, D. Henderson, and S. Sokolowski, “Monte carlo, density functional theory, and poisson–boltzmann theory study of the structure of an electrolyte near an electrode,” *The Journal of chemical physics*, vol. 116, no. 16, pp. 7170–7176, 2002.
- [3] G. Torrie and J. Valleau, “Electrical double layers. 4. limitations of the gouy–chapman theory,” *The Journal of Physical Chemistry*, vol. 86, no. 16, pp. 3251–3257, 1982.
- [4] C. N. Patra, R. Chang, and A. Yethiraj, “Structure of polyelectrolyte solutions at a charged surface,” *The Journal of Physical Chemistry B*, vol. 108, no. 26, pp. 9126–9132, 2004.
- [5] Z. Li and J. Wu, “Density functional theory for polyelectrolytes near oppositely charged surfaces,” *Physical review letters*, vol. 96, no. 4, p. 048302, 2006.
- [6] S. Zeppieri, J. Rodríguez, and A. López de Ramos, “Interfacial tension of alkane+ water systems,” *Journal of Chemical & Engineering Data*, vol. 46, no. 5, pp. 1086–1088, 2001.

- [7] C. Marche, C. Ferronato, and J. Jose, "Solubilities of n-alkanes (c6 to c8) in water from 30 c to 180 c," *Journal of Chemical & Engineering Data*, vol. 48, no. 4, pp. 967–971, 2003.
- [8] M. Velinova, D. Sengupta, A. V. Tadjer, and S.-J. Marrink, "Sphere-to-rod transitions of nonionic surfactant micelles in aqueous solution modeled by molecular dynamics simulations," *Langmuir*, vol. 27, no. 23, pp. 14071–14077, 2011.
- [9] S.-Y. Lin, Y.-Y. Lin, E.-M. Chen, C.-T. Hsu, and C.-C. Kwan, "A study of the equilibrium surface tension and the critical micelle concentration of mixed surfactant solutions," *Langmuir*, vol. 15, no. 13, pp. 4370–4376, 1999.
- [10] B. Zhmud, F. Tiberg, and J. Kizling, "Dynamic surface tension in concentrated solutions of c n e m surfactants: a comparison between the theory and experiment," *Langmuir*, vol. 16, no. 6, pp. 2557–2565, 2000.
- [11] J. N. Israelachvili, *Intermolecular and surface forces: revised third edition*. Academic press, 2011.
- [12] Y. Liu, P. G. Jessop, M. Cunningham, C. A. Eckert, and C. L. Liotta, "Switchable surfactants," *Science*, vol. 313, no. 5789, pp. 958–960, 2006.
- [13] T. Ahmadall, M. V. Gonzalez, J. H. Harwell, J. F. Scamehorn, *et al.*, "Reducing surfactant adsorption in carbonate reservoirs," *SPE reservoir engineering*, vol. 8, no. 02, pp. 117–122, 1993.
- [14] C. A. Miller and P. Neogi, *Interfacial phenomena: equilibrium and dynamic effects*, vol. 139. CRC Press, 2007.

- [15] M. Cates and S. Candau, "Statics and dynamics of worm-like surfactant micelles," *Journal of Physics: Condensed Matter*, vol. 2, no. 33, p. 6869, 1990.
- [16] K. Mortensen and J. S. Pedersen, "Structural study on the micelle formation of poly (ethylene oxide)-poly (propylene oxide)-poly (ethylene oxide) triblock copolymer in aqueous solution," *Macromolecules*, vol. 26, no. 4, pp. 805–812, 1993.
- [17] S. Hyde, "Microstructure of bicontinuous surfactant aggregates," *The Journal of Physical Chemistry*, vol. 93, no. 4, pp. 1458–1464, 1989.
- [18] J. Yang, "Viscoelastic wormlike micelles and their applications," *Current opinion in colloid & interface science*, vol. 7, no. 5, pp. 276–281, 2002.
- [19] A. Domínguez, A. Fernández, N. González, E. Iglesias, and L. Montenegro, "Determination of critical micelle concentration of some surfactants by three techniques," *J. Chem. Educ*, vol. 74, no. 10, p. 1227, 1997.
- [20] I. Danielsson and B. Lindman, "The definition of microemulsion," *Colloids and Surfaces*, vol. 3, no. 4, pp. 391–392, 1981.
- [21] P. Winsor, "Hydrotrophy, solubilisation and related emulsification processes," *Transactions of the Faraday Society*, vol. 44, pp. 376–398, 1948.
- [22] J. G. Fraaije, K. Tandon, S. Jain, J.-W. Handgraaf, and M. Buijse, "Method of moments for computational microemulsion analysis and prediction in tertiary oil recovery," *Langmuir*, vol. 29, no. 7, pp. 2136–2151, 2013.
- [23] J. N. Israelachvili, D. J. Mitchell, and B. W. Ninham, "Theory of self-assembly of hydrocarbon amphiphiles into micelles and bilayers," *Journal of the Chemi-*

- cal Society, Faraday Transactions 2: Molecular and Chemical Physics*, vol. 72, pp. 1525–1568, 1976.
- [24] W. Griffin, “Hydrophilic-lipophilic balance,” *J Soc Cosmet Chem*, vol. 1, pp. 311–326, 1949.
- [25] B. Becker, P. K. Schelling, and S. R. Phillpot, “Interfacial phonon scattering in semiconductor nanowires by molecular-dynamics simulation,” *Journal of applied physics*, vol. 99, no. 12, p. 123715, 2006.
- [26] A. Georgiadis, F. Llovel, A. Bismarck, F. J. Blas, A. Galindo, G. C. Maitland, J. M. Trusler, and G. Jackson, “Interfacial tension measurements and modelling of (carbon dioxide+n-alkane) and (carbon dioxide+ water) binary mixtures at elevated pressures and temperatures,” *The Journal of Supercritical Fluids*, vol. 55, no. 2, pp. 743–754, 2010.
- [27] W. D. Harkins and F. Brown, “The determination of surface tension (free surface energy), and the weight of falling drops: The surface tension of water and benzene by the capillary height method.,” *Journal of the American Chemical Society*, vol. 41, no. 4, pp. 499–524, 1919.
- [28] Y. Rotenberg, L. Boruvka, and A. Neumann, “Determination of surface tension and contact angle from the shapes of axisymmetric fluid interfaces,” *Journal of colloid and interface science*, vol. 93, no. 1, pp. 169–183, 1983.
- [29] J. Drelich, C. Fang, and C. White, “Measurement of interfacial tension in fluid-fluid systems,” *Encyclopedia of surface and colloid science*, vol. 3, pp. 3158–3163, 2002.

- [30] J. S. Rowlinson and B. Widom, *Molecular theory of capillarity*. Courier Corporation, 2013.
- [31] J. Rowlinson, “Translation of jd van der waals’the thermodynamik theory of capillarity under the hypothesis of a continuous variation of density,” *Journal of Statistical Physics*, vol. 20, no. 2, pp. 197–200, 1979.
- [32] J. W. Cahn and J. E. Hilliard, “Free energy of a nonuniform system. i. interfacial free energy,” *The Journal of chemical physics*, vol. 28, no. 2, pp. 258–267, 1958.
- [33] S. Werth, M. Kohns, K. Langenbach, M. Heilig, M. Horsch, and H. Hasse, “Interfacial and bulk properties of vapor-liquid equilibria in the system toluene+ hydrogen chloride+ carbon dioxide by molecular simulation and density gradient theory+ pc-saft,” *Fluid Phase Equilibria*, vol. 427, pp. 219–230, 2016.
- [34] S. Enders and H. Kahl, “Interfacial properties of water+ alcohol mixtures,” *Fluid Phase Equilibria*, vol. 263, no. 2, pp. 160–167, 2008.
- [35] P. Cornelisse, C. Peters, and J. de Swaan Arons, “Application of the peng-robinson equation of state to calculate interfacial tensions and profiles at vapour-liquid interfaces,” *Fluid Phase Equilibria*, vol. 82, pp. 119–129, 1993.
- [36] B. D. Marshall, K. R. Cox, and W. G. Chapman, “A classical density functional theory study of the neat n-alkane/water interface,” *The Journal of Physical Chemistry C*, vol. 116, no. 33, pp. 17641–17649, 2012.
- [37] J. Gross, “A density functional theory for vapor-liquid interfaces using the pc-p-saft equation of state,” *The Journal of chemical physics*, vol. 131, no. 20, p. 204705, 2009.

- [38] K. Liu, "Phase separation of lennard-jones systems: A film in equilibrium with vapor," *The Journal of Chemical Physics*, vol. 60, no. 11, pp. 4226–4230, 1974.
- [39] M. Rao and B. Berne, "On the location of surface of tension in the planar interface between liquid and vapour," *Molecular Physics*, vol. 37, no. 2, pp. 455–461, 1979.
- [40] M. Rao and D. Levesque, "Surface structure of a liquid film," *The Journal of Chemical Physics*, vol. 65, no. 8, pp. 3233–3236, 1976.
- [41] G. A. Chapela, G. Saville, S. M. Thompson, and J. S. Rowlinson, "Computer simulation of a gas–liquid surface. part 1," *Journal of the Chemical Society, Faraday Transactions 2: Molecular and Chemical Physics*, vol. 73, no. 7, pp. 1133–1144, 1977.
- [42] G. J. Gloor, G. Jackson, F. J. Blas, and E. de Miguel, "Test-area simulation method for the direct determination of the interfacial tension of systems with continuous or discontinuous potentials," *The Journal of chemical physics*, vol. 123, no. 13, p. 134703, 2005.
- [43] S. Pronk, S. Páll, R. Schulz, P. Larsson, P. Bjelkmar, R. Apostolov, M. R. Shirts, J. C. Smith, P. M. Kasson, D. van der Spoel, *et al.*, "Gromacs 4.5: a high-throughput and highly parallel open source molecular simulation toolkit," *Bioinformatics*, p. btt055, 2013.
- [44] D. A. Case, T. E. Cheatham, T. Darden, H. Gohlke, R. Luo, K. M. Merz, A. Onufriev, C. Simmerling, B. Wang, and R. J. Woods, "The amber biomolecular simulation programs," *Journal of computational chemistry*, vol. 26, no. 16, pp. 1668–1688, 2005.

- [45] J. C. Phillips, R. Braun, W. Wang, J. Gumbart, E. Tajkhorshid, E. Villa, C. Chipot, R. D. Skeel, L. Kale, and K. Schulten, “Scalable molecular dynamics with namd,” *Journal of computational chemistry*, vol. 26, no. 16, pp. 1781–1802, 2005.
- [46] B. R. Brooks, R. E. Bruccoleri, and B. D. Olafson, “States, dj; swaminathan, s.; karplus, m,” *J. comput. Chem*, vol. 4, no. 2, pp. 187–217, 1983.
- [47] M. G. Martin, “Mcccs towhee: a tool for monte carlo molecular simulation,” *Molecular Simulation*, vol. 39, no. 14-15, pp. 1212–1222, 2013.
- [48] W. L. Jorgensen, D. S. Maxwell, and J. Tirado-Rives, “Development and testing of the opls all-atom force field on conformational energetics and properties of organic liquids,” *Journal of the American Chemical Society*, vol. 118, no. 45, pp. 11225–11236, 1996.
- [49] J. Wang, R. M. Wolf, J. W. Caldwell, P. A. Kollman, and D. A. Case, “Development and testing of a general amber force field,” *Journal of computational chemistry*, vol. 25, no. 9, pp. 1157–1174, 2004.
- [50] J. Alejandre, D. J. Tildesley, and G. A. Chapela, “Molecular dynamics simulation of the orthobaric densities and surface tension of water,” *The Journal of chemical physics*, vol. 102, no. 11, pp. 4574–4583, 1995.
- [51] A. R. van Buuren, S. J. Marrink, and H. J. Berendsen, “A molecular dynamics study of the decane/water interface,” *The Journal of Physical Chemistry*, vol. 97, no. 36, pp. 9206–9212, 1993.
- [52] L. W. Lake, R. Johns, W. Rossen, and G. Pope, *Fundamentals of enhanced oil recovery*. Society of Petroleum Engineers, 2014.

- [53] A. Wilson, *Experimental techniques for the characterization of foams*. Marcel Dekker: New York, NY, USA, 1995.
- [54] G. J. Hirasaki, C. A. Miller, M. Puerto, *et al.*, “Recent advances in surfactant eor,” in *SPE Annual Technical Conference and Exhibition*, Society of Petroleum Engineers, 2008.
- [55] E. Mayer, R. Berg, J. Carmichael, R. Weinbrandt, *et al.*, “Alkaline injection for enhanced oil recovery—a status report,” *Journal of Petroleum Technology*, vol. 35, no. 01, pp. 209–221, 1983.
- [56] R. B. Needham, P. H. Doe, *et al.*, “Polymer flooding review,” *Journal of Petroleum Technology*, vol. 39, no. 12, pp. 1–503, 1987.
- [57] S. Liu, *Alkaline Surfactant Polymer enhanced oil recovery process*. PhD thesis, Rice University, 2008.
- [58] R. Nelson, J. Lawson, D. Thigpen, G. Stegemeier, *et al.*, “Cosurfactant-enhanced alkaline flooding,” in *SPE Enhanced Oil Recovery Symposium*, Society of Petroleum Engineers, 1984.
- [59] D. Levitt, G. A. Pope, *et al.*, “Selection and screening of polymers for enhanced-oil recovery,” in *SPE Symposium on Improved Oil Recovery*, Society of Petroleum Engineers, 2008.
- [60] R. F. Li, W. Yan, S. Liu, G. Hirasaki, C. A. Miller, *et al.*, “Foam mobility control for surfactant enhanced oil recovery,” *SPE Journal*, vol. 15, no. 04, pp. 928–942, 2010.

- [61] L. E. Zerpa, N. V. Queipo, S. Pintos, and J.-L. Salager, “An optimization methodology of alkaline–surfactant–polymer flooding processes using field scale numerical simulation and multiple surrogates,” *Journal of Petroleum Science and Engineering*, vol. 47, no. 3, pp. 197–208, 2005.
- [62] F. M. Orr, *Theory of gas injection processes*. Tie-Line Publications, 2007.
- [63] W. G. Chapman, K. E. Gubbins, G. Jackson, and M. Radosz, “New reference equation of state for associating liquids,” *Industrial & Engineering Chemistry Research*, vol. 29, no. 8, pp. 1709–1721, 1990.
- [64] C. J. Segura and W. G. Chapman, “Associating fluids with four bonding sites against solid surfaces: Monte carlo simulations,” *Molecular Physics*, vol. 86, no. 3, pp. 415–442, 1995.
- [65] S. Tripathi and W. G. Chapman, “Density-functional theory for polar fluids at functionalized surfaces. i. fluid-wall association,” *The Journal of chemical physics*, vol. 119, no. 23, pp. 12611–12620, 2003.
- [66] M. Telo da Gama and K. Gubbins, “Adsorption and orientation of amphiphilic molecules at a liquid-liquid interface,” *Molecular Physics*, vol. 59, no. 2, pp. 227–239, 1986.
- [67] S. Jain, A. Dominik, and W. G. Chapman, “Modified interfacial statistical associating fluid theory: A perturbation density functional theory for inhomogeneous complex fluids,” *The Journal of chemical physics*, vol. 127, no. 24, p. 244904, 2007.
- [68] A. Bymaster and W. G. Chapman, “An i saft density functional theory for associating polyatomic molecules,” *The Journal of Physical Chemistry B*, vol. 114,

- no. 38, pp. 12298–12307, 2010.
- [69] D. McQuarrie, *Statistical Mechanics*. University Science Books, 2000.
- [70] Y. Rosenfeld, “Free-energy model for the inhomogeneous hard-sphere fluid mixture and density-functional theory of freezing,” *Physical review letters*, vol. 63, no. 9, p. 980, 1989.
- [71] J.-P. Hansen and I. R. McDonald, *Theory of simple liquids*. Elsevier, 1990.
- [72] M. Wertheim, “Fluids with highly directional attractive forces. i. statistical thermodynamics,” *Journal of statistical physics*, vol. 35, no. 1-2, pp. 19–34, 1984.
- [73] M. Wertheim, “Fluids with highly directional attractive forces. ii. thermodynamic perturbation theory and integral equations,” *Journal of statistical physics*, vol. 35, no. 1-2, pp. 35–47, 1984.
- [74] M. Wertheim, “Fluids with highly directional attractive forces. iii. multiple attraction sites,” *Journal of statistical physics*, vol. 42, no. 3-4, pp. 459–476, 1986.
- [75] M. Wertheim, “Fluids with highly directional attractive forces. iv. equilibrium polymerization,” *Journal of statistical physics*, vol. 42, no. 3-4, pp. 477–492, 1986.
- [76] B. C. J. SEGURA, W. G. C. SHUKLA, and K. P., “Associating fluids with four bonding sites against a hard wall: density functional theory,” *Molecular Physics*, vol. 90, no. 5, pp. 759–772, 1997.

- [77] W. G. Chapman, G. Jackson, and K. E. Gubbins, "Phase equilibria of associating fluids: chain molecules with multiple bonding sites," *Molecular Physics*, vol. 65, no. 5, pp. 1057–1079, 1988.
- [78] S. Tripathi and W. G. Chapman, "Microstructure of inhomogeneous polyatomic mixtures from a density functional formalism for atomic mixtures," *The Journal of chemical physics*, vol. 122, no. 9, p. 094506, 2005.
- [79] L. J. D. Frink and A. L. Frischknecht, "Density functional theory approach for coarse-grained lipid bilayers," *Physical Review E*, vol. 72, no. 4, p. 041923, 2005.
- [80] J. Wu, T. Jiang, D.-e. Jiang, Z. Jin, and D. Henderson, "A classical density functional theory for interfacial layering of ionic liquids," *Soft Matter*, vol. 7, no. 23, pp. 11222–11231, 2011.
- [81] D. Henderson, S. Lamperski, Z. Jin, and J. Wu, "Density functional study of the electric double layer formed by a high density electrolyte," *The Journal of Physical Chemistry B*, vol. 115, no. 44, pp. 12911–12914, 2011.
- [82] A. Oleksy and J.-P. Hansen, "Towards a microscopic theory of wetting by ionic solutions. i. surface properties of the semi-primitive model," *Molecular Physics*, vol. 104, no. 18, pp. 2871–2883, 2006.
- [83] L. Blum, "Mean spherical model for asymmetric electrolytes: I. method of solution," *Molecular Physics*, vol. 30, no. 5, pp. 1529–1535, 1975.
- [84] K. Hiroike, "Supplement to blum's theory for asymmetric electrolytes," *Molecular Physics*, vol. 33, no. 4, pp. 1195–1198, 1977.

- [85] L. Wang, P. Venkataraman, G. J. Hirasaki, C. A. Miller, and W. G. Chapman, “Effect of surfactant architecture and surface stress profile on oil / water interfacial tension from isoft molecular density functional theory,” in *The 2014 Annual Meeting*, 2014.
- [86] E. Tzimas, A. Georgakaki, C. G. Cortes, and S. Peteves, “Enhanced oil recovery using carbon dioxide in the european energy system,” *Report EUR*, vol. 21895, no. 6, 2005.
- [87] R. Aveyard, B. P. Binks, S. Clark, and J. Mead, “Interfacial tension minima in oil–water–surfactant systems. behaviour of alkane–aqueous nacl systems containing aerosol ot,” *Journal of the Chemical Society, Faraday Transactions 1: Physical Chemistry in Condensed Phases*, vol. 82, no. 1, pp. 125–142, 1986.
- [88] K. Holmberg, B. Jönsson, B. Kronberg, and B. Lindman, *Surfactants and polymers in aqueous solution*. Wiley, 2003.
- [89] J.-L. Salager, A. M. Forgiarini, and J. Bullón, “How to attain ultralow interfacial tension and three-phase behavior with surfactant formulation for enhanced oil recovery: a review. part 1. optimum formulation for simple surfactant–oil–water ternary systems,” *Journal of Surfactants and Detergents*, vol. 16, no. 4, pp. 449–472, 2013.
- [90] A. H.-L. Balance and A. S. E. D. Cases, “Formulation concepts for the emulsion maker,” 2000.
- [91] W. Helfrich, “Elastic properties of lipid bilayers: theory and possible experiments,” *Zeitschrift für Naturforschung C*, vol. 28, no. 11-12, pp. 693–703, 1973.

- [92] C. L. Murphy, *Thermodynamics of low tension and highly curved interfaces*. PhD thesis, University of Minnesota, 1966.
- [93] J. Bowcott and J. H. Schulman, “Emulsions control of droplet size and phase continuity in transparent oil-water dispersions stabilized with soap and alcohol,” *Berichte der Bunsengesellschaft für physikalische Chemie*, vol. 59, no. 4, pp. 283–290, 1955.
- [94] R. S. Cantor, “The lateral pressure profile in membranes: a physical mechanism of general anesthesia,” *Biochemistry*, vol. 36, no. 9, pp. 2339–2344, 1997.
- [95] R. S. Cantor, “Lipid composition and the lateral pressure profile in bilayers,” *Biophysical journal*, vol. 76, no. 5, pp. 2625–2639, 1999.
- [96] R. Aveyard, J. H. Clint, D. Nees, and N. Quirke, “Structure and collapse of particle monolayers under lateral pressure at the octane/aqueous surfactant solution interface,” *Langmuir*, vol. 16, no. 23, pp. 8820–8828, 2000.
- [97] Y. Long, J. C. Palmer, B. Coasne, M. Śliwiska-Bartkowiak, G. Jackson, E. A. Müller, and K. E. Gubbins, “On the molecular origin of high-pressure effects in nanoconfinement: The role of surface chemistry and roughness,” *The Journal of chemical physics*, vol. 139, no. 14, p. 144701, 2013.
- [98] C. Miller and P. Neogi, “Thermodynamics of microemulsions: combined effects of dispersion entropy of drops and bending energy of surfactant films,” *AICHE Journal*, vol. 26, no. 2, pp. 212–220, 1980.
- [99] J. Irving and J. G. Kirkwood, “The statistical mechanical theory of transport processes. iv. the equations of hydrodynamics,” *The Journal of chemical physics*, vol. 18, no. 6, pp. 817–829, 1950.

- [100] L. Makkonen, “Surface melting of ice,” *The Journal of Physical Chemistry B*, vol. 101, no. 32, pp. 6196–6200, 1997.
- [101] H. J. Berendsen, D. van der Spoel, and R. van Drunen, “Gromacs: A message-passing parallel molecular dynamics implementation,” *Computer Physics Communications*, vol. 91, no. 1, pp. 43–56, 1995.
- [102] J. M. Vanegas, A. Torres-Sánchez, and M. Arroyo, “Importance of force decomposition for local stress calculations in biomembrane molecular simulations,” *Journal of chemical theory and computation*, vol. 10, no. 2, pp. 691–702, 2014.
- [103] L. Rekvig, M. Kranenburg, J. Vreede, B. Hafskjold, and B. Smit, “Investigation of surfactant efficiency using dissipative particle dynamics,” *Langmuir*, vol. 19, no. 20, pp. 8195–8205, 2003.
- [104] K. Urita, Y. Shiga, T. Fujimori, T. Iiyama, Y. Hattori, H. Kanoh, T. Ohba, H. Tanaka, M. Yudasaka, S. Iijima, *et al.*, “Confinement in carbon nanospace-induced production of ki nanocrystals of high-pressure phase,” *Journal of the American Chemical Society*, vol. 133, no. 27, pp. 10344–10347, 2011.
- [105] E. Kumacheva and J. Klein, “Simple liquids confined to molecularly thin layers. ii. shear and frictional behavior of solidified films,” *The Journal of chemical physics*, vol. 108, no. 16, pp. 7010–7022, 1998.
- [106] J. Klein and E. Kumacheva, “Simple liquids confined to molecularly thin layers. i. confinement-induced liquid-to-solid phase transitions,” *The Journal of chemical physics*, vol. 108, no. 16, pp. 6996–7009, 1998.
- [107] J. Klein and E. Kumacheva, “Confinement-induced phase transitions in simple liquids,” *Science*, vol. 269, no. 5225, p. 816, 1995.

- [108] K. Kaneko, N. Fukuzaki, K. Kakei, T. Suzuki, and S. Ozeki, "Enhancement of nitric oxide dimerization by micropore fields of activated carbon fibers," *Langmuir*, vol. 5, no. 4, pp. 960–965, 1989.
- [109] H.-W. Hu, G. A. Carson, and S. Granick, "Relaxation time of confined liquids under shear," *Physical review letters*, vol. 66, no. 21, p. 2758, 1991.
- [110] O. Byl, P. Kondratyuk, and J. Yates, "Adsorption and dimerization of no inside single-walled carbon nanotubes an infrared spectroscopic study," *The Journal of Physical Chemistry B*, vol. 107, no. 18, pp. 4277–4279, 2003.
- [111] P. A. Winsor, *Solvent properties of amphiphilic compounds*. Butterworths Scientific Publications, 1954.
- [112] W. Helfrich, "Amphiphilic mesophases made of defects," *Physics of defects*, pp. 716–55, 1981.
- [113] W. M. Gelbart, A. Ben-Shaul, and D. Roux, *Micelles, membranes, microemulsions, and monolayers*. Springer Science & Business Media, 2012.
- [114] K. Shinoda and H. Saito, "The stability of o/w type emulsions as functions of temperature and the hlb of emulsifiers: the emulsification by pit-method," *Journal of Colloid and Interface Science*, vol. 30, no. 2, pp. 258–263, 1969.
- [115] H. Saito and K. Shinoda, "The stability of w/o type emulsions as a function of temperature and of the hydrophilic chain length of the emulsifier," *Journal of Colloid and Interface Science*, vol. 32, no. 4, pp. 647–651, 1970.
- [116] W. Griffin, "Soc. cosmet. chem. 1949, 12, 311; 1954,"

- [117] H. Kunieda and K. Shinoda, "Solution behavior and hydrophile-lipophile balance temperature in the aerosol ot-isooctane-brine system: Correlation between microemulsions and ultralow interfacial tensions," *Journal of Colloid and Interface Science*, vol. 75, no. 2, pp. 601–606, 1980.
- [118] S. Chen, D. F. Evans, and B. Ninham, "Properties and structure of three-component ionic microemulsions," *The Journal of Physical Chemistry*, vol. 88, no. 8, pp. 1631–1634, 1984.
- [119] M. Kahlweit, R. Strey, and G. Busse, "Microemulsions: a qualitative thermodynamic approach," *Journal of Physical Chemistry*, vol. 94, no. 10, pp. 3881–3894, 1990.
- [120] C. P. Emborsky, K. R. Cox, and W. G. Chapman, "Exploring parameter space effects on structure-property relationships of surfactants at liquid-liquid interfaces," *The Journal of chemical physics*, vol. 135, no. 8, p. 084708, 2011.
- [121] K. Klopfer and T. Vanderlick, "Amphiphiles at oil-water interfaces: simulation study of their tension-reducing properties," *Colloids and Surfaces A: Physicochemical and Engineering Aspects*, vol. 96, no. 1, pp. 171–179, 1995.
- [122] N. Van Os, L. Rupert, B. Smit, P. Hilbers, K. Esselink, M. Böhmer, and L. Koopal, "Surfactant adsorption at liquid/liquid interfaces comparison of experimental results with self-consistent field lattice calculations and molecular dynamics simulations," *Colloids and Surfaces A: Physicochemical and Engineering Aspects*, vol. 81, pp. 217–229, 1993.
- [123] J. Israelachvili, "The science and applications of emulsionsan overview," *Colloids and Surfaces A: Physicochemical and engineering aspects*, vol. 91, pp. 1–8,

1994.

- [124] S. Jain, *Molecular modeling of microstructure and thermodynamics of bulk and inhomogeneous polymer systems*. PhD thesis, Rice University, 2009.
- [125] S. H. Im, Y. H. Jeong, and J. J. Ryoo, “Simultaneous analysis of anionic, amphoteric, nonionic and cationic surfactant mixtures in shampoo and hair conditioner by rp-hplc/elsd and lc/ms,” *Analytica chimica acta*, vol. 619, no. 1, pp. 129–136, 2008.
- [126] R. D. Groot and P. B. Warren, “Dissipative particle dynamics: Bridging the gap between atomistic and mesoscopic simulation,” *Journal of Chemical Physics*, vol. 107, no. 11, p. 4423, 1997.
- [127] A. L. Frischknecht and L. J. D. Frink, “Comparison of density functional theory and simulation of fluid bilayers,” *Physical Review E*, vol. 72, no. 4, p. 041924, 2005.
- [128] H. Klevens, “Structure and aggregation in dilute solution of surface active agents,” *Journal of the American Oil Chemists Society*, vol. 30, no. 2, pp. 74–80, 1953.
- [129] E. C. Voutsas, M. V. Flores, N. Spiliotis, G. Bell, P. J. Halling, and D. P. Tassios, “Prediction of critical micelle concentrations of nonionic surfactants in aqueous and nonaqueous solvents with unifac,” *Industrial & engineering chemistry research*, vol. 40, no. 10, pp. 2362–2366, 2001.
- [130] X.-S. Li, J.-F. Lu, Y.-G. Li, and J.-C. Liu, “Studies on unique and soft equations for nonionic surfactant solutions,” *Fluid phase equilibria*, vol. 153, no. 2, pp. 215–229, 1998.

- [131] Y. Moroi, “Mass action model of micelle formation: its application to sodium dodecyl sulfate solution,” *Journal of colloid and interface science*, vol. 122, no. 2, pp. 308–314, 1988.
- [132] C. Lian, L. Wang, X. Chen, X. Han, S. Zhao, H. Liu, and Y. Hu, “Modeling swelling behavior of thermoresponsive polymer brush with lattice density functional theory,” *Langmuir*, vol. 30, no. 14, pp. 4040–4048, 2014.
- [133] C. Lian, X. Chen, S. Zhao, W. Lv, X. Han, H. Wang, and H. Liu, “Substrate effect on the phase behavior of polymer brushes with lattice density functional theory,” *Macromolecular Theory and Simulations*, vol. 23, no. 9, pp. 575–582, 2014.
- [134] K. Gong and W. G. Chapman, “Solvent response of mixed polymer brushes,” *The Journal of chemical physics*, vol. 135, no. 21, p. 214901, 2011.
- [135] K. Gong, B. D. Marshall, and W. G. Chapman, “Response behavior of diblock copolymer brushes in explicit solvent,” *The Journal of chemical physics*, vol. 137, no. 15, p. 154904, 2012.
- [136] K. Gong, B. D. Marshall, and W. G. Chapman, “Modeling lower critical solution temperature behavior of associating polymer brushes with classical density functional theory,” *The Journal of chemical physics*, vol. 139, no. 9, p. 094904, 2013.
- [137] Z. Feng and W. G. Chapman, “Revisited block copolymer/nanoparticle composites: Extension of interfacial statistical associating fluid theory,” *Macromolecules*, vol. 45, no. 16, pp. 6658–6668, 2012.

- [138] D. Cao and J. Wu, "Microstructure of block copolymers near selective surfaces: theoretical predictions and configurational-bias monte carlo simulation," *Macromolecules*, vol. 38, no. 3, pp. 971–978, 2005.
- [139] D. Cao and J. Wu, "Surface-induced phase transitions in ultrathin films of block copolymers," *The Journal of chemical physics*, vol. 122, no. 19, p. 194703, 2005.
- [140] D. Ballal and W. G. Chapman, "Hydrophobic and hydrophilic interactions in aqueous mixtures of alcohols at a hydrophobic surface," *The Journal of chemical physics*, vol. 139, no. 11, p. 114706, 2013.
- [141] B. D. Marshall, C. Emborsky, K. Cox, and W. G. Chapman, "Effect of bond rigidity and molecular structure on the self-assembly of amphiphilic molecules using second-order classical density functional theory," *The Journal of Physical Chemistry B*, vol. 116, no. 9, pp. 2730–2738, 2012.
- [142] P. C. Hiemenz and R. Rajagopalan, *Principles of Colloid and Surface Chemistry, revised and expanded*, vol. 14. CRC press, 1997.
- [143] L. Huynh, C. Neale, R. Pomès, and C. Allen, "Systematic design of unimolecular star copolymer micelles using molecular dynamics simulations," *Soft Matter*, vol. 6, no. 21, pp. 5491–5501, 2010.
- [144] J. Hayter and M. Zulauf, "Attractive interactions in critical scattering from non-ionic micelles," *Colloid and Polymer Science*, vol. 260, no. 11, pp. 1023–1028, 1982.
- [145] O. Glatter, G. Fritz, H. Lindner, J. Brunner-Popela, R. Mittelbach, R. Strey, and S. U. Egelhaaf, "Nonionic micelles near the critical point: micellar growth and attractive interaction," *Langmuir*, vol. 16, no. 23, pp. 8692–8701, 2000.

- [146] L.-J. Chen, S.-Y. Lin, C.-C. Huang, and E.-M. Chen, "Temperature dependence of critical micelle concentration of polyoxyethylenated non-ionic surfactants," *Colloids and Surfaces A: Physicochemical and Engineering Aspects*, vol. 135, no. 1, pp. 175–181, 1998.
- [147] K. Meguro, Y. Takasawa, N. Kawahashi, Y. Tabata, and M. Ueno, "Micellar properties of a series of octaethyleneglycol-n-alkyl ethers with homogeneous ethylene oxide chain and their temperature dependence," *Journal of Colloid and Interface Science*, vol. 83, no. 1, pp. 50–56, 1981.
- [148] W. Brown, Z. Pu, and R. Rymden, "Size and shape of nonionic amphiphile micelles: Nmr self-diffusion and static and quasi-elastic light-scattering measurements on c12e5, c12e7, and c12e8 in aqueous solution," *The Journal of Physical Chemistry*, vol. 92, no. 21, pp. 6086–6094, 1988.
- [149] R. Alargova, I. Kochijashky, M. Sierra, and R. Zana, "Micelle aggregation numbers of surfactants in aqueous solutions: a comparison between the results from steady-state and time-resolved fluorescence quenching," *Langmuir*, vol. 14, no. 19, pp. 5412–5418, 1998.
- [150] R. Nagarajan, "Molecular packing parameter and surfactant self-assembly: the neglected role of the surfactant tail," *Langmuir*, vol. 18, no. 1, pp. 31–38, 2002.
- [151] J. Traube, "Ueber die capillaritätsconstanten organischer stoffe in wässrigen lösungen," *Justus Liebigs Annalen der Chemie*, vol. 265, no. 1, pp. 27–55, 1891.
- [152] W. Kunz, F. Testard, and T. Zemb, "Correspondence between curvature, packing parameter, and hydrophilic-lipophilic deviation scales around the phase-inversion temperature," *Langmuir*, vol. 25, no. 1, pp. 112–115, 2008.

- [153] J. L. Shelton, L. Yarborough, *et al.*, “Multiple phase behavior in porous media during co₂ or rich-gas flooding,” *Journal of Petroleum Technology*, vol. 29, no. 09, pp. 1–171, 1977.
- [154] R. Farajzadeh, A. Andrianov, R. Krastev, G. Hirasaki, and W. Rossen, “Foamoil interaction in porous media: Implications for foam assisted enhanced oil recovery,” *Advances in Colloid and Interface Science*, vol. 183184, pp. 1 – 13, 2012.
- [155] T. Zhu, D. Ogbe, and S. Khataniar, “Improving the foam performance for mobility control and improved sweep efficiency in gas flooding,” *Industrial & engineering chemistry research*, vol. 43, no. 15, pp. 4413–4421, 2004.
- [156] D. Wasan, A. Nikolov, D. Huang, D. Edwards, and D. Smith, “Surfactant based mobility control,” in *ACS Symposium Series*, vol. 373, p. 136, 1988.
- [157] K. Koczko, L. Lobo, and D. Wasan, “Effect of oil on foam stability: aqueous foams stabilized by emulsions,” *Journal of colloid and interface science*, vol. 150, no. 2, pp. 492–506, 1992.
- [158] C. Stubenrauch and R. von Klitzing, “Disjoining pressure in thin liquid foam and emulsion films — new concepts and perspectives,” *J. Phys. Condens. Matter*, vol. 15, pp. R1197–R1232, 2003.
- [159] K. G. Kornev, A. V. Neimark, and A. N. Rozhkov, “Foam in porous media: thermodynamic and hydrodynamic peculiarities,” *Advances in colloid and interface science*, vol. 82, no. 1, pp. 127–187, 1999.
- [160] R. F. Li, G. Hirasaki, C. A. Miller, S. K. Masalmeh, *et al.*, “Wettability alteration and foam mobility control in a layered, 2d heterogeneous sandpack,” *SPE*

- Journal*, vol. 17, no. 04, pp. 1–207, 2012.
- [161] E. S. Basheva, D. Ganchev, N. D. Denkov, K. Kasuga, N. Satoh, and K. Tsujii, “Role of betaine as foam booster in the presence of silicone oil drops,” *Langmuir*, vol. 16, no. 3, pp. 1000–1013, 2000.
- [162] H. Zhang, C. A. Miller, P. R. Garrett, and K. H. Raney, “Lauryl alcohol and amine oxide as foam stabilizers in the presence of hardness and oily soil,” *Journal of surfactants and detergents*, vol. 8, no. 1, pp. 99–107, 2005.
- [163] D. Shah, N. Djabbarah, and D. Wasan, “A correlation of foam stability with surface shear viscosity and area per molecule in mixed surfactant systems,” *Colloid and Polymer Science*, vol. 256, no. 10, pp. 1002–1008, 1978.
- [164] M. Frisch, G. Trucks, H. Schlegel, G. Scuseria, M. Robb, J. Cheeseman, G. Scalmani, V. Barone, B. Mennucci, G. Petersson, *et al.*, “09, revision d. 01, gaussian,” *Inc., Wallingford, CT*, 2009.
- [165] F.-Y. Dupradeau, A. Pigache, T. Zaffran, C. Savineau, R. Lelong, N. Grivel, D. Lelong, W. Rosanski, and P. Cieplak, “The red. tools: Advances in resp and esp charge derivation and force field library building,” *Physical Chemistry Chemical Physics*, vol. 12, no. 28, pp. 7821–7839, 2010.
- [166] S. J. Weiner, P. A. Kollman, D. A. Case, U. C. Singh, C. Ghio, G. Alagona, S. Profeta, and P. Weiner, “A new force field for molecular mechanical simulation of nucleic acids and proteins,” *Journal of the American Chemical Society*, vol. 106, no. 3, pp. 765–784, 1984.
- [167] J. L. Abascal and C. Vega, “A general purpose model for the condensed phases

- of water: Tip4p/2005,” *The Journal of chemical physics*, vol. 123, no. 23, p. 234505, 2005.
- [168] G. Bussi, D. Donadio, and M. Parrinello, “Canonical sampling through velocity rescaling,” *The Journal of chemical physics*, vol. 126, no. 1, p. 014101, 2007.
- [169] M. Parrinello and A. Rahman, “Polymorphic transitions in single crystals: A new molecular dynamics method,” *Journal of Applied physics*, vol. 52, no. 12, pp. 7182–7190, 1981.
- [170] S. Baoukina, L. Monticelli, M. Amrein, and D. P. Tieleman, “The molecular mechanism of monolayer-bilayer transformations of lung surfactant from molecular dynamics simulations,” *Biophysical journal*, vol. 93, no. 11, pp. 3775–3782, 2007.
- [171] E. Boek, W. Den Otter, W. Briels, and D. Iakovlev, “Molecular-dynamics simulation of amphiphilic bilayer membranes and wormlike micelles: a multi-scale modelling approach to the design of viscoelastic surfactant solutions,” *PHILOSOPHICAL TRANSACTIONS-ROYAL SOCIETY OF LONDON SERIES A MATHEMATICAL PHYSICAL AND ENGINEERING SCIENCES*, vol. 362, pp. 1625–1638, 2004.
- [172] C. Kandt, W. L. Ash, and D. P. Tieleman, “Setting up and running molecular dynamics simulations of membrane proteins,” *Methods*, vol. 41, no. 4, pp. 475–488, 2007.
- [173] A. Muthuswamy, *Foam Rheology of Zwitterionic and Anionic Surfactant Blends in Porous Media*. PhD thesis, Rice University, 2015.

- [174] B. Liu, M. I. Hoopes, and M. Karttunen, “Molecular dynamics simulations of dppc/ctab monolayers at the air/water interface,” *The Journal of Physical Chemistry B*, vol. 118, no. 40, pp. 11723–11737, 2014.
- [175] R. Hockney, S. Goel, and J. Eastwood, “Quiet high-resolution computer models of a plasma,” *Journal of Computational Physics*, vol. 14, no. 2, pp. 148–158, 1974.
- [176] S. Miyamoto and P. A. Kollman, “Settle: an analytical version of the shake and rattle algorithm for rigid water models,” *Journal of computational chemistry*, vol. 13, no. 8, pp. 952–962, 1992.
- [177] B. Hess, H. Bekker, H. J. Berendsen, J. G. Fraaije, *et al.*, “Lincs: a linear constraint solver for molecular simulations,” *Journal of computational chemistry*, vol. 18, no. 12, pp. 1463–1472, 1997.
- [178] J. M. Martínez and L. Martínez, “Packing optimization for automated generation of complex system’s initial configurations for molecular dynamics and docking,” *Journal of computational chemistry*, vol. 24, no. 7, pp. 819–825, 2003.
- [179] L. Martínez, R. Andrade, E. G. Birgin, and J. M. Martínez, “Packmol: a package for building initial configurations for molecular dynamics simulations,” *Journal of computational chemistry*, vol. 30, no. 13, pp. 2157–2164, 2009.
- [180] P. Wydro and M. Paluch, “A study of the interaction of dodecyl sulfobetaine with cationic and anionic surfactant in mixed micelles and monolayers at the air/water interface,” *Journal of colloid and interface science*, vol. 286, no. 1, pp. 387–391, 2005.

- [181] Y. Zeng, A. Muthuswamy, K. Ma, L. Wang, R. Farajzadeh, M. Puerto, S. Vincent-Bonnieu, A. A. Eftekhari, Y. Wang, C. Da, and et al., “Insights on foam transport from a texture-implicit local-equilibrium model with an improved parameter estimation algorithm,” *Ind. Eng. Chem. Res.*, vol. 55, pp. 7819–7829, 2016.
- [182] E. H. Lucassen-Reynders, *Anionic surfactants: Physical chemistry of surfactant action*, vol. 11. Marcel Dekker, 1981.
- [183] H. Fruhner, K.-D. Wantke, and K. Lunkenheimer, “Relationship between surface dilational properties and foam stability,” *Colloids and Surfaces A: Physicochemical and Engineering Aspects*, vol. 162, no. 1, pp. 193–202, 2000.
- [184] A. Dan, G. Gochev, and R. Miller, “Tensiometry and dilational rheology of mixed β -lactoglobulin/ionic surfactant adsorption layers at water/air and water/hexane interfaces,” *Journal of Colloid and Interface Science*, vol. 449, pp. 383–391, 2015.
- [185] J. G. Kirkwood and F. P. Buff, “The statistical mechanical theory of surface tension,” *The Journal of Chemical Physics*, vol. 17, no. 3, pp. 338–343, 1949.
- [186] D. D. Huang, A. Nikolov, and D. T. Wasan, “Foams: basic properties with application to porous media,” *Langmuir*, vol. 2, pp. 672–677, 1986.
- [187] Y. Wang, X. Liu, T. Jiao, and J. Niu, “Performance comparison between internal olefin sulfonates and alpha olefin sulfonates,” *Journal of Surfactants and Detergents*, vol. 20, no. 1, pp. 183–191, 2017.
- [188] J. K. Borchardt, A. R. Stryker, *et al.*, “Olefin sulfonates for high temperature steam mobility control: Structure-property correlations,” in *International*

Symposium on Oilfield Chemistry, Society of Petroleum Engineers, 1997.

- [189] W. G. Anderson, “Wettability literature survey-part 4: Effects of wettability on capillary pressure,” *Journal of Petroleum Technology*, vol. 39, no. 10, pp. 1–283, 1987.
- [190] A. Seethepalli, B. Adibhatla, and K. K. Mohanty, “Physicochemical interactions during surfactant flooding of fractured carbonate reservoirs,” *SPE journal*, vol. 9, no. 04, pp. 411–418, 2004.
- [191] T. Austad and D. C. Standnes, “Spontaneous imbibition of water into oil-wet carbonates,” *Journal of Petroleum Science and Engineering*, vol. 39, no. 3, pp. 363–376, 2003.
- [192] B. J. Chun, S. G. Lee, J. I. Choi, and S. S. Jang, “Adsorption of carboxylate on calcium carbonate ($10\bar{1}4$) surface: Molecular simulation approach,” *Colloids and Surfaces A: Physicochemical and Engineering Aspects*, vol. 474, pp. 9–17, 2015.
- [193] M. M. Thomas, J. A. Clouse, and J. M. Longo, “Adsorption of organic compounds on carbonate minerals: 1. model compounds and their influence on mineral wettability,” *Chemical geology*, vol. 109, no. 1-4, pp. 201–213, 1993.
- [194] P. O. Roehl and P. W. Choquette, *Carbonate petroleum reservoirs*. Springer Science & Business Media, 2012.
- [195] D. C. Standnes and T. Austad, “Wettability alteration in chalk: 2. mechanism for wettability alteration from oil-wet to water-wet using surfactants,” *Journal of Petroleum Science and Engineering*, vol. 28, no. 3, pp. 123–143, 2000.

- [196] P. Zhang, M. T. Tweheyo, and T. Austad, "Wettability alteration and improved oil recovery by spontaneous imbibition of seawater into chalk: Impact of the potential determining ions Ca^{2+} , Mg^{2+} , and SO_4^{2-} ," *Colloids and Surfaces A: Physicochemical and Engineering Aspects*, vol. 301, no. 1, pp. 199–208, 2007.
- [197] A. RezaeiDoust, T. Puntervold, S. Strand, and T. Austad, "Smart water as wettability modifier in carbonate and sandstone: A discussion of similarities/differences in the chemical mechanisms," *Energy & fuels*, vol. 23, no. 9, pp. 4479–4485, 2009.
- [198] M. I. Chaudhari, S. B. Rempe, D. Asthagiri, L. Tan, and L. R. Pratt, "Molecular theory and the effects of solute attractive forces on hydrophobic interactions," *The Journal of Physical Chemistry B*, vol. 120, no. 8, pp. 1864–1870, 2016.
- [199] C. Young and J. D. Miller, "Effect of temperature on oleate adsorption at a calcite surface: an ft-nir/irs study and review," *International journal of mineral processing*, vol. 58, no. 1, pp. 331–350, 2000.
- [200] Y. Hu, T. Guo, X. Ye, Q. Li, M. Guo, H. Liu, and Z. Wu, "Dye adsorption by resins: effect of ionic strength on hydrophobic and electrostatic interactions," *Chemical engineering journal*, vol. 228, pp. 392–397, 2013.
- [201] E. TobyáKelsey *et al.*, "Computer modelling of inorganic solids and surfaces," *Faraday Discussions*, vol. 95, pp. 75–84, 1993.
- [202] B. R. Heywood and S. Mann, "Molecular construction of oriented inorganic materials: controlled nucleation of calcite and aragonite under compressed langmuir monolayers," *Chemistry of Materials*, vol. 6, no. 3, pp. 311–318, 1994.

- [203] P. Raiteri, J. D. Gale, D. Quigley, and P. M. Rodger, “Derivation of an accurate force-field for simulating the growth of calcium carbonate from aqueous solution: a new model for the calcite- water interface,” *The Journal of Physical Chemistry C*, vol. 114, no. 13, pp. 5997–6010, 2010.
- [204] E. Stöckelmann and R. Hentschke, “Adsorption isotherms of water vapor on calcite: A molecular dynamics-monte carlo hybrid simulation using a polarizable water model,” *Langmuir*, vol. 15, no. 15, pp. 5141–5149, 1999.
- [205] N. Schmid, A. P. Eichenberger, A. Choutko, S. Riniker, M. Winger, A. E. Mark, and W. F. van Gunsteren, “Definition and testing of the gromos force-field versions 54a7 and 54b7,” *European biophysics journal*, vol. 40, no. 7, pp. 843–856, 2011.
- [206] A. W. Schüttelkopf and D. M. Van Aalten, “Prodrgr: a tool for high-throughput crystallography of protein–ligand complexes,” *Acta Crystallographica Section D: Biological Crystallography*, vol. 60, no. 8, pp. 1355–1363, 2004.
- [207] M. Ø. Jensen, S. Park, E. Tajkhorshid, and K. Schulten, “Energetics of glycerol conduction through aquaglyceroporin glpf,” *Proceedings of the National Academy of Sciences*, vol. 99, no. 10, pp. 6731–6736, 2002.
- [208] S. Kumar, J. M. Rosenberg, D. Bouzida, R. H. Swendsen, and P. A. Kollman, “The weighted histogram analysis method for free-energy calculations on biomolecules. i. the method,” *Journal of computational chemistry*, vol. 13, no. 8, pp. 1011–1021, 1992.
- [209] J. S. Hub, B. L. De Groot, and D. Van Der Spoel, “g-wham a free weighted histogram analysis implementation including robust error and autocorrelation esti-

- mates,” *Journal of Chemical Theory and Computation*, vol. 6, no. 12, pp. 3713–3720, 2010.
- [210] J. A. Lemkul and D. R. Bevan, “Assessing the stability of alzheimers amyloid protofibrils using molecular dynamics,” *The Journal of Physical Chemistry B*, vol. 114, no. 4, pp. 1652–1660, 2010.
- [211] N. Choudhury and B. M. Pettitt, “Enthalpy-entropy contributions to the potential of mean force of nanoscopic hydrophobic solutes,” *The Journal of Physical Chemistry B*, vol. 110, no. 16, pp. 8459–8463, 2006.
- [212] S. Kerisit and S. C. Parker, “Free energy of adsorption of water and metal ions on the {1014} calcite surface,” *Journal of the American Chemical Society*, vol. 126, no. 32, pp. 10152–10161, 2004.
- [213] S. Kerisit, S. C. Parker, and J. H. Harding, “Atomistic simulation of the dissociative adsorption of water on calcite surfaces,” *The Journal of Physical Chemistry B*, vol. 107, no. 31, pp. 7676–7682, 2003.
- [214] D. Spagnoli, S. Kerisit, and S. C. Parker, “Atomistic simulation of the free energies of dissolution of ions from flat and stepped calcite surfaces,” *Journal of crystal growth*, vol. 294, no. 1, pp. 103–110, 2006.
- [215] P. Geissbühler, P. Fenter, E. DiMasi, G. Srajer, L. Sorensen, and N. Sturchio, “Three-dimensional structure of the calcite–water interface by surface x-ray scattering,” *Surface Science*, vol. 573, no. 2, pp. 191–203, 2004.
- [216] D. Ballal and R. Srivastava, “Modeling the interfacial properties of poly (ethylene oxide-co-propylene oxide) polymers at water-toluene interface,” *Fluid Phase Equilibria*, vol. 427, pp. 209–218, 2016.

- [217] A. Lavasanifar, J. Samuel, and G. S. Kwon, "Poly (ethylene oxide)-block-poly (l-amino acid) micelles for drug delivery," *Advanced drug delivery reviews*, vol. 54, no. 2, pp. 169–190, 2002.
- [218] K. Kataoka, A. Harada, and Y. Nagasaki, "Block copolymer micelles for drug delivery: design, characterization and biological significance," *Advanced drug delivery reviews*, vol. 47, no. 1, pp. 113–131, 2001.
- [219] B. Jeong, Y. H. Bae, D. S. Lee, and S. W. Kim, "Biodegradable block copolymers as injectable drug-delivery systems," *Nature*, vol. 388, no. 6645, pp. 860–862, 1997.
- [220] C. Allen, D. Maysinger, and A. Eisenberg, "Nano-engineering block copolymer aggregates for drug delivery," *Colloids and Surfaces B: Biointerfaces*, vol. 16, no. 1, pp. 3–27, 1999.
- [221] K. Mortensen, "Structural properties of self-assembled polymeric micelles," *Current opinion in colloid & interface science*, vol. 3, no. 1, pp. 12–19, 1998.
- [222] Z. Feng, *Multi-Scale Molecular Modeling of Phase Behavior and Microstructure in Polymeric Mixtures with Nanoparticles*. PhD thesis, Rice University, 2013.
- [223] F. A. Detcheverry, D. Q. Pike, P. F. Nealey, M. Müller, and J. J. de Pablo, "Monte carlo simulation of coarse grain polymeric systems," *Physical review letters*, vol. 102, no. 19, p. 197801, 2009.

Appendix A

Numerical Integrals in 1-D Spherical Coordinate

A.1 Introduction

Due to the limitation of computational resources, the integrals in iSAFT are too expensive to handle directly. By taking advantage of the symmetry of the systems being studied, the integrals can be simplified to 1-D form, which makes iSAFT more computationally efficient and easy to implement. Here in this appendix we demonstrate the numerical procedure we took to simplify the integrals in 1-D spherical coordinate and the final forms of some of the most important integrals in iSAFT are provided for reference.

A.2 1-D Numerical Integrals

A.2.1 Ideal Gas Contribution

The ideal gas contribution and its functional derivative are quite straightforward since the functional derivative does not include a convolution. The explicit form is:

$$\beta A^{id}[\rho(\vec{r})] = \int d\vec{r}_2 \sum_{\alpha=1}^m \rho_{\alpha}(\vec{r}_2) [\ln \rho_{\alpha}(\vec{r}_2) - 1] \quad (\text{A.1})$$

This is the ideal gas contribution to the free energy functional. The functional derivative is:

$$\frac{\delta \beta A^{id}}{\delta \rho_{\alpha}(\vec{r}_1)} = \ln \rho_{\alpha}(r_1) \quad (\text{A.2})$$

A.2.2 Hard Sphere Contribution

The hard sphere contribution can be approximated very accurately in a weighted density formalism. There have been several modified versions of weighted density approximation e.g. Rosenfeld's Fundamental Measure Theory(FMT), Wu's modified FMT and White-Bear version FMT. In this thesis, we adopt the Rosenfeld's FMT. As introduced before, the FMT contribution to free energy is give as:

$$\beta A^{hs}[\rho(\vec{r})] = \int d\vec{r}_1 \Phi[n_i(\vec{r}_1)] \quad (\text{A.3})$$

where $n_i(\vec{r}_1)$ are weighted densities, namely $n_0, n_1, n_2, n_3, \vec{n}_{V1}$, and \vec{n}_{V2} :

$$n_i(\vec{r}_1) = \sum_{\alpha} n_{i,\alpha}(\vec{r}_1) = \sum_{\alpha} \int d\vec{r}_2 \rho_{\alpha}(\vec{r}_2) \omega_{\alpha}^{(i)}(\vec{r}_1 - \vec{r}_2) \quad i = 0, 1, 2, 3, V1, V2 \quad (\text{A.4})$$

Here $\omega_{\alpha}^{(i)}$ are six weighting functions representing the contribution to free energy functional from mass, surface area and volume. They are given by:

$$\begin{aligned} \omega_{\alpha}^{(2)}(r) &= \delta(R_{\alpha} - r), \omega_{\alpha}^{(3)}(r) = \Theta(R_{\alpha} - r), \vec{\omega}_{\alpha}^{(V2)}(\vec{r}) = \frac{\vec{r}}{r} \delta(R_{\alpha} - r), \\ \omega_{\alpha}^{(0)}(r) &= \frac{\omega_{\alpha}^{(2)}(r)}{4\pi R_{\alpha}^2}, \omega_{\alpha}^{(1)}(r) = \frac{\omega_{\alpha}^{(2)}(r)}{4\pi R_{\alpha}}, \vec{\omega}_{\alpha}^{(V1)}(\vec{r}) = \frac{\vec{\omega}_{\alpha}^{(V2)}(\vec{r})}{4\pi R_{\alpha}} \end{aligned} \quad (\text{A.5})$$

$\Phi[n_{\alpha}(\vec{r}_1)]$ is given by:

$$\Phi[n_{\alpha}(\vec{r}_1)] = -n_0 \ln(1 - n_3) + \frac{n_1 n_2}{1 - n_3} + \frac{n_2^3}{24\pi(1 - n_3)^2} - \frac{\vec{n}_{V1} \cdot \vec{n}_{V2}}{1 - n_3} - \frac{n_2 \vec{n}_{V1} \cdot \vec{n}_{V2}}{8\pi(1 - n_3)^2} \quad (\text{A.6})$$

We start with the averaged fundamental geometrical measures n_i of the particles. Since n_0, n_1 and \vec{n}_{V1} are trivial once we know n_2, n_3 , and \vec{n}_{V2} , we here only do the 1-D integration of n_2, n_3 and \vec{n}_{V2} .

$$n_i(\vec{r}_1) = \sum_{\alpha} n_{i,\alpha}(\vec{r}_1) = \sum_{\alpha} \int d\vec{r}_2 \rho_{\alpha}(\vec{r}_2) \omega_{\alpha}^{(i)}(\vec{r}_1 - \vec{r}_2) \quad i = 0, 1, 2, 3, V1, V2 \quad (\text{A.7})$$

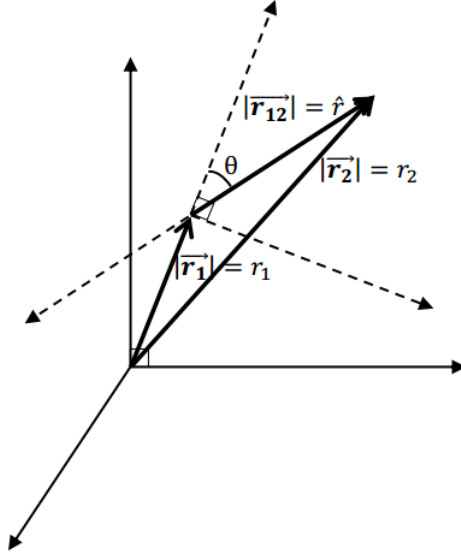


Figure A.1 : Coordinate transformation from rectanlinear to spherical coordinate.

We first define $\vec{r}_{12} = \vec{r}_2 - \vec{r}_1$ (Fig. A.1). Then we substitute \vec{r}_2 with $\vec{r}_1 + \vec{r}_{12}$ and n_i becomes:

$$n_i(\vec{r}_1) = \sum_{\alpha} \int d\vec{r}_{12} \rho_{\alpha}(\vec{r}_{12} + \vec{r}_1) \omega_{\alpha}^{(i)}(-\vec{r}_{12}) \quad i = 0, 1, 2, 3, V1, V2 \quad (\text{A.8})$$

Since it is a linear transformation, the Jacobian from substitution is 1. The boundary of integration will not be changed either since it integrates from negative infinity to positive infinity.

Now we change the rectilinear variable \vec{r}_{12} to curvilinear variables as we do in spherical coordinate. The axis of spherical coordinate and notation for variables are given in Fig A.1. Here we have to add the Jacobian which is a scalar $\hat{r} \sin \theta$, where \hat{r} is the magnitude of \vec{r}_{12} . Then the transformed fundamental geometric measures are:

$$n_i(\vec{r}_1) = \sum_{\alpha} \int_0^{2\pi} d\varphi \int_0^{\pi} \sin \theta d\theta \int_0^{+\infty} \rho_{\alpha}(r_2) \omega_{\alpha}^{(i)}(\hat{r}) \hat{r}^2 d\hat{r} \quad i = 0, 1, 2, 3, V1, V2 \quad (\text{A.9})$$

since \hat{r} and r_2 are directly related by:

$$\hat{r}^2 + r_1^2 + 2r_1\hat{r}\cos\theta = r_2^2 \quad (\text{A.10})$$

we can substitute r_2 with $\sqrt{\hat{r}^2 + r_1^2 + 2r_1\hat{r}\cos\theta}$:

$$n_i(\vec{r}_1) = \sum_{\alpha} \int_0^{2\pi} d\varphi \int_0^{\pi} \sin\theta d\theta \int_0^{+\infty} \rho_{\alpha}(\sqrt{\hat{r}^2 + r_1^2 + 2r_1\hat{r}\cos\theta}) \omega_{\alpha}^{(i)}(\hat{r}) \hat{r}^2 d\hat{r} \quad i = 0, 1, 2, 3, V1, V2 \quad (\text{A.11})$$

Let's first take a look at n_2 . Since the system is spherically symmetrical, $n_2(\vec{r}_1) = n_2(r_1)$. We also use the property of delta function $\int f(r)\delta(r - r_1)dr = f(r_1)$.

$$\begin{aligned} n_2(r_1) &= \sum_{\alpha} \int_0^{2\pi} d\varphi \int_0^{\pi} \sin\theta d\theta \int_0^{+\infty} \rho_{\alpha}(\sqrt{\hat{r}^2 + r_1^2 + 2r_1\hat{r}\cos\theta}) \delta(R_{\alpha} - \hat{r}) \hat{r}^2 d\hat{r} \\ &= \sum_{\alpha} 2\pi \int_0^{\pi} \sin\theta \rho_{\alpha}(\sqrt{R_{\alpha}^2 + r_1^2 + 2r_1R_{\alpha}\cos\theta}) R_{\alpha}^2 d\theta \end{aligned} \quad (\text{A.12})$$

We can further simplified this equation by using Eq. A.13 and Eq. A.14 given by:

$$r' = \sqrt{R_{\alpha}^2 + r_1^2 + 2r_1R_{\alpha}\cos\theta} \quad (\text{A.13})$$

$$dr' = -\frac{R_{\alpha}r_1\sin\theta}{r'} d\theta \quad (\text{A.14})$$

Plugging the above two equations into n_2 and assign proper upper bound and lower bound for the integral, we arrive at:

$$n_2(r_1) = \sum_{\alpha} \frac{2\pi R_{\alpha}}{r_1} \int_{|r_1 - R_{\alpha}|}^{r_1 + R_{\alpha}} \rho_{\alpha}(r') r' dr' \quad (\text{A.15})$$

Similarly we can compute n_3 where a Heaviside function instead of a delta function is involved as:

$$n_3(r_1) = \sum_{\alpha} \int_0^{2\pi} d\varphi \int_0^{\pi} \sin\theta d\theta \int_0^{+\infty} \rho_{\alpha}(\sqrt{\hat{r}^2 + r_1^2 + 2r_1\hat{r}\cos\theta}) \Theta(R_{\alpha} - \hat{r}) \hat{r}^2 d\hat{r} \quad (\text{A.16})$$

Again, we use Eq.A.13 and Eq.A.14 and rearrange n_3 . It becomes:

$$n_3(r_1) = \sum_{\alpha} \frac{2\pi}{r_1} \int_0^{R_{\alpha}} \hat{r} d\hat{r} \int_{|r_1-\hat{r}|}^{r_1+\hat{r}} \rho_{\alpha}(r') r' dr' \quad (\text{A.17})$$

After changing the order of integration, the third geometric measure n_3 for spherically symmetrical system is:

$$\begin{aligned} n_3(r_1) &= \sum_{\alpha} \frac{\pi}{r_1} \int_{|r_1-R_{\alpha}|}^{r_1+R_{\alpha}} (R_{\alpha} - (r_1 - r')^2) \rho_{\alpha}(r') r' dr' \\ &+ \sum_{\alpha} \Theta(R_{\alpha} - r_1) 4\pi \int_0^{R_{\alpha}-r_1} \rho_{\alpha}(r') r'^2 dr' \end{aligned} \quad (\text{A.18})$$

The other scalar geometric measures n_0 and n_1 can be obtained by:

$$n_0(r_1) = \frac{1}{4\pi R_{\alpha}^2} n_2(r_1), n_1(r_1) = \frac{1}{4\pi R_{\alpha}} n_2(r_1) \quad (\text{A.19})$$

The vector geometric measures \vec{n}_{V2} and \vec{n}_{V1} are somewhat more complicated.

$$\begin{aligned} \vec{n}_{V2}(r_1) &= \sum_{\alpha} \int d\vec{r}_2 \rho_{\alpha}(\vec{r}_2) \vec{\omega}_{\alpha}^{V2}(\vec{r}_1 - \vec{r}_2) \\ &= \sum_{\alpha} \int d\vec{r}_2 \rho_{\alpha}(\vec{r}_2) \frac{\vec{r}_1 - \vec{r}_2}{|\vec{r}_1 - \vec{r}_2|} \delta(R_{\alpha} - |\vec{r}_1 - \vec{r}_2|) \\ &= \sum_{\alpha} \int d\vec{r}_{12} \rho_{\alpha}(\vec{r}_1 + \vec{r}_{12}) \frac{-\vec{r}_{12}}{\hat{r}} \delta(R_{\alpha} - \hat{r}) \end{aligned} \quad (\text{A.20})$$

Recognizing that the system is spherically symmetrical, only the vector in \vec{e}_r is non-zero. The above equation becomes:

$$\begin{aligned} \vec{n}_{V2}(r_1) &= \sum_{\alpha} \int d\vec{r}_{12} \rho_{\alpha}(\vec{r}_1 + \vec{r}_{12}) \frac{-\vec{r}_{12}}{\hat{r}} \delta(R_{\alpha} - \hat{r}) \\ &= \sum_{\alpha} \int d\vec{r}_{12} \rho_{\alpha}(\vec{r}_1 + \vec{r}_{12}) \frac{-\hat{r} \cos \theta \vec{e}_r}{\hat{r}} \delta(R_{\alpha} - \hat{r}) \\ &= -\vec{e}_r \sum_{\alpha} \int_0^{2\pi} d\varphi \int_0^{\pi} \sin \theta d\theta \int_0^{+\infty} \rho_{\alpha}(\sqrt{\hat{r}^2 + r_1^2 + 2r_1\hat{r} \cos \theta}) \delta(R_{\alpha} - \hat{r}) \cos \theta \hat{r}^2 d\hat{r} \\ &= -\vec{e}_r \sum_{\alpha} 2\pi \int_{-1}^1 \rho_{\alpha}(\sqrt{R_{\alpha}^2 + r_1^2 + 2r_1 R_{\alpha} \cos \theta}) R_{\alpha}^2 \cos \theta d \cos \theta \end{aligned} \quad (\text{A.21})$$

Plugging in Eq. A.13 and Eq. A.14, we arrive at:

$$\vec{n}_{V2}(r_1) = \vec{e}_r \frac{\pi}{r_1^2} \sum_{\alpha} \int_{|r_1-R_{\alpha}|}^{r_1+R_{\alpha}} \rho_{\alpha}(r') r' (r_1^2 - r'^2 + R_{\alpha}^2) dr' \quad (\text{A.22})$$

The other vectorial geometric measure \vec{n}_{V1} is available through:

$$\vec{n}_{V1}(\vec{r}'_1) = \frac{1}{4\pi R_{\alpha}} \vec{n}_{V2}(r_1) \quad (\text{A.23})$$

Now we have all the weighted densities in 1-D spherical form and they are summarized here:

$$n_0(r_1) = \sum_{\alpha} \frac{1}{2R_{\alpha}r_1} \int_{|r_1-R_{\alpha}|}^{r_1+R_{\alpha}} \rho_{\alpha}(r') r' dr' \quad (\text{A.24})$$

$$n_1(r_1) = \sum_{\alpha} \frac{1}{2r_1} \int_{|r_1-R_{\alpha}|}^{r_1+R_{\alpha}} \rho_{\alpha}(r') r' dr' \quad (\text{A.25})$$

$$n_2(r_1) = \sum_{\alpha} \frac{2\pi R_{\alpha}}{r_1} \int_{|r_1-R_{\alpha}|}^{r_1+R_{\alpha}} \rho_{\alpha}(r') r' dr' \quad (\text{A.26})$$

$$\begin{aligned} n_3(r_1) &= \sum_{\alpha} \frac{\pi}{r_1} \int_{|r_1-R_{\alpha}|}^{r_1+R_{\alpha}} (R_{\alpha}^2 - (r_1 - r')^2) \rho_{\alpha}(r') r' dr' \\ &+ \sum_{\alpha} \Theta(R_{\alpha} - r_1) 4\pi \int_0^{R_{\alpha}-r_1} \rho_{\alpha}(r') r'^2 dr' \end{aligned} \quad (\text{A.27})$$

$$\vec{n}_{V1}(r_1) = \vec{e}_r \frac{1}{4R_{\alpha}r_1^2} \sum_{\alpha} \int_{|r_1-R_{\alpha}|}^{r_1+R_{\alpha}} \rho_{\alpha}(r') r' (r_1^2 - r'^2 + R_{\alpha}^2) dr' \quad (\text{A.28})$$

$$\vec{n}_{V2}(r_1) = \vec{e}_r \frac{\pi}{r_1^2} \sum_{\alpha} \int_{|r_1-R_{\alpha}|}^{r_1+R_{\alpha}} \rho_{\alpha}(r') r' (r_1^2 - r'^2 + R_{\alpha}^2) dr' \quad (\text{A.29})$$

To compute the functional derivative of FMT terms, we first apply chain rule in functional differentiation:

$$\frac{\delta \beta A^{hs}}{\delta \rho_{\alpha}(\vec{r}'_1)} = \int d\vec{r}'_2 \sum_i \frac{\partial \Phi^{hs}}{\partial n_i(\vec{r}'_2)} \frac{\delta n_i(\vec{r}'_2)}{\delta \rho_{\alpha}(\vec{r}'_1)} = \int d\vec{r}'_2 \sum_i \frac{\partial \Phi^{hs}}{\partial n_i(\vec{r}'_2)} \omega_{\alpha}^{(i)}(\vec{r}'_2 - \vec{r}'_1) \quad (\text{A.30})$$

We can see that the forms of the integrals are very similar to the weighted densities (Eq. A.9). Following the same numerical procedure described above, the functional derivative of FMT can be computed:

$$\begin{aligned}
\frac{\delta\beta A^{hs}}{\delta\rho_\alpha(r_1)} &= \int_{|r_1-R_\alpha|}^{r_1+R_\alpha} \left[\frac{1}{2R_\alpha r_1} \frac{\partial\Phi}{\partial n_0(r')} + \frac{1}{2r_1} \frac{\partial\Phi}{\partial n_1(r')} + \frac{2\pi R_\alpha}{r_1} \frac{\partial\Phi}{\partial n_2(r')} \right] r' dr' \\
&+ \int_{|r_1-R_\alpha|}^{r_1+R_\alpha} \left[\frac{\partial\Phi}{\partial n_3(r')} \frac{\pi}{r_1} (R_\alpha^2 - (r_1 - r')^2) \right] r' dr' \\
&+ \Theta(R_\alpha - r_1) 4\pi \int_0^{R_\alpha - r_1} \frac{\partial\Phi}{\partial n_3(r')} r'^2 dr' \\
&- \vec{e}_r \int_{|r_1-R_\alpha|}^{r_1+R_\alpha} \left[\frac{\pi}{r_1^2} \frac{\partial\Phi}{\partial \vec{n}_{V2}(r')} r' (r_1^2 - r'^2 + R_\alpha^2) \right] dr' \\
&- \vec{e}_r \int_{|r_1-R_\alpha|}^{r_1+R_\alpha} \left[\frac{1}{4r_1^2 R_\alpha} \frac{\partial\Phi}{\partial \vec{n}_{V1}(r')} r' (r_1^2 - r'^2 + R_\alpha^2) \right] dr'
\end{aligned} \tag{A.31}$$

A.2.3 Long Range Attraction

Functional derivative due to long range attraction is approximated by mean field method and it is given below.

$$\beta A^{att}[\rho(\vec{r})] = \frac{1}{2} \sum_\alpha \sum_\beta \int \int_{|\vec{r}_1 - \vec{r}_2| > \sigma_{\alpha\beta}} d\vec{r}_1 d\vec{r}_2 \rho_\alpha(\vec{r}_1) \rho_\beta(\vec{r}_2) \beta u_{\alpha\beta}^{att}(|\vec{r}_1 - \vec{r}_2|) \tag{A.32}$$

$$\begin{aligned}
\frac{\delta\beta A^{att}}{\delta\rho_\alpha(\vec{r}_1)} &= \sum_\beta \int_{|\vec{r}_1 - \vec{r}_2| > \sigma_{\alpha\beta}} d\vec{r}_2 \rho_\beta(\vec{r}_2) \beta u_{\alpha\beta}^{att}(|\vec{r}_1 - \vec{r}_2|) \\
&= \sum_\beta 2\pi \int_0^\pi \sin\theta d\theta \int_{\sigma_{\alpha\beta}}^{+\infty} \rho_\alpha(\sqrt{\hat{r}^2 + r_1^2 + 2r_1\hat{r}\cos\theta}) \beta u_{\alpha\beta}^{att}(\hat{r}) \hat{r}^2 d\hat{r}
\end{aligned} \tag{A.33}$$

The 1-D integral can be written as:

$$\frac{\delta\beta A^{att}}{\delta\rho_\alpha(r_1)} = \begin{cases} \sum_\beta \frac{2\pi}{r_1} \int_{\sigma_{\alpha\beta} - r_1}^{+\infty} dr' r' \rho_\beta(r') \int_{\max(|r' - r_1|, \sigma_{\alpha\beta})}^{r' + r_1} d\hat{r} \beta u_{\alpha\beta}^{att}(\hat{r}) \hat{r}, & r_1 < \sigma_{\alpha\beta} \\ \sum_\beta \frac{2\pi}{r_1} \int_0^{2r_1} dr' r' \rho_\beta(r') \int_{\max(|r' - r_1|, \sigma_{\alpha\beta})}^{r_1} d\hat{r} \beta u_{\alpha\beta}^{att}(\hat{r}) \hat{r} \\ + \sum_\beta \frac{2\pi}{r_1} \int_0^{+\infty} dr' r' \rho_\beta(r') \int_{\max(|r' - r_1|, r_1)}^{r' + r_1} d\hat{r} \beta u_{\alpha\beta}^{att}(\hat{r}) \hat{r}, & r_1 \geq \sigma_{\alpha\beta} \end{cases} \tag{A.34}$$

Realizing that $u_{\alpha\beta}^{att}$ is known, the second integral can be handled analytically.

A.2.4 Association Contribution

Association contribution to the over all Helmholtz free energy functional is given below.

$$\beta A^{assoc}[\rho(\vec{r})] = \int d\vec{r} \sum_{\alpha=1}^N \rho_{\alpha}(\vec{r}) \sum_{A \in \Gamma(\alpha)} (\ln X_A^{\alpha}(\vec{r}) - \frac{X_A^{\alpha}(\vec{r})}{2} + \frac{1}{2}) \quad (\text{A.35})$$

Its functional derivative can be derived as:

$$\frac{\delta \beta A^{assoc}}{\delta \rho_{\alpha}(\vec{r}_1)} = \sum_{A \in \Gamma(\alpha)} \ln X_A^{\alpha}(\vec{r}_1) - \frac{1}{2} \sum_{\beta=1}^N \sum_{\beta'}^{\{\beta'\}} \int d\vec{r}_2 \rho_{\beta}(\vec{r}_2) \sum_{A \in \Gamma(\beta)} (1 - X_A^{\beta}(\vec{r}_2)) \left[\frac{\delta \ln y^{\beta\beta'}(\bar{\rho}(\vec{r}_2))}{\delta \rho_{\alpha}(\vec{r}_1)} \right] \quad (\text{A.36})$$

Applying the chain rule for the functional derivative $\frac{\delta \ln y^{\beta\beta'}(\bar{\rho}(\vec{r}_2))}{\delta \rho_{\alpha}(\vec{r}_1)}$:

$$\begin{aligned} \frac{\delta \ln y^{\beta\beta'}(\bar{\rho}(\vec{r}_2))}{\delta \rho_{\alpha}(\vec{r}_1)} &= \frac{\partial \ln y^{\beta\beta'}(\bar{\rho}(\vec{r}_2))}{\partial \bar{\rho}_{\alpha}(\vec{r}_2)} \frac{\delta \bar{\rho}_{\alpha}(\vec{r}_2)}{\delta \rho_{\alpha}(\vec{r}_1)} \\ &= \frac{\partial \ln y^{\beta\beta'}(\bar{\rho}(\vec{r}_2))}{\partial \bar{\rho}_{\alpha}(\vec{r}_2)} \frac{3}{4\pi\sigma^3} \Theta(\sigma - |\vec{r}_1 - \vec{r}_2|) \end{aligned} \quad (\text{A.37})$$

Plugging this equation back to the original equation of the functional derivative gives:

$$\begin{aligned} \frac{\delta \beta A^{assoc}}{\delta \rho_{\alpha}(\vec{r}_1)} &= \sum_{A \in \Gamma(\alpha)} \ln X_A^{\alpha}(\vec{r}_1) - \frac{1}{2} \sum_{\beta=1}^N \sum_{\beta'}^{\{\beta'\}} \int d\vec{r}_2 \rho_{\beta}(\vec{r}_2) \sum_{A \in \Gamma(\beta)} (1 - X_A^{\beta}(\vec{r}_2)) \left[\frac{\partial \ln y^{\beta\beta'}(\bar{\rho}(\vec{r}_2))}{\partial \bar{\rho}_{\alpha}(\vec{r}_2)} \right] \\ &\quad \times \frac{3}{4\pi\sigma^3} \Theta(\sigma - |\vec{r}_1 - \vec{r}_2|) \\ &= \sum_{A \in \Gamma(\alpha)} \ln X_A^{\alpha}(r_1) + \frac{1}{2} \frac{3}{4\pi\sigma^3} \sum_{\beta=1}^N \sum_{\beta'}^{\{\beta'\}} \frac{\pi}{r_1} \int_{|r_1-\sigma|}^{r_1+\sigma} (\sigma^2 - (r_1 - r')^2) \rho_{\beta}(r') \\ &\quad \times \sum_{A \in \Gamma(\beta)} (1 - X_A^{\beta}(r')) \left[\frac{\partial \ln y^{\beta\beta'}(\bar{\rho}(r'))}{\partial \bar{\rho}_{\alpha}(r')} \right] r' dr' \\ &\quad + \frac{1}{2} \frac{3}{4\pi\sigma^3} \sum_{\beta=1}^N \sum_{\beta'}^{\{\beta'\}} \Theta(\sigma - r_1) 4\pi \int_0^{\sigma-r_1} \rho_{\beta}(r') \sum_{A \in \Gamma(\beta)} (1 - X_A^{\beta}(r')) \left[\frac{\partial \ln y^{\beta\beta'}(\bar{\rho}(r'))}{\partial \bar{\rho}_{\alpha}(r')} \right] r'^2 dr' \end{aligned} \quad (\text{A.38})$$

A.2.5 Chain Formation Contribution

Chain contribution is based on association contribution so they carry similar forms.

The 1-D integral is given:

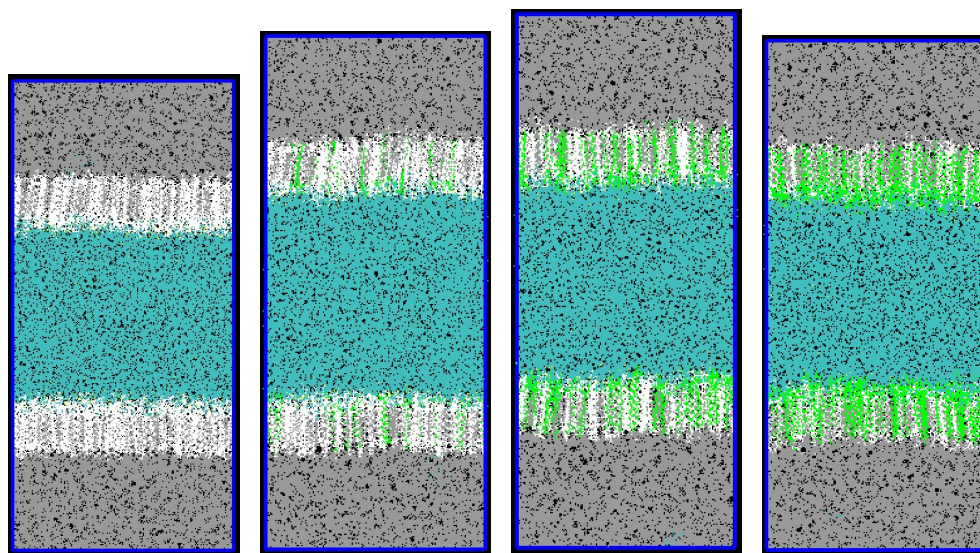
$$\begin{aligned}
\frac{\delta \beta A^{chain}}{\delta \rho_\alpha(\vec{r}_1)} &= \sum_{A \in \Gamma(\alpha)} \ln X_A^\alpha(\vec{r}_1) - \frac{1}{2} \sum_{\beta=1}^N \sum_{\beta'}^{\{\beta'\}} \int d\vec{r}_2 \rho_\beta(\vec{r}_2) \left[\frac{\delta \ln y^{\beta\beta'}(\bar{\rho}(\vec{r}_2))}{\delta \rho_\alpha(\vec{r}_1)} \right] \\
&= \sum_{A \in \Gamma(\alpha)} \ln X_A^\alpha(r_1) + \frac{1}{2} \frac{3}{4\pi\sigma^3} \sum_{\beta=1}^N \sum_{\beta'}^{\{\beta'\}} \frac{\pi}{r_1} \int_{|r_1-\sigma|}^{r_1+\sigma} (\sigma^2 - (r_1 - r')^2) \rho_\beta(r') \left[\frac{\partial \ln y^{\beta\beta'}(\bar{\rho}(r'))}{\partial \bar{\rho}_\alpha(r')} \right] r' dr \\
&\quad + \frac{1}{2} \frac{3}{4\pi\sigma^3} \sum_{\beta=1}^N \sum_{\beta'}^{\{\beta'\}} \Theta(\sigma - r_1) 4\pi \int_0^{\sigma-r_1} \rho_\beta(r') \left[\frac{\partial \ln y^{\beta\beta'}(\bar{\rho}(r'))}{\partial \bar{\rho}_\alpha(r')} \right] r'^2 dr'
\end{aligned} \tag{A.39}$$

Monomer fraction $\ln X_A$ at the limit of complete association can be seen in the theory section. Its 1-D integration is similar to the derivation shown previously.

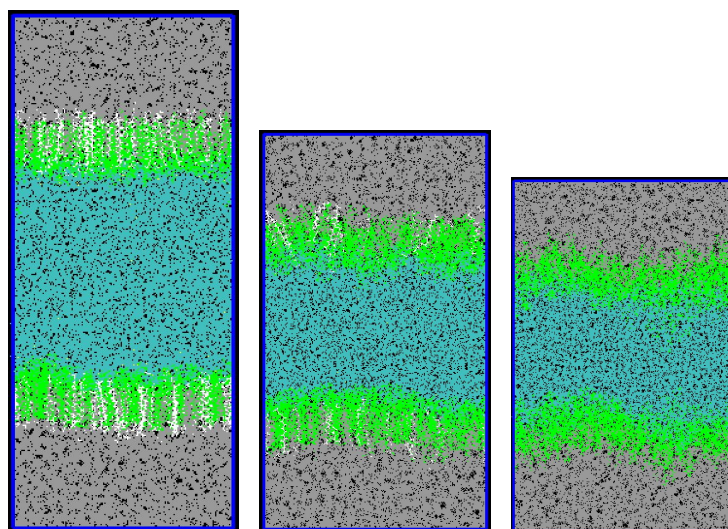
Appendix B

Simulation Box Snapshots and Pair Correlation Functions

B.1 Snapshots of the simulation box



(a) 0% LB, system 1 (b) 10% LB, system 2 (c) 30% LB, system 3 (d) 50% LB, system 4



(e) 70% LB, system 5 (f) 90% LB, system 6 (g) 100% LB, system 7

7

Figure B.1 : Snapshots of the systems listed in Table 1 at the end of production. Color scheme: LB in green, AOS in white, octane in gray, water in blue, and NA in yellow. Black represents vacuum. The aspect ratios of the simulation boxes printed here are kept the same as the original simulation cells while the real dimensions are not produced.

B.2 Pair Correlation Functions

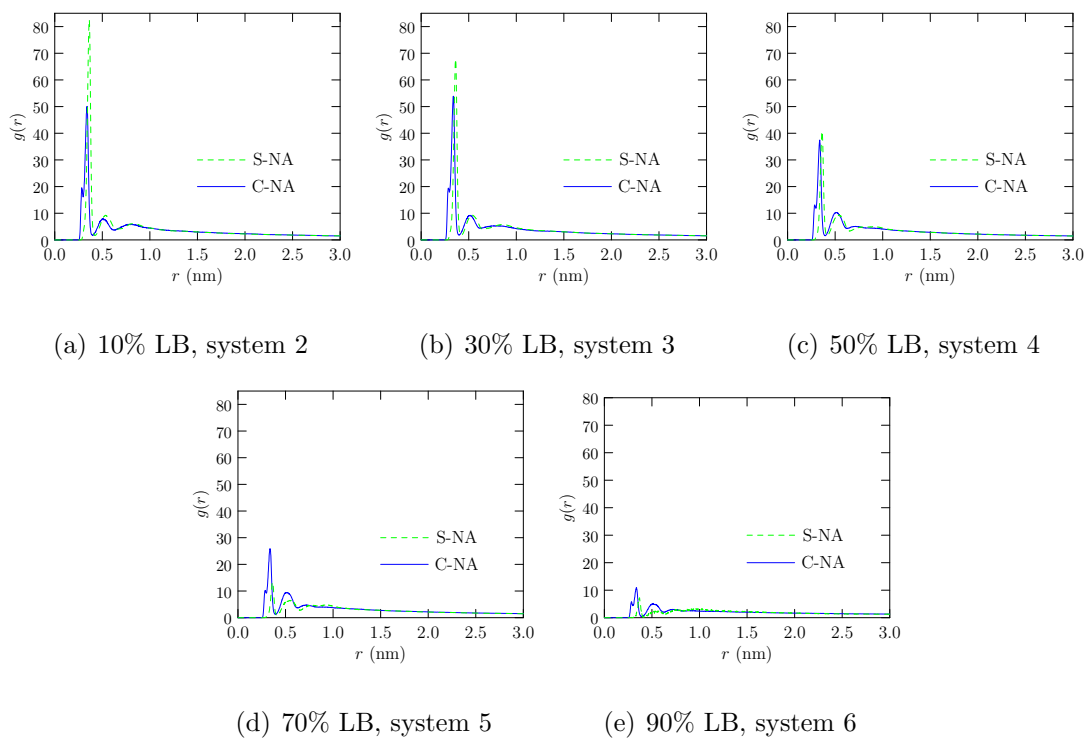


Figure B.2 : 3-D Pair correlation functions between C in carboxylic group of LB and sodium(solid blue) and S in sulfonate group of AOS and sodium(dash green), respectively. The range of y axes are kept the same for comparison.